A coupled modeling-experimental study of Li-air Batteries

Yinghui Yin

Thèse de Doctorat

Mention : Chimie
Spécialité : Chimie des Solides et Sciences des Matériaux

présentée à *l'Ecole Doctorale en Sciences Technologie et Santé (ED 585)*

de l'Université de Picardie Jules Verne

par

Yinghui YIN

pour obtenir le grade de Docteur de l'Université de Picardie Jules Verne

A Coupled Modeling/Experimental Study of Li-air Batteries

Soutenue le 22/02/2018, après avis des rapporteurs, devant le jury d'examen :

M. W. Bessler,	**Professeur, Hochschule Offenburg**	**Rapporteur**
M. F. Favier,	**Professeur, Université de Montpellier**	**Rapporteur**
M^me F. Bardé,	**Senior Scientist, Toyota Motor Europe**	**Examinateur**
M. D. Loffreda,	**Directeur de recherche, ENS Lyon**	**Examinateur**
M. D. Larcher,	**Professeur, UPJV, Amiens**	**Directeur de Thèse**
M. A. A. Franco,	**Professeur, UPJV, Amiens & IUF, Paris**	**Directeur de Thèse**

Ce projet est cofinancé par l'Union européenne L'Europe s'engage en Picardie avec le Fond européen de développement régional

To my parents,

Lixing Yin

Hongwei Wan

To Ruxi

Acknowledgements

This thesis marks the end of a three-year journey. It is not easy but it was memorable time for me particularly because of all the wonderful people that I have met during the journey.

Firstly, I would like to thank my supervisors, Prof. Alejandro A. Franco and Dominique Larcher, for all their guidance, encouragement and supports during the thesis. Alejandro's passion to science is always the source of inspiration for me. I appreciate a lot when he provides me the freedom to explore outside the box and build the model from scratch. I admire very much Dominique's rigorous attitude to science and profound knowledge. I am also grateful for having the chance to learn to do the "bricolage".

I gratefully acknowledge Kanhao Xue, Matias Quiroga and Trong-Khoa Nguyen for helping me to step into the world of modeling. I would like also to thank Jean-Bernard Leriche and Sébastien Cavalaglio for their help to set up the "LeParfait" pot for the Li-air battery cycling. Many thanks to the "Li-air Team" in LRCS: Guillaume, Ruijie, Caroline, Amangeldi, Vigneshwaran, for all the collaborations: brainstorming, discussion and debugging. Sometimes, it was not always easy to convince each other but I enjoy a lot the sparkling from the collision of ideas.

Many thanks to my dear friends in the lab who made my life in Amiens so enjoyable: Garima, Iryna, Ronan, Laura, Alice, Simon, Boris, Mattia, Alain, Alexis, Mariem, Zeliang, Rakesh and all others in LRCS. Thanks to Yue, Meiling, Wei and Fan for making me feel at home.

I also want to thank my parents who protected my curiosity carefully when I was young and encouraged me to embrace the beauty of nature and provided me with their unconditional love. Lastly, I would like to extend my appreciation to my boyfriend, Ruxi for taking care of me and always being by my side.

Preface

The global climate change and the depletion of fossil fuels prompt us to shift to renewableal energy sources with low carbon emission, whose penetration requires reliable devices to concentrate and store the captured energy. Towards high energy density, Li-air batteries are proposed as promising candidates for the next generation of energy storage devices. However, despite the efforts in the last decades, fundamental breakthroughs are still needed to enable the practical applications of metal-air systems. This is due to the high complexity of these systems resulting from the reaction mechanisms, electrode textural variations and various side reactions.

Promoted by the advancements of computational sciences, mathematical modeling emerges as a powerful tool to study the behavior of such complex systems, as already done for many years, for instance, in weather forecasting and stock market predictions. Nowadays, it is recognized that mathematical modeling can be helpful for assessing and optimizing electrochemical systems such as proton-exchange membrane fuel cells and Li-ion batteries. In this context, the coupling of experiment and modeling may provide a new possibility to untangle the complexity and to deepen the understanding of Li-air batteries,[1] with the hope to accelerate the maturation of this technology.

Instead of targeting a perfect match between modeling prediction and experimental data, this thesis rather focuses on the physical meaning of the models, aiming at converging the scattered experimental observations into a comprehensive self-consistent and unified theory, which can predict trends, within a wide spectrum of conditions, in consistency with such experimental observations.

---

[1] Franco, A. A.; Doublet, M. L.; Bessler, W. G. *Physical Multiscale Modeling and Numerical Simulation of Electrochemical Devices for Energy Conversion and Storage: From Theory to Engineering to Practice*; Springer, 2015.

Table of Contents

Chapter 1 : General Introduction

I General Introduction

I.1 Towards renewable energy and low carbon-emission

Energy is of central interest today, as it is not only the prerequisite for the improvement of living standards, but also the pillar for the advancement of our society. Starting from late nineteenth century, the four successive industrial revolutions have liberated people from repetitive labor, boosted the economy growth and kicked off technological innovation, leading us to a modern life with an unprecedented vision (**Figure 1.1**).

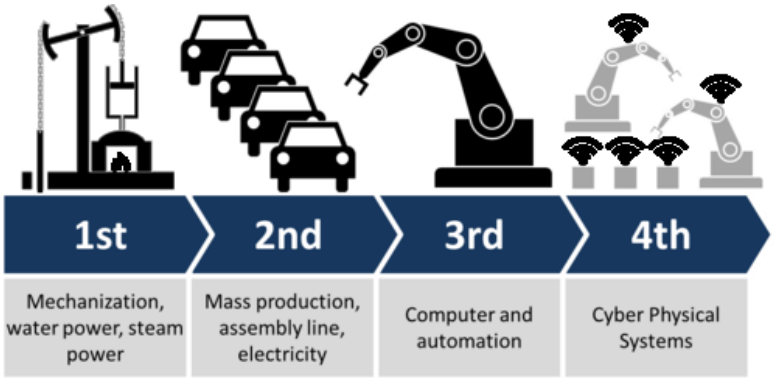

Figure 1.1: Industrial revolutions and future view. Credit of figure: Christoph Roser at *AllAboutLean.com*

Today, we are able to communicate with others from thousands of kilometers away without any delay; we are able to reach the other side of the globe within a single day and since the *Voyager1* probe entered the interstellar space in 2012, we are even able to deliver a sign of our existence beyond our solar system.[1] All these conveniences of life and ambitions of our civilization are rooted from a huge energy consumption, which keeps increasing as the worldwide population grows incessantly. It is projected that the annual energy consumption rate will increase from 16 TW in 2016 to 30 TW in 2050 (**Figure 2**).[2]

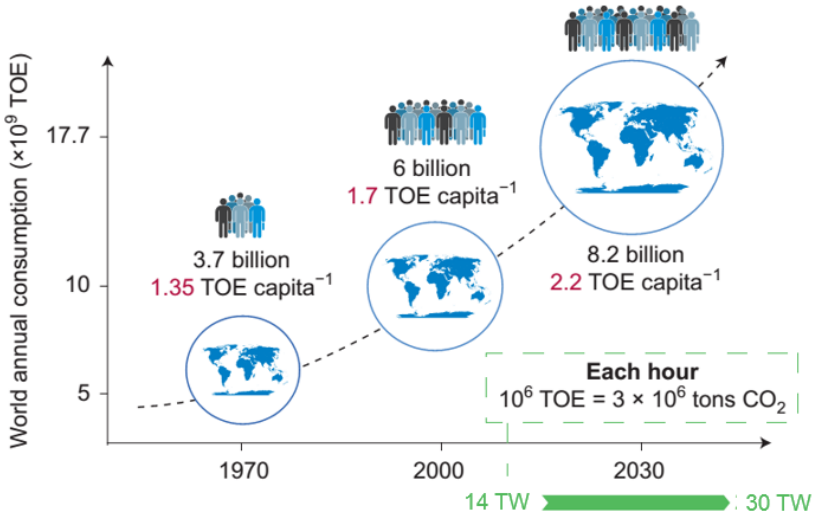

Figure 1.2: Past, present and forecast of the world's energy needs up to 2050. TOE = ton of oil equivalent.[2]

Since the late 1800s, fossil fuels such as coal, oil and natural gas, have accounted for most of our energy supply (**Figure 1.3 a**).[3] However, they could not be the ultimate solution for the escalating energy demand considering the following issues:

(a) fossil fuels have limited reserves as they are non-renewable energy sources. If the current energy structure remains unchanged, the known reserves of coal, natural gas and oil will be depleted in 100, 50 and 50 years, respectively (**Figure 1.3 b**).[4]

(b) the extraction processes, particularly the deep mining and drilling, are at high risk of generating air and water pollution, threatening environment and biodiversity.[5] Unregulated or inefficient fuel combustion is the most important man-made source for the air pollutants such as particulate matter, sulfur oxides, nitrogen oxides and volatile organic compounds, which are responsible for most of the world's air pollution. Globally, around 6.5 million deaths are attributed each year to poor air quality.[6]

(c) burning of the fossil fuels also leads to enormous emission of greenhouse gases, which is believed to be the main cause of the global climate changes and sea-leveling rising as observed in recent 50 years.[7]

(d) the non-uniform distribution of fossil fuels causes geopolitical tensions, even became flashpoint of wars, as the Gulf war in 1990; the political interplays

between countries result in the price waving of fossil fuels and bring about economic instability.

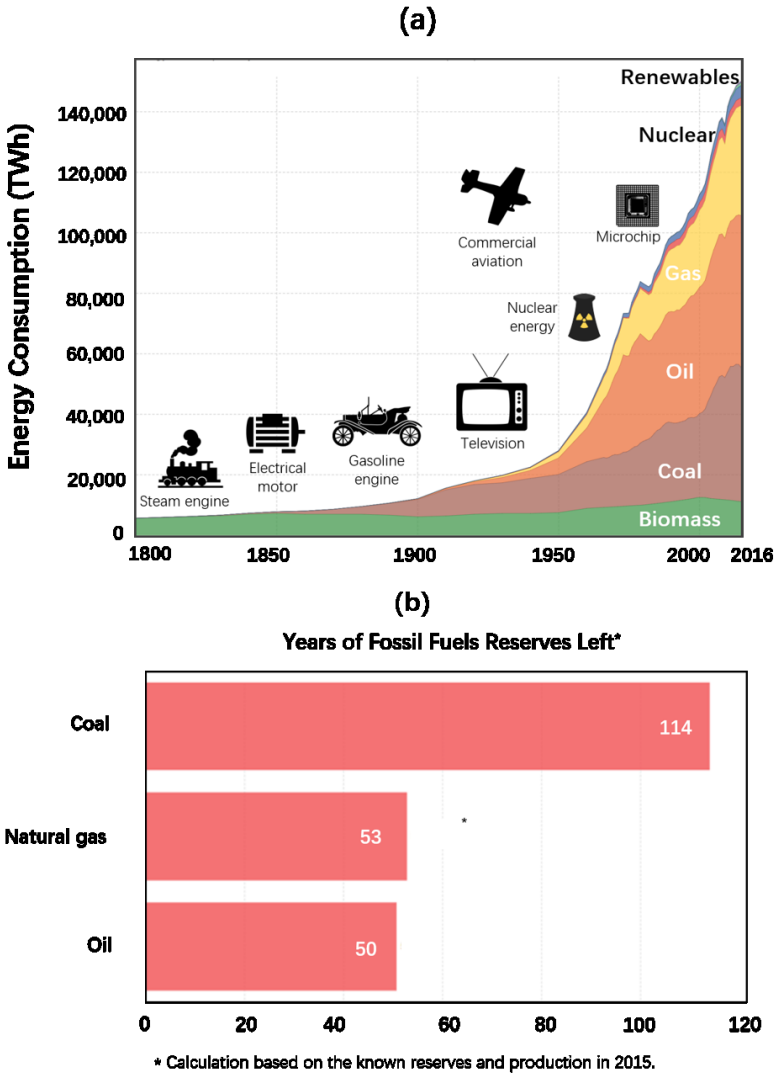

Figure 1.3: (a) Energy consumption and its primary sources since the first industrial revolution;[3] (b) Estimation in years of fossil fuels reserve left based on the data of known reserves and production on 2015.[7]

Aiming at sustainable development, it is a critical moment now to break our dependence on fossil fuels and to shift towards renewable energy sources, particularly those with low carbon-emission. Hydropower holds the largest share in electricity generation among the low-carbon renewable energy sources (**Figure 1.4**), but its growth is limited by geological constraint and high initial investment. Solar photovoltaic and wind energy are two energy resources that increase the most rapidly, with average annual growth rates of 45 % and 24 %, respectively, much faster than the

growth rate of the world Total Primary Energy Supply (TPES) (**Figure 1.5**).[8] In some developed countries, the low carbon-emission renewable energies have already played an important role in the energy market. For example, in Denmark, wind energy has accounted for 40% of total energy consumption in 2015.[9] With the development of renewable energy sources, higher demands for energy storage are created.

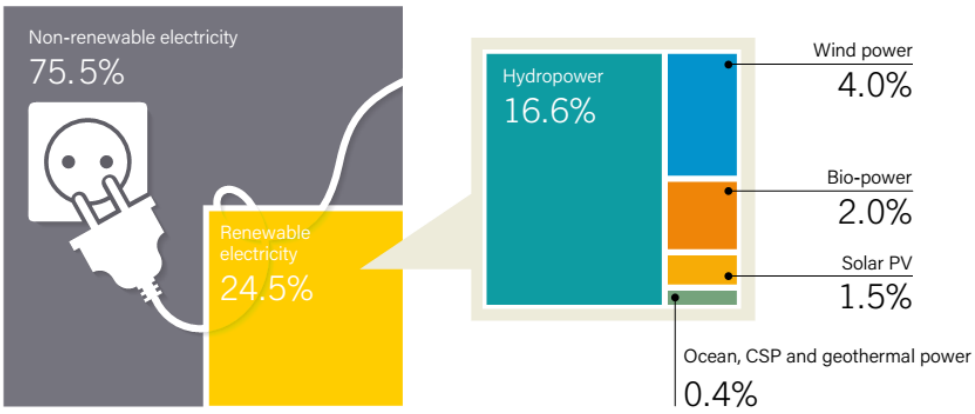

Figure 1.4: World electricity production from different energy sources in 2016.[10]

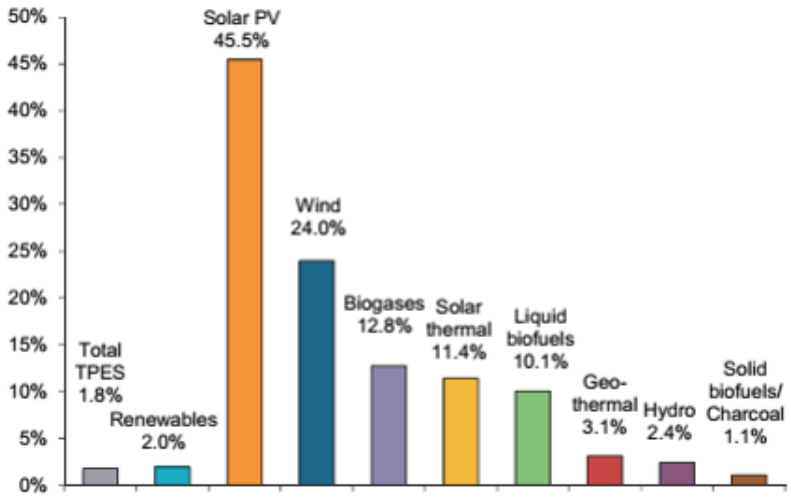

Figure 1.5: Average annual growth rates of world renewable energies supply from 1990 to 2015.[8]

I.2 More renewable energy requires more energy storage

Energy storage systems store energy when the demand is low, or when the electricity (or heat) supply exceeds demand, and supply the stored energy when the demand is high. Since a long time, various energy storage systems have been used for different purposes including adjusting the grid loading, providing back-up energy supply, supporting off-grid systems and facilitating energy access for mobile devices. The increasing demand of energy storage from renewable energy sources, particularly solar energy and wind energy, is driven by their intermittance and the development of electrical vehicles (EV).

Direct solar energy and wind energy come from the sunlight and air flow, which are usually converted into electricity by solar photovoltaic panels and wind turbines, or/and into heat by solar thermal collectors. However, the sun is not always shining and the air is not always blowing, leading to the diurnal, monthly and seasonal fluctuations of energy harvest (**Figure 1.6**). Due to this variability, energy storage systems are required to be integrated to regulate the energy output and to improve the dispatchability of the energy sources.

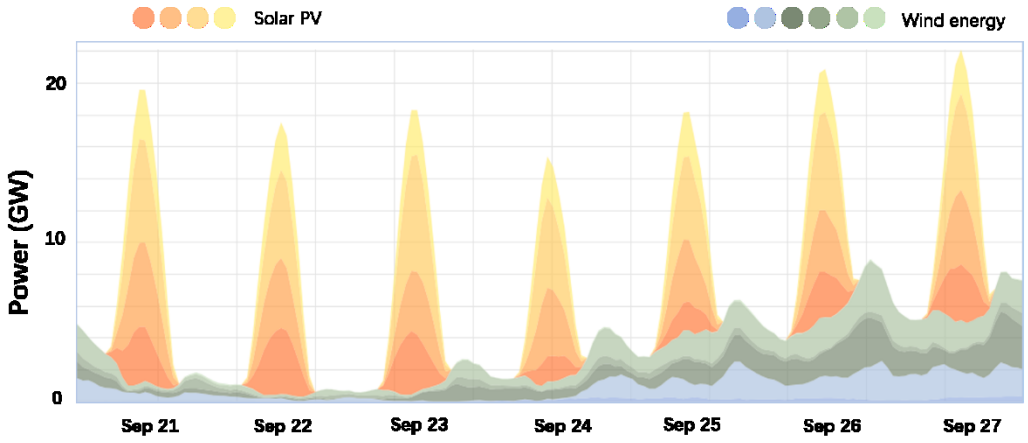

Figure 1.6: The electricity production from solar PV and wide energy in a week of September 2017. Data source: Fraunhofer Institute for Solar Energy Systems.[11]

Another important application of energy storage in the scenario of renewable energy is transportation. Due to high energy density and power density, fossil fuels are predominately used for traditional vehicles powered by combustion engines. Statistics

show that during the period 1990-2015, 47.5% of oil consumption in the European Union was for the sector of road transport (**Figure 1.7**).[12] The solution to the oil-dependent road transport is to replace the internal combustion engine vehicles (ICVs) with the electrical vehicles (EVs). Thus, a system is required to be implemented to store the electricity and then power the vehicles.

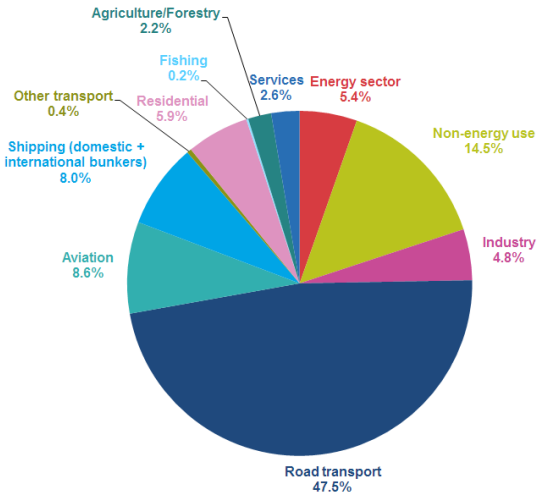

Figure 1.7: Final oil consumption by sector in the European Union during the period 1990-2015. Source: Eurostat.[12]

There is a spectrum of energy storage systems available today, whose choice depends on applications. For large scale applications, such as a power plant, pumped hydroelectric storage (PHS) is the most used system as it meets the requirement of storing massive energy and power at relative low levelized cost. For smaller scale applications, where the size and weight of the energy storage system really matter, batteries become the top choice due to their compact size and high specific energy density. For example, nowadays all the batteries in our phones and laptops are Li-ion batteries (LIBs), which are also used in most of today's plug-in full EVs.

I.3 Li-ion batteries: current and beyond

Batteries, which are devices converting chemical energy to electric energy, can be classified into two categories: primary batteries, which are not rechargeable, and secondary batteries that could be recharged after discharge by applying a current in a

direction opposite to the discharge current. Batteries for energy storage are obviously of the secondary type.

The past decades witnessed the evolution of batteries, which changed step-by-step from lead-acid batteries to Ni-Cd batteries, then to Ni-metal hydride batteries (Ni-MH) and finally to LIBs, all the way towards more energy at smaller size and lower weight. As shown in **Figure 1.8**, from lead-acid batteries to LIBs, the gravimetric and volumetric energy densities increased by a factor of 4 and 6 over 150 years.[13] As a result, more energy could be stored within the volume of vehicles and the function of these batteries was extended from simple lighting and ignition to fully power an entire vehicle up to 300 km per full charge.[14]

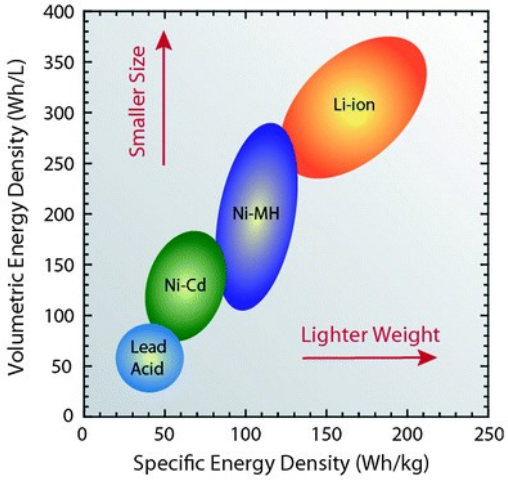

Figure 1.8: Gravimetric and volumetric energy densities of various secondary batteries.[13]

The concept of LIBs was first proposed in the 70s and commercialized by Sony in 1991.[15] Though there were many improvements since then, most of today's LIBs are still based on intercalation chemistry. A typical LIB consists of a positive electrode, a negative electrode and a liquid electrolyte that provides ionic conductivity while electronically isolating the electrodes (**Figure 1.9**). During the discharge process, Li^+ ions de-intercalate from the host materials in the negative electrode, move through the electrolyte and intercalate into the positive host material. At the same time, electrons flow in the same direction through the external circuit to compensate the ion flow,

generating electricity. Both flows are reversed under an imposed opposite current during the charge process.

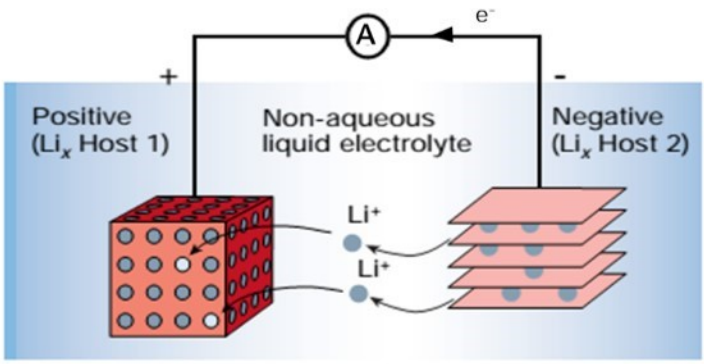

Figure 1.9: Schematic representation and operating principle of rechargeable Li-ion batteries.[13]

The commonly used positive electrode materials are transition metal oxide compounds including $LiCoO_2$,[16,17] $LiNi_{0.8}Co_{0.15}Al_{0.05}O_2$ (NCA),[18] $LiNi_{1/3}Co_{1/3}Mn_{1/3}O_2$ (NMC),[19] $LiMn_2O_4$ (LMO)[20] and $LiFePO_4$ (LFP),[21] the characteristics of which are summarized in **Table 1.1**. For the negative electrode, graphite[22,23] and $Li_4Ti_5O_{12}$ (LTO)[24,25] are the most popular materials. The practical energy density of today's LIBs is around 200 Wh/kg.

Table 1.1 The characteristics of commercial Li-ion battery cathode materials.[26]

Material	Structure	Potential versus Li/Li^+, average V	Specific capacity, mAh/g
$LiCoO_2$	Layered	3.9	140
$LiNi_{0.8}Co_{0.15}Al_{0.05}O_2$ (NCA)	Layered	3.8	180–200
$LiNi_{1/3}Co_{1/3}Mn_{1/3}O_2$ (NMC)	Layered	3.8	160–170
$LiMn_2O_4$ and variants (LMO)	Spinel	4.1	100–120
$LiFePO_4$ (LFP)	Olivine	3.45	150–170

However, the high price of LIBs becomes one of the main barriers to EV's further penetration in the market. Thus, lowering batteries cost is necessary and it could be achieved in two ways: firstly, enhancing the specific energy density of the batteries, to have the same performance at lower weight and volume; secondly, replacing the

battery materials with cheaper ones. Based on these two strategies, a lot of effort has been made both within and beyond the framework of LIBs, from finding new materials for LIBs to developing new batteries system with other chemistries. Among those new battery technologies, Li-air battery (LAB) is considered as a promising candidate due to its high theoretical energy density and the natural abundance of the active positive material, O_2, in replacement of transition metal oxides in LIB.

II. Li-air batteries

LABs rely on the reversible electrochemical reaction between Li and gaseous O_2, thus they are actually Li-O_2 batteries (LOBs). They can operate in both aqueous and non-aqueous electrolyte, forming LiOH and Li_2O_2 as discharge products. The thermodynamic standard potentials of aqueous and non-aqueous LOBs are at 3.45 and 2.96 V, respectively.[27] As formed at much higher potential, LiOH is thermodynamically more stable than Li_2O_2. So, the presence of water in non-aqueous LOBs will result in a preferential formation of LiOH over Li_2O_2.

The formation of 1 kg of LiOH and Li_2O_2 corresponds to 3795 and 3448 Wh of energies, respectively. Such high energy densities become the overarching interests of LOBs. Moreover, while transition metal oxides are obtained from energy-consuming mining and synthetic process, O_2 can be separated directly from the air, making O_2 a cheaper and easier choice for the active materials of positive electrode.

The cell structures and working principles of aqueous and non-aqueous LOBs are shown in **Figure 1.10**. In both cases, the cell consists of a negative electrode based on lithium metal, a separator and a porous positive electrode. Both the separator and porous electrode are soaked with electrolyte. For aqueous Li-air batteries, a Li-conducting but electronically insulating layer is coated on Li metal to prevent the reaction with water.

During the discharge process, Li^+ ions are formed at the negative electrode (**Eq.1.1**). In aqueous LOB, the dissolved O_2 molecules diffuse to the surface of the positive electrode, get reduced and form LiOH with Li^+ ions and water (**Eq.1.2**). The solubility of LiOH in water is around 5.3 M, above which LiOH starts to precipitate in the solution. In non-aqueous LOB, the solvent is not involved in the reaction. The dissolved O_2 molecules are reduced on the electrodes in presence of Li^+ ions to form

Li_2O_2 (**Eq.1.3**), which is insoluble in organic solvent. These reactions are expected to occur in the reverse direction during the charge process, with the decomposition of discharge products and Li deposition. However, LiOH is not readily decomposed due to the difficulties of O-H bond cleavage,[27,28] impairing the reversibility and cyclability of the cell. This intrinsic limitation as well as the technical issue of anode protection results in the unfavorbleness of the aqueous Li-air batteries. **Therefore, more attention, including the focus of the rest of thesis, is attributed to non-aqueous LOBs.**

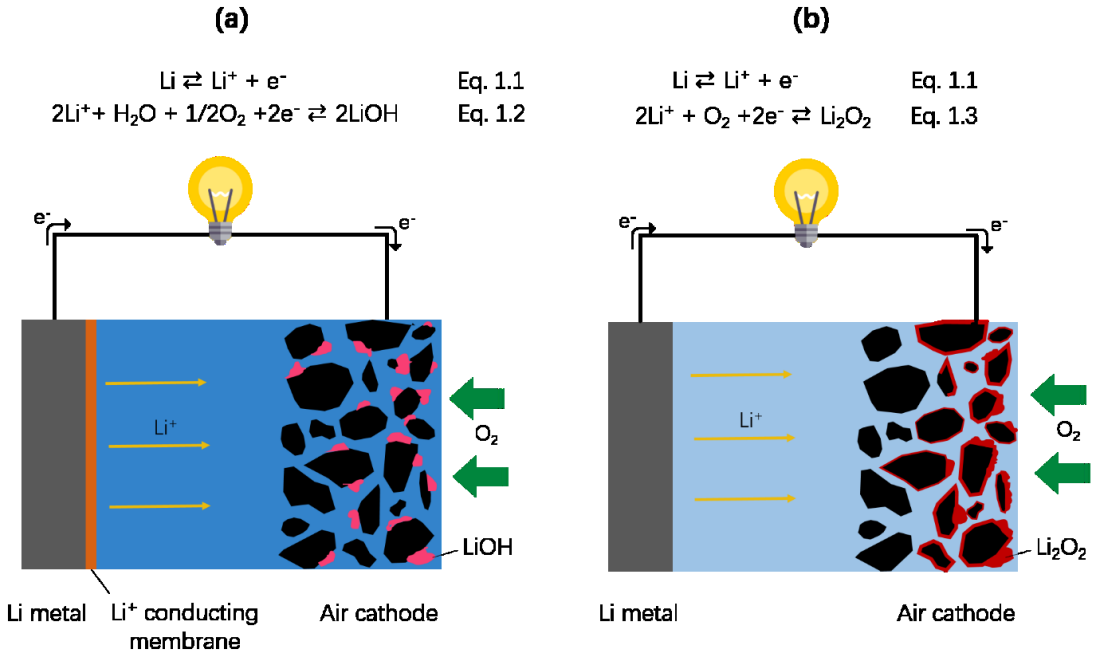

Figure 1.10: Schematic representation of (a) aqueous Li-air batteries and (b) non-aqueous Li-batteries.

The first secondary LOB based on non-aqueous electrolyte was reported by Abrahama *et al.* in 1996.[29] The formation of Li_2O_2 in this cell has been confirmed by Raman spectroscopy but the cyclability of the cell was not good. The revival of the research interests in this field appeared in 2006, after Bruce *et al.* demonstrated that LOBs could be discharged and charged over more than 30 cycles.[30] Despite the endeavors in the past decade, there are still a lot of challenges which LIBs do not face, thus preventing Li-air batteries from approaching the theoretical energy density and stalling commercialization.

Unlike LIBs where all the active materials are encapsulated in the package, the positive electrodes in LOBs are open to O_2 sources to ensure the O_2 untaking and releasing upon cycling. Ideally, the O_2 is fed directly by the ambient air. However, to avoid the formation of Li_2CO_3 and LiOH that are hardly decomposed during charge, CO_2 and H_2O have to be filtered from the cells. Thus, a filtering system is needed if air is employed as the O_2 source. More often, LOBs are performed with pure dry O_2 so as to avert overcomplicated cell design. In this case, O_2 is supplied by O_2 tanks. Incorporating either a filtering system or an O_2 tank significantly increase largely the volume and mass penalties of LOBs. As a result, the energy density of LOBs drops from ~3500 Wh/kg, according to a material-based calculation, to less than 500 Wh/kg at system-level (**Figure 1.11**).[31]

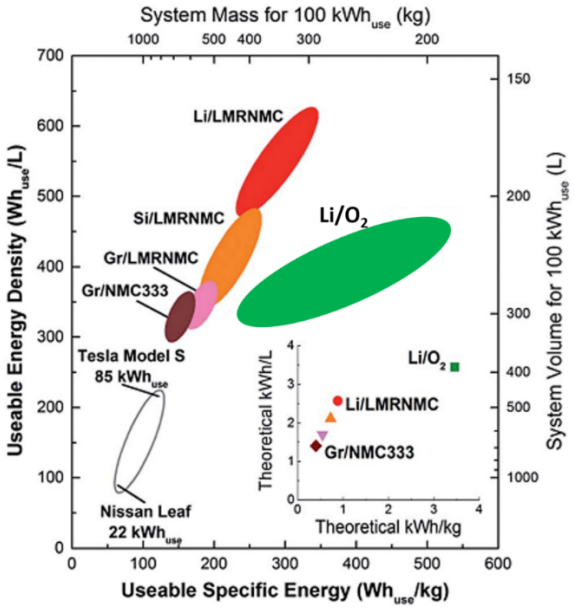

Figure 1.11: Calculated systems-level energy density and specific energy for 100 kWh of useable energy and 80 kW of net power at a nominal voltage of 360 V. (inset) Theoretical specific energy and energy density considering both anode and cathode active materials. MNC333 and LMRNMC refer to NMC and Li- and Mn- rich variation of NMC compounds, respectively. [31]

Apart from the cell design, the discharge product (Li_2O_2) is also a trouble maker. Firstly, due to its low solubility, solid Li_2O_2 accumulates in porous electrode during discharge, causing pore clogging and hindering mass transport. Moreover, as an

insulator, the formed Li_2O_2 on the electrode surface impedes charge transfer, stops electrochemical reactions and thus limits the discharge capacity. The insulating Li_2O_2 is also responsible for the huge voltage gap between discharge and charge, which results in a poor round-trip energy efficiency.

Furthermore, the instabilities of electrolytes and carbon-based electrodes are important issues for both discharge and charge of LOBs. The reactive species formed during discharge (*e.g.* O_2^- and Li_2O_2) attack the solvents and carbon-based electrodes, causing side reactions and generating side products such as Li_2CO_3 and Li oxalate[32,33]. While during charge, carbon corrosion and electrolyte decomposition occur due to the high electrode potential. Side reactions upon cycling damage the electrolyte and electrode, leading to a low coulombic efficiency and poor cyclability of LOBs.

Overcoming the above challenges requires significant research efforts to obtain more comprehensive understandings of the reaction mechanism, to find novel strategies bypassing the intrinsic limitations, to develop more stable electrolytes and electrode materials, and to optimize the structural design at system level.

III. Organization of the thesis

This thesis is organized as follows,

- Chapter 2 discusses in detail the operation principles of non-aqueous LOB and demonstrates the complexity of these systems by revisiting the state of the art ;
- Chapter 3 presents a cell model of the charge process in non-aqueous LOB;
- Chapter 4 reports a cell model of the discharge process in non-aqueous LOB;
- Chapter 5 shows a kinetic Monte Carlo model of the discharge process in non-aqueous LOB;
- Chapter 6 summarizes experimental work attempted to obtain coupling with modeling results;
- Chapter 7 discusses the general conclusions and outlooks of this thesis.

Chapter 2 : State of the Art

In this chapter, we revisit the state-of-the-art of non-aqueous LOB. Important findings on the understanding of the discharge and charge processes are summarized, through which the complexity of the Li-O_2 system is highlighted. The discussion is followed by a review of modeling investigations in this field.

I. Discharge process of non-aqueous Li-O_2 batteries

As previously mentioned, during the discharge process, an insoluble Li_2O_2 deposit is formed and stored in the porous electrode. Once the accumulation of Li_2O_2 reaches a certain extent, it will either fail to maintain the (electronic) charge transport or block the mass (*e.g.* oxygen) transport, leading to the "sudden death" of LOB. The discharge capacity, which is proportional to the amount of Li_2O_2 formed during discharge, shows dependences on current density, electrolyte components and the nature of the positive electrode.

I.1 Impact of current density

The so-called "Ragone plot" represents the relationship between the energy and power of a battery. As shown in **Figure 2.1**, in both Li-$LiCoO_2$ cell and Li-O_2 cells, the specific energy density decreases when the specific power increases, but much larger dependences are found in Li-O_2 cells, regardless of the nature of electrode materials.[34] In Li-ion batteries, the interplay between the energy and power results mainly from the Li^+ transport limitation in electrolyte and in host materials. However, in LOB, not only mass transport but also the electrode passivation is responsible for the energy-power trade-off.

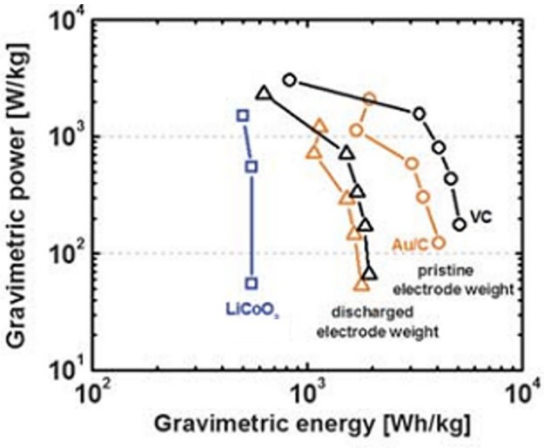

Figure 2.1: Ragone plot for discharges of different Li-O_2 cells with Vulcan carbon (VC) electrode (by pristine electrode weight: black circle; by discharged electrode weight: black triangles), Au/C electrode (by pristine electrode: orange circles; by discharged electrode weight: orange triangles) and of conventional Li-$LiCoO_2$ cell (blue square).[34]

In galvanostatic cycling, the energy of a battery is characterized by the product between the discharge capacity and the cell voltage. The power of the battery is obtained from the product of the current density by the cell voltage. Therefore, the energy-power relationship can be reflected by the evolution of capacity as a function of the applied current density.

Adam *et al*. first reported that by increasing the discharge current density, not only did the discharge capacity decrease but the morphology of Li_2O_2 also changed.[35] Their experiments were performed with electrodes consisting of carbon nanoparticles (**Figure 2.2 a**). At a current density of 5 μA/cm^2, Li_2O_2 was formed as individual toroidal particles (**Figure 2.2 b**), then, when the current density increased to 10 and 25 μA/cm^2, the Li_2O_2 toroidal particles became smaller and thinner (**Figure 2.2 c-d**). Under higher current densities of 50 and 100 μA/cm^2, Li_2O_2 was no longer in toroidal shape; instead, it formed a thin-film on the carbon (**Figure 2.2 e-f**), making the carbon grains larger and reducing the pore volume between grains. The morphological changes of Li_2O_2 were accompanied by the reduction of discharge capacity as displayed by the inserted graphs in **Figure 2.2 b-f**. This current-dependence of discharge capacity and Li_2O_2 morphology were also reported by other groups,[36,37] but sometimes, instead of thin-film deposits, Li_2O_2 formed at high current density was observed in the form of small particles.[38]

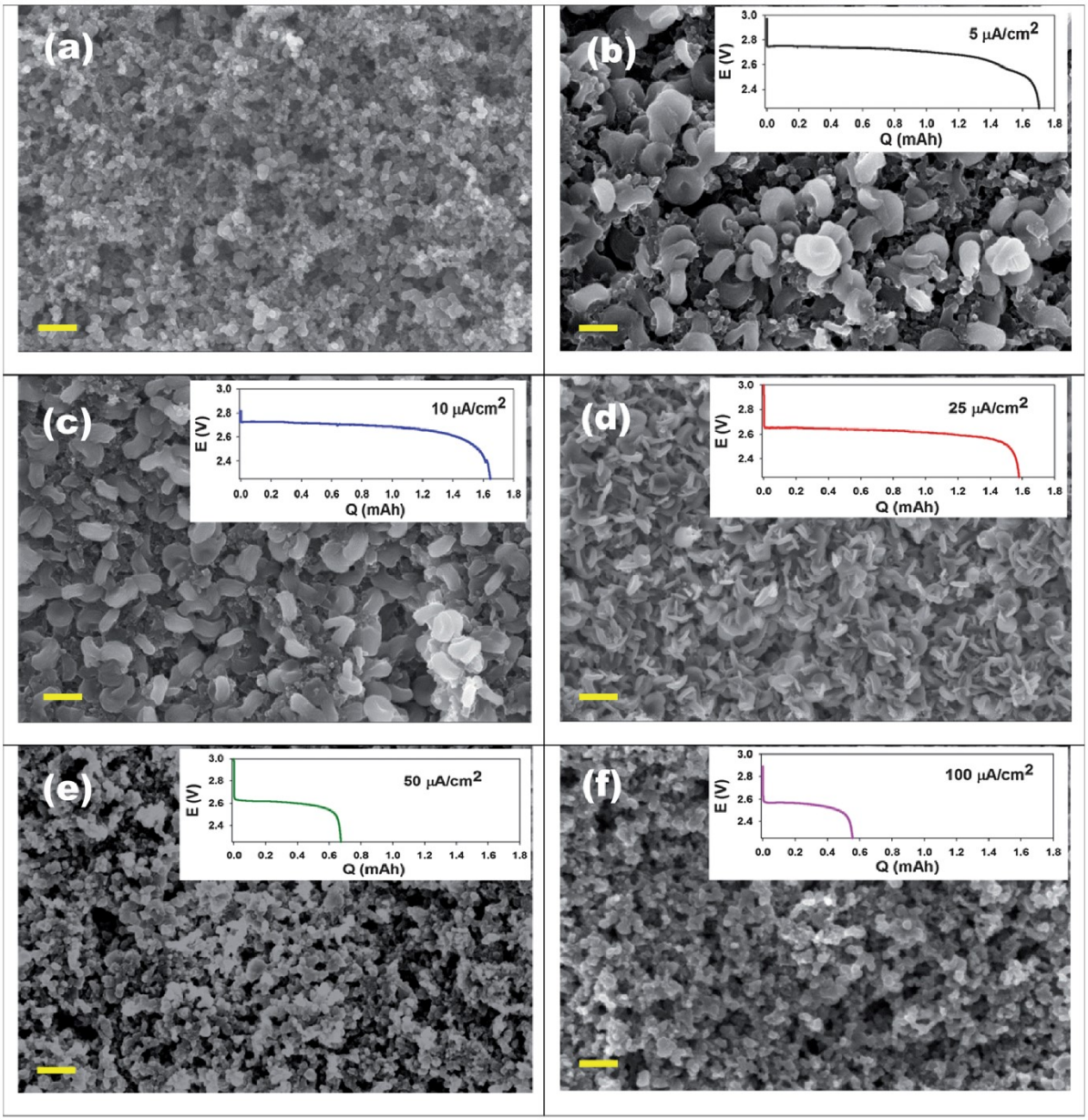

Figure 2.2: SEM images the **(a)** pristine carbon composite electrode and **(b-f)** discharged carbon composited electrodes at current densities of 5, 10, 25, 50 and 100 µA/cm^2, respectively. The inserted graphs display the discharge voltage profiles at each current density. The carbon composite electrodes consist of Vulcan XC72 carbon and Li-Nafion® binder with a carbon/binder weight ratio of 1:1. The electrolyte used in the experiments was 1 M LiTFSI/TEGDME solution. Scale bar = 400 nm.[35]

The Li_2O_2 morphology and discharge capacity are linked to the electrode passivation. When the passivation layer consists of Li_2O_2 thin-film ((**Figure 2.3 a**) or small particles (**Figure 2.3 b**), the thickness and volume of this layer is lower as compared to a passivation layer composed of large Li_2O_2 particles (**Figure 2.3 c**). Therefore, when the electrode passivation is the dominant capacity-limiting factor, the formation of large particles is favorable with respect to a higher discharge capacity.

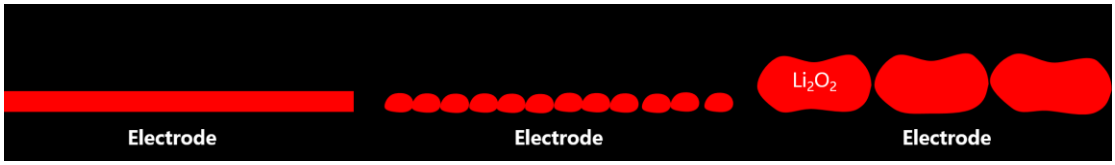

Figure 2.3: Schematic illustration of the electrode passivation process by **(a)** Li_2O_2 thin-film, **(b)** small Li_2O_2 particles and **(c)** large Li_2O_2 toroids.

In the above experiments, the morphological transition of Li_2O_2 from toroidal particles to thin-film happened at a narrow current range from 25 to 50 µA/cm^2, which was consistent with the sudden increase of discharge capacity at the same current range (**Figure 2.4**). Similar "switch" in Li_2O_2 morphology was also found by other groups.[36–38] Horstmann *et al*. developed a nano-scale continuum model to study this morphology transition using non-equilibrium thermodynamics. Their model predicted that this transition would take place at current densities that are two orders of magnitude larger than the exchange current density.[3]

Moreover, Adam *et al.* pointed out that the discharge current density influenced Li_2O_2 crystallinity. **Figure 2.5** shows the X-ray diffraction (XRD) patterns of the discharged electrodes at different current densities. Crystalline Li_2O_2 were detected in all cases but the intensities of reflections are largely reduced at current densities of 50 and 100 µA due to less amount of deposits. However, with similar capacities, the Li_2O_2 diffraction intensities at 100 µA were still significantly lower than at 50 µA, indicating that less crystalline Li_2O_2 and more amorphous Li_2O_2 was formed at 100 µA.

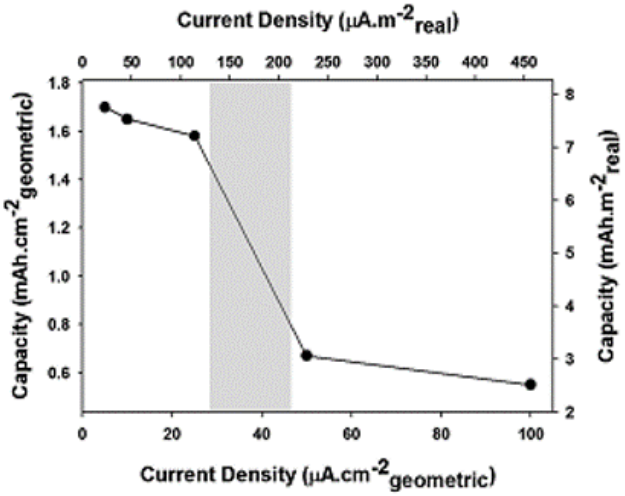

Figure 2.4: Variations of discharge capacity as a function of discharge current density.The subscript "real" in the units of capacity and current density means the values are reported with respect to the real surface area of carbon.[35]

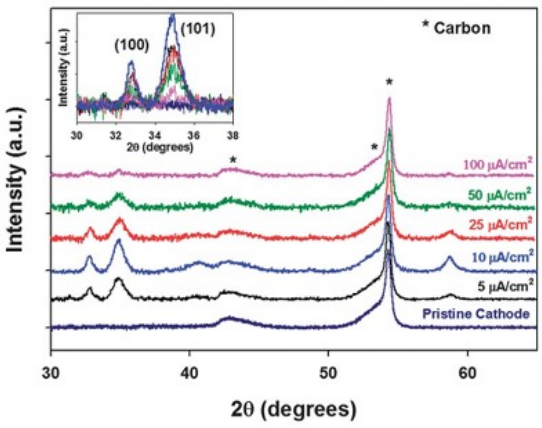

Figure 2.5: XRD patterns of discharged electrodes at various discharge current densities. All peaks, except those due to carbon (*), can be indexed to Li_2O_2.[35]

I.2 Impact of the electrolyte

I.2.a. Impact of the solvent

Various types of solvents, such as carbonates,[39,40] ethers,[41,42] DMSO,[43–45] DMA[46] and ionic liquids[47,48] have been employed in electrolytes for LOB. It is found that the discharge capacity depends strongly on the electrolyte solvent. This has been explained in detail in the discharge mechanism as proposed by Lee *et al.*[49]

As shown in **Figure 2.6**, it was recognized that the first step of O_2 reduction in non-aqueous solvent, in the presence of Li^+, involved the formation of superoxide LiO_2 as intermediate through the following reaction,[50–52]

$$Li^+ + e^- + O_2 \rightarrow LiO_2 \qquad 2.1$$

The superoxide LiO_2 can either be adsorbed on the electrode surface, marked as LiO_2^*, or dissolve in electrolyte, noted as $LiO_{2(sol)}$, which can be in the form of free ions, but more likely as ion pairs[53] and higher aggregate.[53,54] LiO_2 can convert into Li_2O_2 via electrochemical reduction

$$LiO_2 + Li^+ + e^- \rightarrow Li_2O_2 \qquad 2.2$$

or chemical disproportionation:

$$2LiO_2 \rightarrow Li_2O_2 + O_2 \qquad 2.3$$

The former reaction pathway involves another electron transfer from the electrode and usually takes place with LiO_2^* close to the electrode surface, so it is called “surface mechanism”. The later reaction pathway does not rely on the electrode surface and can occur in the solution with $LiO_{2(sol)}$, thus it is known as “solution mechanism”. Due to the charge transfer limitation, Li_2O_2 formed from the surface mechanism is usually in the form of small particles or a thin-film. By contrast, the Li_2O_2 particles generated through the solution mechanism could be very large and relatively further away from the electrode. Compared to the surface mechanism, the solution mechanism can delay the electrode passivation and form more Li_2O_2. Thus, the solution mechanism is favored with respect to a larger capacity.

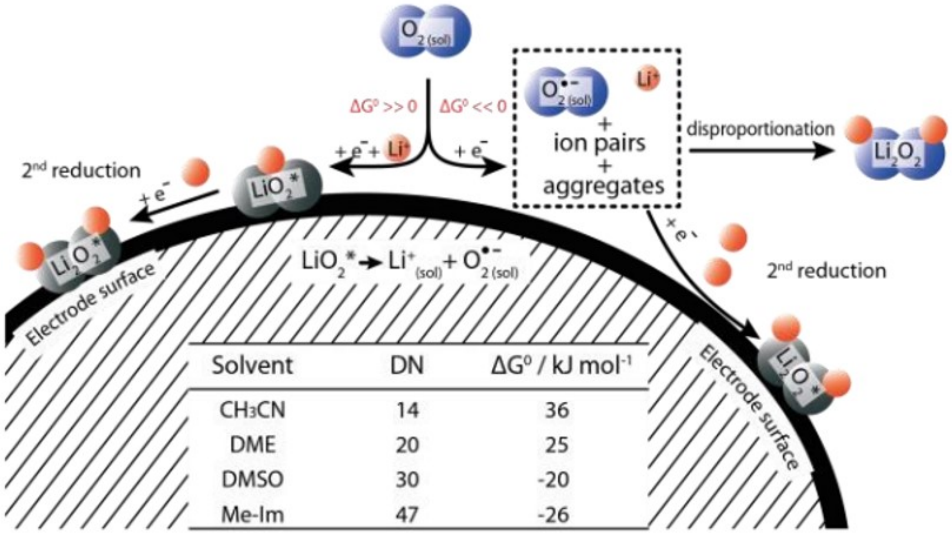

Figure 2.6: Schematic illustration of O_2 reduction in non-aqueous solvents containing Li^+ following the surface mechanism when $\Delta G^o > 0$ (low DN) and the solution mechanism when $\Delta G^o < 0$ (high DN). The inserted table displays the DN and ΔG^o of different solvents. ΔG^o is the Gibbs free energy difference between LiO_2^* and $LiO_{2(sol)}$ in the same solvent.[49]

The competition between the solution and the surface mechanisms depends on the equilibrium between LiO_2^* and $LiO_{2(sol)}$ as follows

$$LiO_2^* \leftrightarrow LiO_{2(sol)} \qquad 2.4$$

The above equilibrium is influenced by the solvent donor number (DN), a concept proposed by Gutmann, which is a quantitative measure of Lewis basicity.[55,56] In high-DN solvents, due to the strong solvation of Li^+, the Gibbs free energy of $LiO_{2(sol)}$ formation is higher than that of LiO_2^*, and the equilibrium shifts to the right side. Consequently, Li_2O_2 is mainly formed through solution mechanism, resulting in high discharge capacity. In low-DN solvent, the Li^+ solvation is weak and the Gibbs free energy of $LiO_{2(sol)}$ formation is lower than LiO_2^*. Thus, the equilibrium moves to the left side and Li_2O_2 is predominantly formed via surface mechanism, leading to low discharge capacity. As shown in **Figure 2.7**, the discharge capacity is in good accordance with the DN of the solvents.

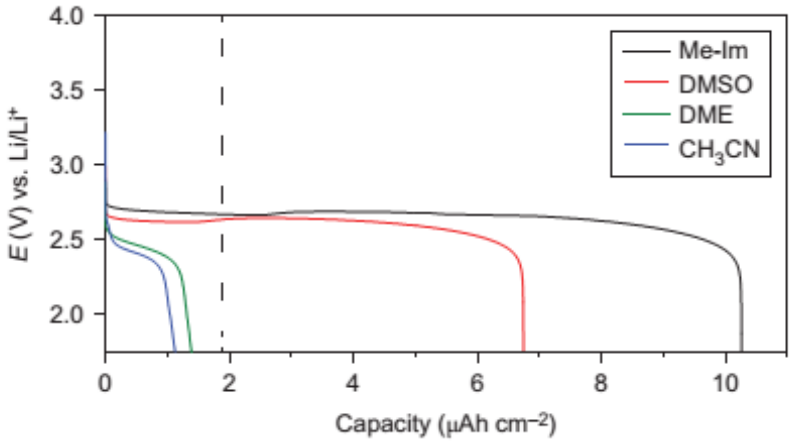

Figure 2.7: Discharge profile of a planar Au electrode at 60 μA/cm^2 in various O_2-saturated aprotic solvents and 100 mM $LiClO_4$.The dash line indicates the discharge capacity correlated to the formation of a 7 nm uniform Li_2O_2 thin-film on electrode.[49]

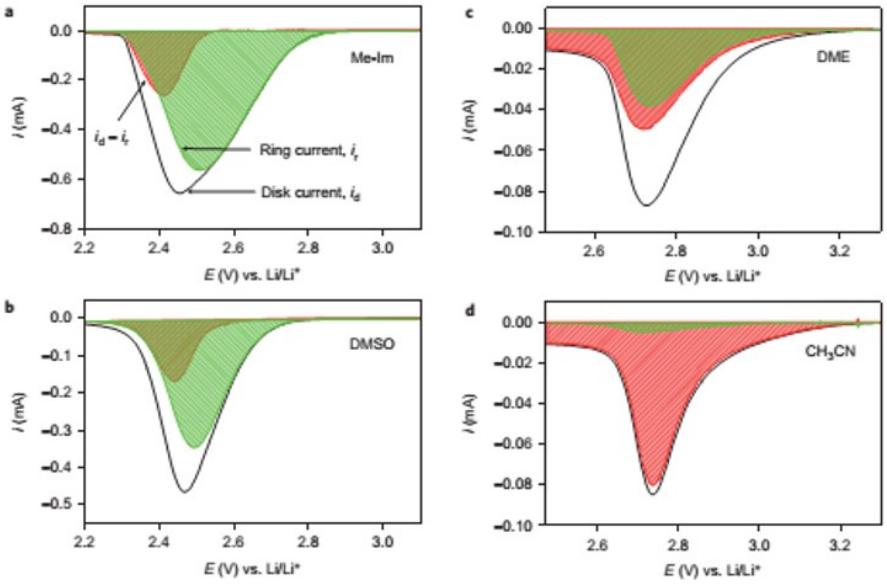

Figure 2.8: Current-voltage curves obtained in O_2-saturated Me-lm (a), DMSO (b), DME (c) and CH_3CN (d) containing 100 mM $LiClO_4$: black line disk current i_d ; green area, ring current i_r (presented as a negative current); red area, $i_d - i_r$.[49]

The impact of the solvent DN on the LiO_2 solubility has been confirmed by rotating ring disk electrode (RRDE) experiments (**Figure 2.8**).[49] The disk current (i_d) in RRDE measurement was generated from the reduction of O_2 and LiO_2, while the ring current (i_r) corresponded to the $LiO_{2(sol)}$ oxidation. When the concentration of $LiO_{2(sol)}$ was increased, i_r became larger. In high-DN solvent (Me-lm and DMSO), the i_d and i_r were found to be comparable, indicating a relatively high LiO_2 solubility. But in low-DN solvent (DME and CH_3CN), i_r was much smaller and even absent, proving that LiO_2 solubility was low in these solvents.

I.2.b Impact of salt

Similar to the solvent, the counter anion of the electrolyte salt could also affect the Li^+ solvation and $LiO_{2(sol)}$ solubility, thus it exerts influences on the discharge mechanism, particularly in low-DN solvents.[57–59] Gunasekara *et al.* found that a cell with $LiCF_3SO_3$/TEGDME showed higher discharge capacity than one with $LiPF_6$/TEGDME.[60] The combined results from RRDE and IR spectra suggested that this higher capacity in $LiCF_3SO_3$ electrolyte was due to the increased solubility of the LiO_2 ion pairs as stabilized by high DN $CF_3SO_3^-$. Sharon *et al.* further correlated the impact of the salt anions to its ionic association strength (AS), which describes the interaction between the counter anions of the salt and Li^+.[57] In low-DN solvents such as diglyme, the counter anion in high-AS salt stayed in the solvation shell, stabilized the LiO_2 ion pairs so they had a higher chance to diffuse away from electrode, then formed Li_2O_2 in solution via solution mechanism. For low-AS salts, the counter anion was excluded from the solvation shell, failing to stabilize the LiO_2 ion pair. In this case, the Li_2O_2 was formed via the surface mechanism. Therefore, as shown in **Figure 2.9**, the discharge capacities in low DN-diglyme based electrolyte were enhanced with increasing the AS of salt anion in the order $TFSI^- < FSI^- < Tf^- < Br^- < OAc^- < NO_3^-$.

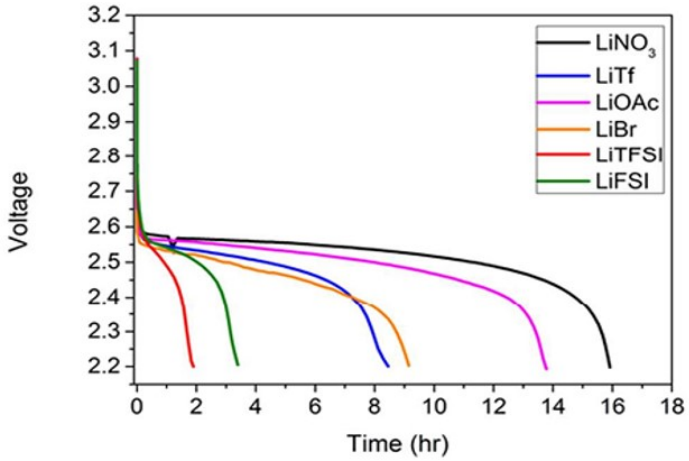

Figure 2.9: The discharge curves of Li-O_2 batteries with electrolytes based on diglyme solvent and different salts. The ionic association strengths of the salt anions were in the following order: $TFSI^- < FSI^- < Tf^- < Br^- < OAc^- < NO_3^-$. In all cases, the salt concentrations were 1 M and the discharge current densities were 3 μA/cm^2.[57]

Apart from the salt type, the salt concentration of the electrolyte also impacts the discharge performance of non-aqueous LOB. Liu *et al.* investigated the salt concentration effects in LiTFSI/DME electrolytes.[61] They showed that high-concentration electrolytes could mitigate the electrolyte decomposition and thus improve the stability and reversibility of LOB. However, Marcus *et al.* reported different effects of the same electrolytes, showing that high-concentration electrolyte can result in cathode passivation due to increased salt decomposition.[62] According to the authors, low-concentration electrolytes with more stable Li salts would be a better choice to reach better performances.

Mohazabrad *et al.* found that the viscosity and ionic conductivity of LiTFSI/TEGDME electrolytes changed with salt concentration, which could account for the dependence of LOB discharge capacity on electrolytes as well.[63] At low salt concentration (≤0.25 M), the discharge capacity was extremely low due to insufficient Li^+ and its slow diffusion. The discharge capacity was improved significantly when the salt concentration was higher than 0.25 M. However, typically, the O_2 solubility decreases when more salt is added in the electrolyte. At the same time, the O_2 transport slows down due to the increase of the electrolyte viscosity.[64] The effects of O_2 solubility and transport property led to a slight decrease of capacity when the salt concentration increased from 0.75 M to 1 M. Moreover, it is found that optimized salt concentration,

which was determined by the balance between ionic conductivity and mass transport, depended on the current density. At lower current density (< 0.2 mA/cm^2 in their experiments), the highest discharge capacity was obtained with 0.75 M electrolyte; while at high current density (0.3~0.5 mA/cm^2), the highest capacity was obtained with 1 M electrolyte.

I.2.c Side reactions of the electrolyte

In the early investigations, carbonate-based electrolytes, which were commonly used in Li-ion batteries, were also used in non-aqueous LOB.[30,39,65,66] However, it was found that discharge products were in fact Li_2CO_3 instead of Li_2O_2. Later on, it is reported that this Li_2CO_3 stems from the decomposition of the carbonate solvent upon cycling.[67–69] Since then, other electrolytes, such as ether-based electrolytes and DMSO-based electrolyte were employed and Li_2O_2 was then found as the predominate discharge product.[42,43,70,71]

Nevertheless, side reactions were still found in various electrolytes. Younesi *et al.* reported the instability of DMSO when it was in contact with Li_2O_2 for 2 days.[72] As a result, DMSO decomposed to form carbonate species through a reaction between the methyl of DMSO and Li_2O_2. Oxygen-containing compounds like LiOH, with lower oxidation state as compared to Li_2O_2, were detected on the surface of Li_2O_2. Moreover, the glymes, such as DEM and TEGDME, were reported to be stable against superoxide radicals as evidenced by their stability when in contact with KO_2.[73,74] But the autoxidation of glymes causes their degradation in LOB. [69, 75]

Apart from the solvent, some salts suffer from instability issues. For example, it was reported that the LiBOB and $LiBF_4$ decomposed during discharge to form Li borates, Li oxalate in the former and LiF in the latter case.[76]

The common byproducts from electrolyte decomposition are carbonates, which are insoluble in the electrolyte and even harder to decompose than Li_2O_2. Thus, the accumulation of carbonates on the electrode surface aggravates the electrode passivation, increases the charge voltage and reduces the discharge capacities upon cycling. This indicates that finding a stable electrolyte for LOB is still a key challenge.

I.3 Impact of the positive electrode

Both of the chemistry and texture of the positive electrode materials can impact the operation of the LOB.

I.3.a. Impact of the electrode chemistry

Various types of carbon materials, including mesoporous carbon,[51,66,77] carbon nanotube (CNT) [78–80] and graphene[81–83], are widely used in LOBs as positive materials. The advantages of carbon materials include a high electronical conductivity, light weight, relative low cost and environmental benignity. As the electrochemical reactions take place on the electrode surface, the surface chemistry of the carbon impacts the discharge performances. Wong *et al.* reported that the removal of the surface groups of the carbon materials enhanced the discharge capacity of LOBs (**Figure 2.10**).[84] This is due to the fact that the –OH and –COOH surface groups may bind LiO_2 to the electrode surface and thus favor the surface mechanism during the discharge process, which is in agreement with the dependence of O_2 reduction on the defect content of the carbon surface as reported by Belova *et al.*[85]

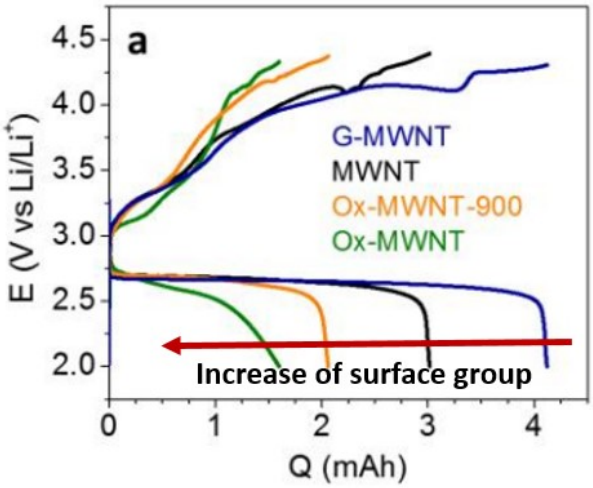

Figure 2.10: Galvanostatic discharge and recharge profiles of the first cycle performed with electrodes made from different multi-wall nano-tube (MWNT) carbons.[84]

However, the carbon-based electrodes are not stable during the charge, resulting from the reaction with Li_2O_2.[32] This carbon corrosion occurs mainly during charge at a

relative low potential (U > 3.5) and forms Li_2CO_3 or Li carboxylate.[86] Towards a higher stability, some new electrode materials were proposed. For instance, Peng *et al.* reported an nano-porous gold electrode which can give 100 cycles in $LiClO_4$/DMSO with a yield of Li_2O_2 that was higher than 99 %.[87] TiC was used as positive electrode of LOBs by Thotyl *et al*., which was demonstrated to significantly reduce largely the side reactions.[88]

The change of electrode materials may lead to the variation of the discharge pathway. Combining RRDE measurement and differential electrochemical mass spectrometry (DEMS), Reinsberg *et al.* elucidated different pathways for the Li_2O_2 formation on gold, platinum and glassy carbon electrode.[89] It is found that while the oxygen reduction on glassy carbon and Pt takes place via the parallel formation of LiO_2 and Li_2O_2, there is a distinct transition between LiO_2 and Li_2O_2 formation on the gold electrode. This transition occurs close to a potential where the LiO_2 formation is mainly limited by the diffusion. The difference of discharge path may be correlated to different binding strengths of O_2 on these materials.

I.3.b. Impact of the electrode texture

The positive electrodes of LOBs are porous so as to store the insoluble discharge product Li_2O_2 and provide active surface for the electrochemical reactions. Specific surface area (m^2/g), pore size and pore volume (m^3/g) are three main electrode textural features, which influence the discharge performance.

By investigating seven different porous carbons as positive electrodes in LOBs, Meini *et al.* found a linear correlation between the discharge capacity and specific surface area of the carbon materials (**Figure 2.11)**.[90] This suggests that the electrode passivation is the main capacity limiting factor. A similar capacity increase with high surface electrode was observed by Cheng *et al*. [91] and Hayashi *et al* [92]. The authors concluded that large surface carbon materials can be beneficial to reach high discharge capacities.

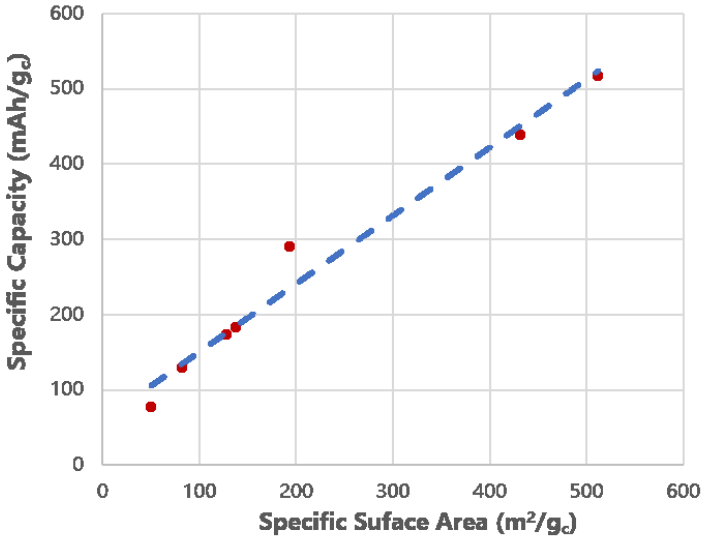

Figure 2.11: The discharge capacity as a function of the specific surface area of the carbon. This figure is re-plotted with data withdrawn from ref. [90].

Ma *et al*. reported that the efficiency of Li_2O_2 deposition in mesoporous carbon aerogel is higher than that in microporous carbon.[93] It is found that as much as 61% of pore volume of carbon aerogel was filled with Li_2O_2 while it is less than 18% at the end of discharge in activated carbons. Therefore, despite a lower specific surface, carbon aerogels showed a larger discharge capacity than activated carbons. The effect of pore size on the discharge performance has also been investigated by Ding *et al*.[94] By using spherical silica as templates, the authors prepared carbon materials with pore sizes in the range of 20 to 100 nm and tested them as positive electrodes in LOBs. The results revealed that the discharge capacity increased with the increase of pore size and reached its maximum at a pore size of 80 nm. The lower capacity in smaller pores has been attributed to a more serious pore shrinking or even clogging due to the accumulation of Li_2O_2. The decrease of capacity in pores larger than 100 nm was due to a lower specific surface area. Moreover, Miranda *et al*.[95] reported that discharge reactions and pore clogging took place preferentially in the closest proximity to the oxygen inlet as shown in **Figure 2.12**. This clogging of the oxygen inlet hindered the full exploitation of pore volume and active surface, thus resulting in a weak discharge capacity.

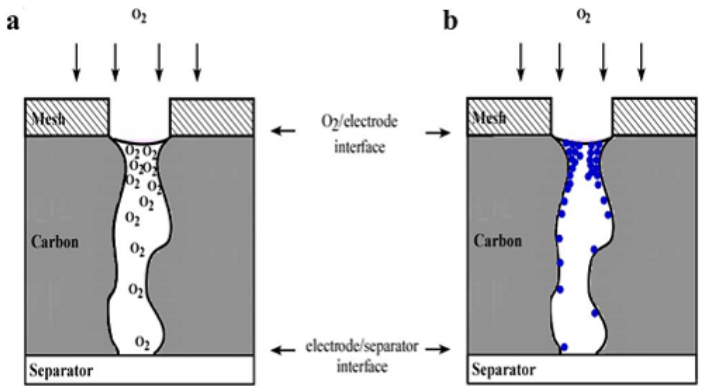

Figure 2.12: Schematic representation of the oxygen electrode (a) before and (b) after discharge.[95]

Recently, Sakai *et al*. used mesoporous carbon gels with different pore size distributions as model cathodes to study the pore-filling by Li_2O_2 during the discharge process.[96] It is found that regardless of the pore size, the volume ratio of the Li_2O_2 deposits in fully discharged cathodes with respect to the meso- and macro-pore volume of cathode was in the range of 0.5–0.6 and was fairly constant among the samples. This highlighted the importance of pore volume in determining the discharge performance of Li_2O_2.

The optimization of the electrode texture is not trivial due to the complicated relationships among specific surface area, pore size, and pore volume. On one hand, large specific surface area requires small pores which have a high surface-to-volume ratio; on the other hand, large pores as well as the good interconnectivity between pores are critical to ensure the O_2 transport. In addition, the tailoring of the electrode texture may cause modifications of the surface chemistry, which even increased the complexity of electrode optimization.

I.3.b. Comments on the capacity representation

Conventionally, the discharge capacity in LOBs are reported as mAh/g. However, there is a lack of standardized protocol about which masses should be included. In some cases, the capacity is reported with respect to the mass of the composite electrode,[97] in some other cases, only the mass of catalyst is considered[40] and many times there is no specification of the meaning of mass.[76,93] These scattered

representation results in the difficulty to compare the cell performances reported in different papers.

Moreover, the mass of the electrode components may not be the most relevant metric as the discharge capacity depends only on the amount of formed Li_2O_2. Except for comparing the same electrode under different conditions, little information can be provided by the capacity with respect to the mass of the electrode components. In this context, other capacity reporting method could be better. For example, reporting capacity with respect to the total surface area of the electrode material can imply the dominant discharge mechanism in the system, because the capacity from surface mechanism is proportional to the total surface area. Another approach is to report the capacity with respect to the pore volume, wherein the efficiency of pore utilization can be reflected by the discharge capacity.

II. Charge process in non-aqueous Li-air batteries

II.1 Charge transport across Li_2O_2

Crystalline Li_2O_2 is an insulator with a large band gap ~5 eV.[98] Combining electrochemical experiments and Density Functional Theory (DFT) calculations, Viswanathan *et al.* suggested that the charge transport through Li_2O_2 thin-film was dominated by the tunneling of holes and there is a critical thickness of Li_2O_2 deposit around 5 to 10 nm, above which the tunneling current is insufficient to support the electrochemistry.[99] According to the authors, this critical tunneling distance is the origin of the potential drop, known as “sudden death”, at the end of the discharge.

However, it is widely observed that Li_2O_2 is indeed decomposed during the charging process despite a size much larger than the critical tunneling distance. This suggests other mechanisms accounting for the necessary charge transfer during the charge process.

Based on DFT calculations, Radin *et al.* reported that the O-rich surface of Li_2O_2 shows metallic behavior in spite of the insulating nature of the bulk phase, which implies that surface conduction may be a possible way for electron transport in Li_2O_2 particles.[100] Later on, Geng *et al.* further showed that electronic structure of the O-rich grain boundary of Li_2O_2 is similar to the free surface.[101] As the Li_2O_2 is always polycrystalline, the electron can then be transferred through the large Li_2O_2 particle via

the inner grain boundary. These two mechanisms should have the same impact on both discharge and charge process. Nevertheless, the implementation of the surface conduction and boundary conduction leads to failure in explaining the "sudden death" phenomenon at the end of the discharge process.

Another possible charge transfer mechanism in Li_2O_2 is via the polaron hopping, particularly, hole polaron hopping. According to the theoretic calculation, the barrier for the hole polaron migration is only ~0.1- 0.2 eV, which is low enough to support the charge transport in Li_2O_2.[102] Since polaron hopping could be enhanced by increasing the potential bias, its preferential appearance during the charge process could be ascribed to the higher overpotential.

In addition to Li_2O_2 in crystalline form, Tian *et al* investigated the electron transport in amorphous Li_2O_2 through first-principle calculation.[103] They found that amorphous Li_2O_2 has a much higher electronic conductivity and an even higher ionic conductivity compared to crystalline Li_2O_2. This theoretical prediction has been confirmed in experiments by Zhang *el al.*[104]

II.2 Proposed mechanisms for the charge process

While the discharge profiles in LOBs are similar in most of cases, the shape of the charge profiles depends on electrolyte components and electrode materials (**Figure 2.13**). The difference in charge profiles may imply the occurrence of different processes, however the reason for this diversity is not clear yet. Different mechanisms have been proposed and updated with new evidences, but until now, there is a lack of consensus.

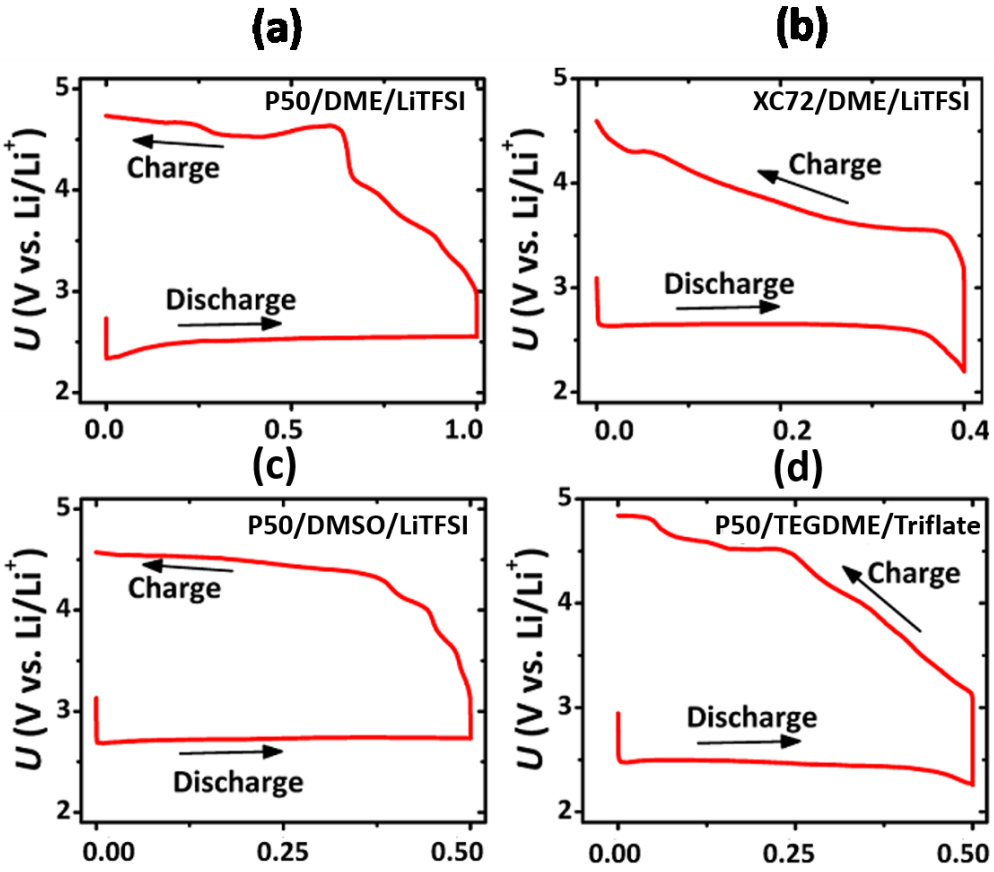

Figure 2.13: Discharge-charge profiles of different carbon electorde/solvent/salt combinations In all cases, the salt conetrations are 1 M.[86]

McCloskey *et al*. proposed a simple kinetic model of the charge process of LOBs (**Figure 2.14 a**).[105] In this model, the Li_2O_2 oxidation kinetics was assumed to be proportional to its surface concentration. Due to the continuous formation and accumulation of carbonate product from the electrolyte decomposition, Li_2O_2 surface concentration was decreasing during the charge process, consequently increasing the charge potential. Once reaching above 4V, carbonates byproducts start to decompose, resulting in the flat voltage plateau. The simulation results fitted well with the experimental results (**Figure 2.14 b**). However, uniform thin film assumption of Li_2O_2 is neither consistent with inhomogeneous distribution of Li_2O_2 in electrode, nor the particle morphology of the Li_2O_2 formed via the solution mechanism.

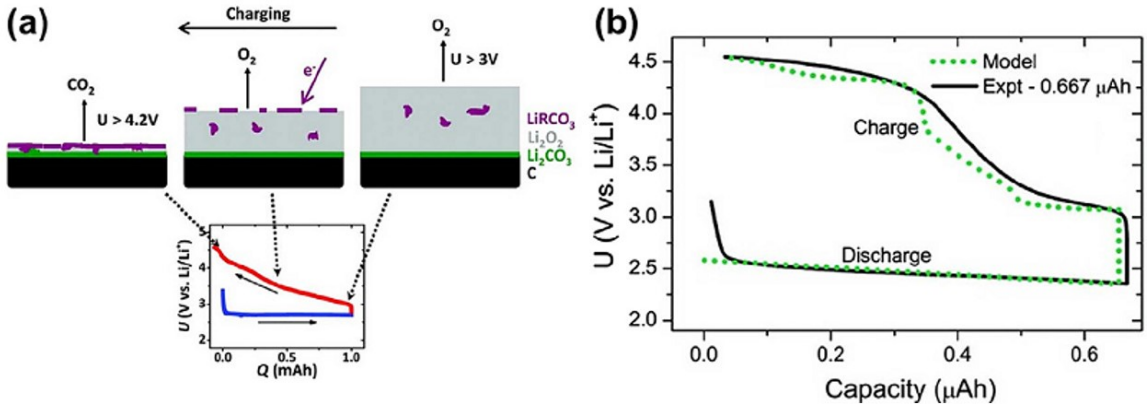

Figure 2.14: (a) Schematic illustration of the charge process with carbonate formation; (b) Comparison between experimental and modeling results.[105]

Through DFT calculations, Kang *et al.* proposed a charge mechanism for LOBs.[106] This mechanism is based on the formation of the off-stoichiometric $Li_{2-x}O_2$ compound, which has a relative low formation energy of ~0.3-0.4 eV. With increasing x, the compound became more unstable and readily to release O_2. Those particles that were charged earlier released Li^+ and O_2 during the decomposition. The increase of local Li^+ and O_2 concentration reduced the local potential and prevented the nearby Li_2O_2 from reacting until the excess Li^+ and O_2 was removed by diffusion. This suggested that the charging of Li_2O_2 could be a particle-by-particle inhomogeneous process (**Figure 2.15**), which is contradictory to the experimental observations.[107]

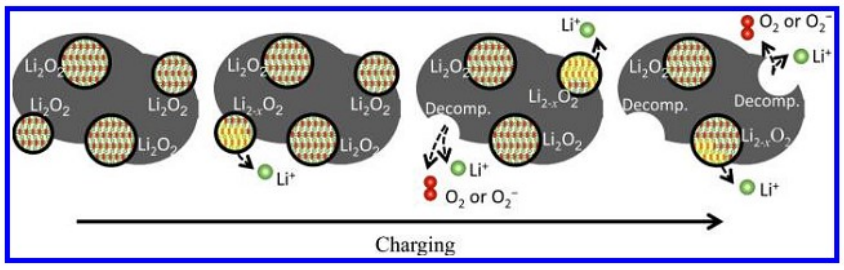

Figure 2.15: Schematic illustration of the off-stoichiometric mechanism of charging in Li-O_2 batteries.[106]

Lu *et al.* reported a charge profile where the electrode potential increased gradually and then it was followed by a voltage plateau (**Figure 2.16**).[108] The sloping voltage region has been attributed to the decomposition of the outer layer of the Li_2O_2 through a solid-solution route, in which LiO_2-like component was formed first through delithiation, then decomposed via disproportionation. The voltage plateau was linked to the direct decomposition of the bulk Li_2O_2 via two-phase transition and the voltage plateau at the end of the charging was ascribed to the side reaction such as carbonate decomposition. However, how the solid-solution route changes to the two-phase route is not explained by the authors.

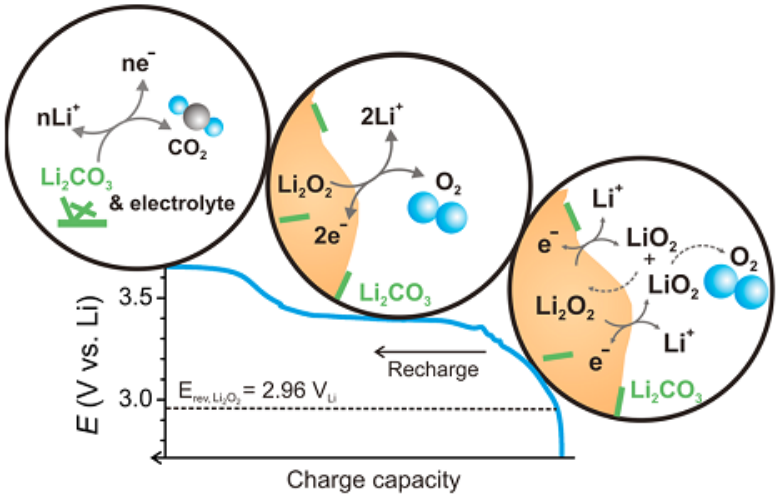

Figure 2.16: Schematic illustration of the charging mechanism of Li-O_2 batteries as proposed by Lu *et al.* [109]

The charge profile obtained by Zhai *et al.* comprises two plateaus, which were correlated to the decomposition of LiO_2 and Li_2O_2, respectively.[107] According to the authors, the LiO_2 formed during discharge was not completely reduced to Li_2O_2 before charge process started. The remaining LiO_2 was decomposed at lower voltage plateau during the charge process, followed by the oxidation of Li_2O_2 at the high voltage plateau. The existence of LiO_2-like component on the surface of Li_2O_2 toroidal particles has been confirmed by Raman spectrometry.[110] It was also found that the peak related to the superoxide species in Raman spectra disappeared when the electrode was charged back to the high voltage plateau. Nevertheless, the one-electron decomposition does not

agree with the DEMS results where a $2e^-/O_2$ ratio was measured for the charging process.[86]

Combining operando X-ray diffraction and Rietveld refinement, Ganapathy *et al.* proposed a two-stage oxidation for Li_2O_2 formed during discharge. As shown in the **Figure 2.17 a**, during the first stage of charge, the integrated area under the Li_2O_2 reflections remained constant, indicating the preferential decomposition of surface LiO_2 or/and amorphous Li_2O_2. The integrated area under Li_2O_2 reflections decreased linearly during the second stage of charge, implying the oxidation of the Li_2O_2 particles. Therefore, this suggested that amorphous Li_2O_2 was oxidized at low voltage, whereas crystalline Li_2O_2 was decomposed at high voltage.

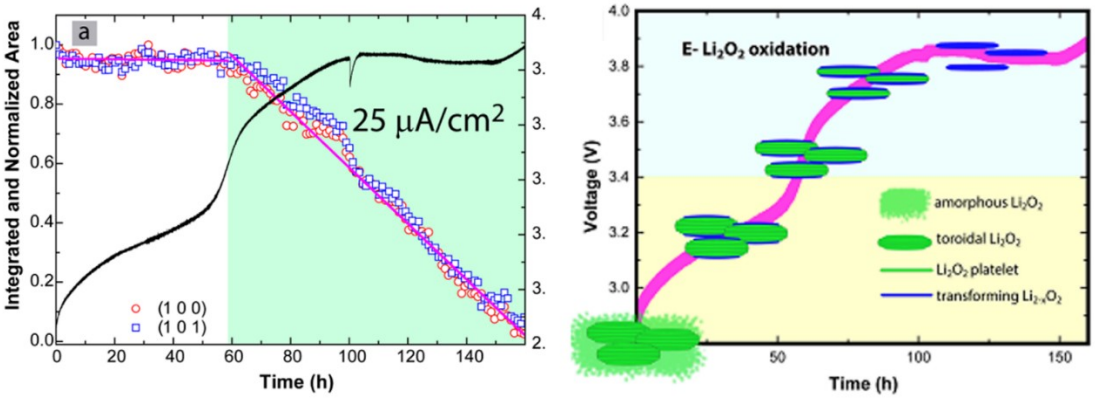

Figure 2.17: (a) Galvanostatic charging of a Li-O_2 cell at current density of 25 μA/cm^2. Integrated and normalized areas under the crystalline Li_2O_2 (1 0 0) and (1 0 1) peaks is plotted as a function of charge time. The pink lines indicate the linear fit of the points. **(b)** Schematic illustration of the charge mechanism of electrochemical-formed Li_2O_2 f as proposed by Ganapathy *et al.*[111]

II.3 Impact of the heterogeneous catalyst

The charge process of the LOBs is characterized by its high potential (3.5 ~ 4.2 V) and overpotential (0.5 ~ 1.3 V). This high overpotential leads to a large voltage gap during cycling, resulting in a low round-trip efficiency. Besides, charging at high voltage can cause carbon corrosion[32,86] and electrolyte decompostions.[32,86] Therefore, it is crucial to minimize the charge overpotential.

In fuel cells, heterogeneous catalysts, such as Pt nanoparticles and Pt alloys, play an important role in reducing the overpotential of the oxygen reduction reaction.[112] Along the same line, various catalysts have been proposed for LOBs with the hope of decreasing the charge overpotential, such as precious metals and their oxides,[40,113] transition metals and their oxide[78,114,115,115]. For example, Lu *et al*. systematically investigated the catalytical impacts of Pt-Au nanoparticles. They found that by loading the Pt-Au catalyst on the carbon electrode, the charge potential can be reduced by 900 mV. [81] Qin *et* al. incorporated MnO_2 nanorods into porous carbon and the as prepared MnO_2/C composites showed a charge potential of 3.5 V which was lower than the pure porous carbon materials.[116]

However, as pointed out by McCloskey and Addison, the impact of heterogeneous catalysts on the charge kinetics could be limited due to the insoluble nature of Li_2O_2.[117] It is difficult to envision how the Li_2O_2 formed away from the catalysts reaches the active site of the catalyst. So, instead of directly participating in the charge process, heterogeneous catalysts may reduce the charge potential via other mechanisms, such as by tuning the crystallinity of the Li_2O_2. Yang *et al* reported that while Li_2O_2 formed on catalyst-free graphene was crystalline, Li_2O_2 formed on Pd-loaded graphene was amorphous.[118] As amorphous Li_2O_2 has a higher electrical conductivity than crystalline phase, the former can be oxidized at lower voltage than the latter.[103,104] Therefore, the charge potential in the Pd-loaded LOBs was lower than those with graphene electrode.

However, the loading of catalysts does not always bring benefits to the battery performances. With DEMS measurement, McCloskey *et al* found that there was more CO_2 released during the charge process when Pt nano-particles were used as catalysts, indicating that Pt could also catalyze the solvent decomposition.[119]

II.4 Homogeneous catalysis with redox mediators

Very recently, there is a new trend of exploiting redox mediators as homogeneous catalysts in LOBs to enhance the discharge capacity and more importantly, to decrease the charge overpotential. [82,120–123] Redox mediators are small molecules dissolved in the electrolyte and have a redox potential close to that of Li_2O_2 formation or oxidation.

Gao *et al.* reported a redox mediator DBBQ (2,5-di-*tert*-butly-1,4-benzoquione), which has a slightly lower redox potential than Li_2O_2. Thus instead of reducing on the electrode surface, O_2 could be reduced by DBBQ in the solution and further form Li_2O_2 through solution mechanism (**Figure 2.18**).[121] As a result, the solution mechanism has been improved by the redox mediator even in low DN solvent, leading to a much higher discharge capacity.

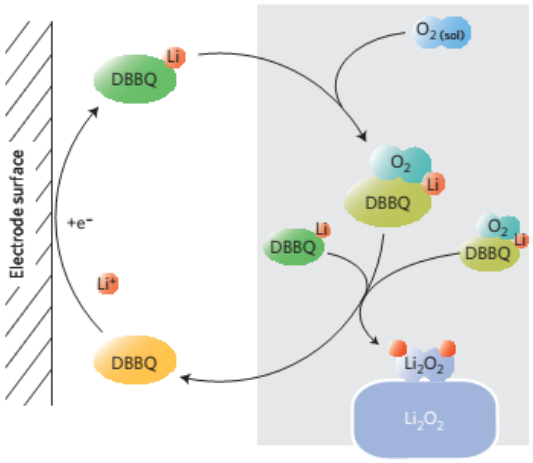

Figure 2.18: Schematics illustration of discharge process in Li-O_2 batteries with presence of redox mediator DBBQ.[121]

Some redox mediators, such as LiI and LiBr, could work on the opposite direction during the charge process owning to their redox potentials that are slightly higher than the Li_2O_2 oxidation potential.[122–124] Under the oxidized form (R^+), the redox mediator could oxidize Li_2O_2 to O_2 and Li^+, and the resulting reduced form is regenerated on the electrode surface as shown in **Figure 2.19 a**. Consequently, with the addition of redox mediator, the oxidation of Li_2O_2 shifts from an electrochemical pathway to a chemical pathway, bypassing the high overpotential due to the electron transfer limitation in large Li_2O_2 (**Figure 2.19 b**).

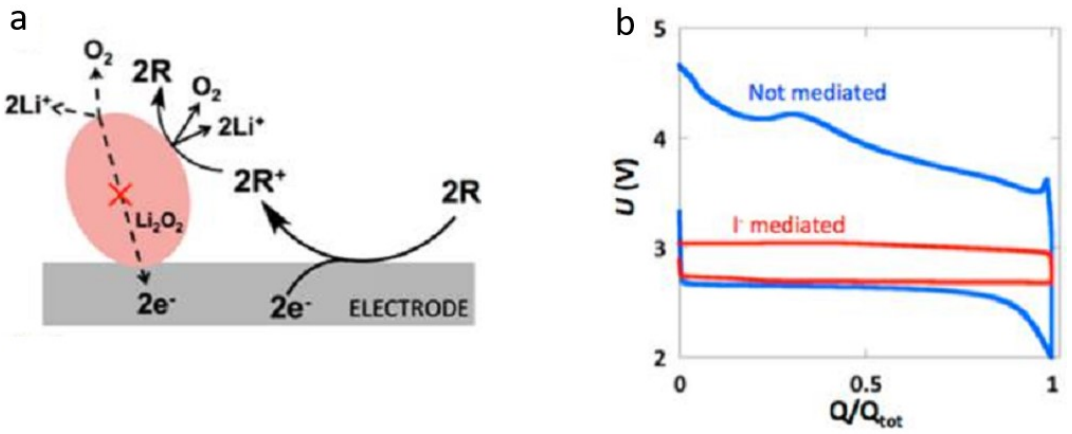

Figure 2.19: (a) Schematic illustration showing the mechanism of Li_2O_2 oxidation with presence of redox mediator; **(b)** Discharge/charge curves of Li-O_2 batteries with (blue) and without (red) I^- as redox mediator.[117]

Despite of their effectiveness, redox mediators are facing the stability issue. It is reported that some redox mediators degrade during the operation of battery and promote LiOH formation.[82,123] Thus, caution should be exercised to interpret the impacts of redox mediator and more efforts should be made to improve their stability.

III. Modeling of Li-O_2 batteries

Modeling is the process to interpret a physical system. In a model, a set of mathematical equations are written computationally solved to simulate the physical system behavior (**Figure 2.20**).[125] With the development of computational science, computational modeling has merged as a powerful tool to study complex systems. In the field of energy conversion and storage, modeling has already been applied to various systems including fuel cells,[126,127] photovoltaic cells[128,129] and rechargeable batteries.[130]

Figure 2.20: Schematic representation of the workflow in computational modeling.[125]

As highlighted in this chapter, a LOB is a complex system with multiple components and its operation relies on various physical and chemical processes occurring at different time and length scales. For example, the bond breakage and formation during chemical reactions happens within several pico-seconds (10^{-12} s), while the O_2 transport through the porous electrode occurs within a few seconds (s). Thus, diverse modeling techniques at both microscale and macroscale are applied for the modeling of LOBs.

III.1 Microscopic models

III.1.a Application of Density Functional Theory in Li-O_2 batteries

Density Functional Theory (DFT) is a quantum mechanical modeling method which focuses on the most local level of the bulk and surface/interface properties of the materials at a length scale of nm. Through DFT calculations, one can predict not only the electronic structure of materials, but also the thermodynamic or kinetic parameters, such as equilibrium energies or energy barriers of the system or process.

As shown previously in this Chapter, DFT has been widely applied to calculate the electrical conductivity of Li_2O_2 and various mechanisms were proposed to account for the charge transport across Li_2O_2.[99–101,103,131,132] A polaron hopping mechanism was proposed by calculating the formation energy and the migration energy barrier of the charge carriers in crystalline and in amorphous Li_2O_2. Surface conduction mechanism was suggested by determining the electronic structure of the Li_2O_2 surface and grain boundary. These investigations advance in the understanding of the charge transport mechanism in LOBs.

Also, DFT calculations have been used to predict the reaction and degradation mechanism in LOBs. The topotactic delithiation mechanism of Li_2O_2 decomposition proposed by Kang is based on the energy calculation of Li_xO_2 ($1<x<2$) compounds.[106] This work has provided theoretical evidence for the low-potential oxidation of Li_2O_2. Besides, Bryantsev *et al.* predicted the instability of carbonate-based electrolytes towards the superoxides by calculating the free energy barrier and reaction free energy for nucleophilic substitution and proton/hydrogen abstraction reactions, which has been confirmed later in experiments.[68] The same authors also reported the autoxidation mechanism of ethers and amides, explaining the instability of those solvents in LOBs.[75]

Another application of DFT in LOBs is to provide the molecular-level insights into the thermodynamics of the catalysts. Dathar *et al.* reported a volcano-like trend of the calculated intrinsic activity of Au, Ag, Pt, Pd, Ir, and Ru with respect to the adsorption energy of oxygen, with Pd and Pt being the most active.[133] This trend is based on two different mechanisms, *i.e.*, the associative mechanism involving the reduction of molecular O_2 on Au and Ag, and the dissociative mechanism involving the reduction of atomic O on Pt, Pd, Ir, and Ru. According to the authors, an active catalyst for the ORR reaction should have a O_2 adsorption strength close to Pt and Pd.

However, the DFT method has significant drawbacks. It is strong in predicting the thermodynamics, but it is not suitable for studying the dynamics of the systems. Furthermore, the simulation conditions in DFT deviate from the realistic system regarding: (a) vacuum assumption, (b) 0 K assumption, and (c) absence of electric field.

III.1.b Application of Molecular Dynamics in LOBs

Molecular Dynamics (MD) simulation focuses on interatomic or intermolecular interactions. The system is presented as a collection of spheres at a resolution of atoms or groups of atoms, whose positions and velocities are calculated by using Newton's equations.[134] The forces that act on the atoms or atom groups are determined from the interaction potentials, also known as "force fields", which could be obtained from first-principles calculations or empirical fitting.

In comparison to the DFT method, MD simulations can be applied to larger length and time scales. As MD enables the simulation of the systems dynamics and particle trajectory, it is widely used to simulate the ion transport in solids.[135–137] Besides, due to the flexibility of the determination of force fields, the system could be simulated with more realistic feature via the MD method.

A few MD models of LOBs are reported in the literature, mainly related to the solvent/solute interaction. With MD simulation, Scheers *et al.* investigated the solvation of $LiO_{2(ip)}$ in different electrolyte and found that O_2^- in DME is more prone to reduction due to low permittivity.[53] Sergeev *et al* studied the solvent structuring and salt ion distribution near the electrode surface via MD simulation.[138] The authors found that under realistic potential, the electrode/DMSO interface will push O_2^- anions out of

the reaction layer, suggesting the preference of solution mechanism in DMSO electrolyte as consistent with the experimental observations

However, the time scale of MD is typically around several nano-seconds, which is too short to capture the long-range mass transport in electrolyte. Moreover, there is a lack of possibility to address chemical and electrochemical reactions with MD, except if using ReaxFF techniques which are difficult to parameterize.[139]

III.2 Macroscopic models

Macroscopic models, based on the resolution of partial differential equations, can simulate the LOBs in terms of temporal and spatial dependent quantities, such as the concentrations of species and evolution of cell voltage, which can be directly compared with the experimental observations.

In a continuum model, the battery components are considered as a continuum media consisting of several phases, typically a solid phase presenting the electrode or separator, and a liquid phase representing the electrolyte. Transport of soluble species occurs in the liquid phase and the electrochemical reactions take place at the boundary between the solid and the liquid phases. Most of the continuum models focus on the positive electrode. Depending on the main interests, they can be classified into two categories: structural models and mechanistic models. The structural models emphasize on the positive electrode texture and its variation upon cycling.[140–143] The O_2 transport through the electrode has been described with some details while the reaction kinetics description was simplified. By contrast, mechanistic models provide more details of the reaction mechanisms upon discharge, usually through elementary kinetic approaches.[97,144–146] In some cases, the transport phenomena have been incorporated in the mechanistic models,[142] while there are some mechanistic models which are more focused on the local reaction kinetics without considering the species transport at the cell-scale.[146]

III.2.a Structural models

The first Li-O_2 model was proposed by Sandhu *et al.*[143] Neglecting the electrode passivation, the simulation results of this model show that the discharge capacity was limited by pore clogging close to the air inlet. Similar inhomogeneous formation of Li_2O_2 has been captured in the model reported by Andrei *et al.*[147] Targeting delay in the

pore clogging, the authors further proposed a new approach to enhance only the reaction kinetics at the separator side by non-uniform catalyst distribution along the positive electrode thickness.[147] This concept has been demonstrated in numerical simulations and a larger improvement in discharge capacity is found in non-uniform system as compared to uniform system. However, as aforementioned, the impacts of catalysts on the discharge can be limited, which raised the question of the experiment relevance of this study.

Despite that the structure properties, such as the porosity and pore size, homogenizing to single-value parameters, the correlation between these parameters is built through the geometrical representation of the electrode texture. Rather than using the mean pore size, Franco *et al.* and Xue *et al.* at LRCS have previously developed a continuum model considering, the pore size distribution of the positive electrode.[142,148] In the model, both electrode passivation and pore clogging have been considered to be responsible for the degradation of active surface area. This model has been applied to electrodes based on Super P carbon and Ketjen Black carbon, respectively (**Figure 2.21 a**). The simulation results revealed that larger discharge capacity was found in the Ketjen Black cell because its high specific surface area led to slower Li_2O_2 thickness growth rate (**Figure 2.21 b**).

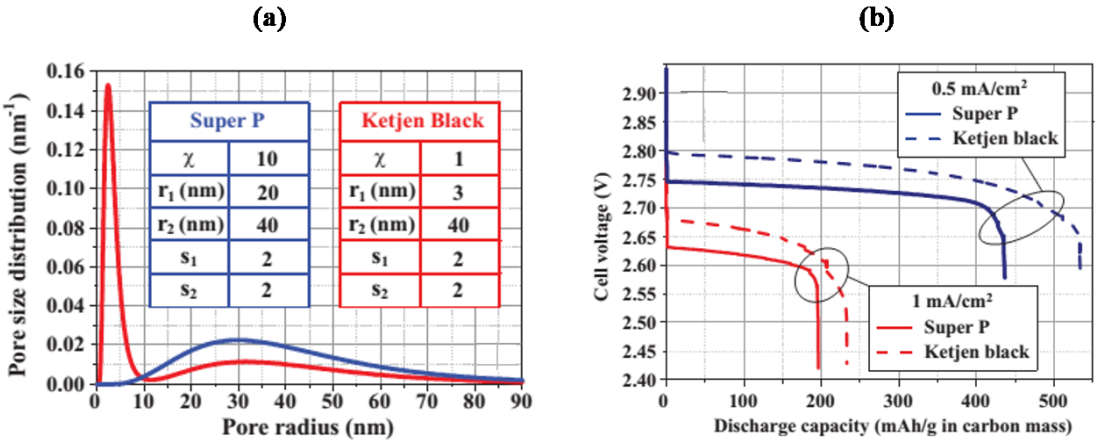

Figure 2.21: (a) Pore size distribution of carbon Super P and Ketjen Black; **(b)** comparisons of simulated discharge profiles for LOBs with Super P and Ketjen Black electrodes. [117]

Bevara *et al.* analyzed different material microstructures including structures made of spherical and cylindrical pores, nanoparticles, carbon nanotubes, and nanofibers (**Figure 2.22**).[149] It shows that although the different microstructures result in different dynamics in which the pores are being filled, they lead to relatively similar values of the energy and power densities.

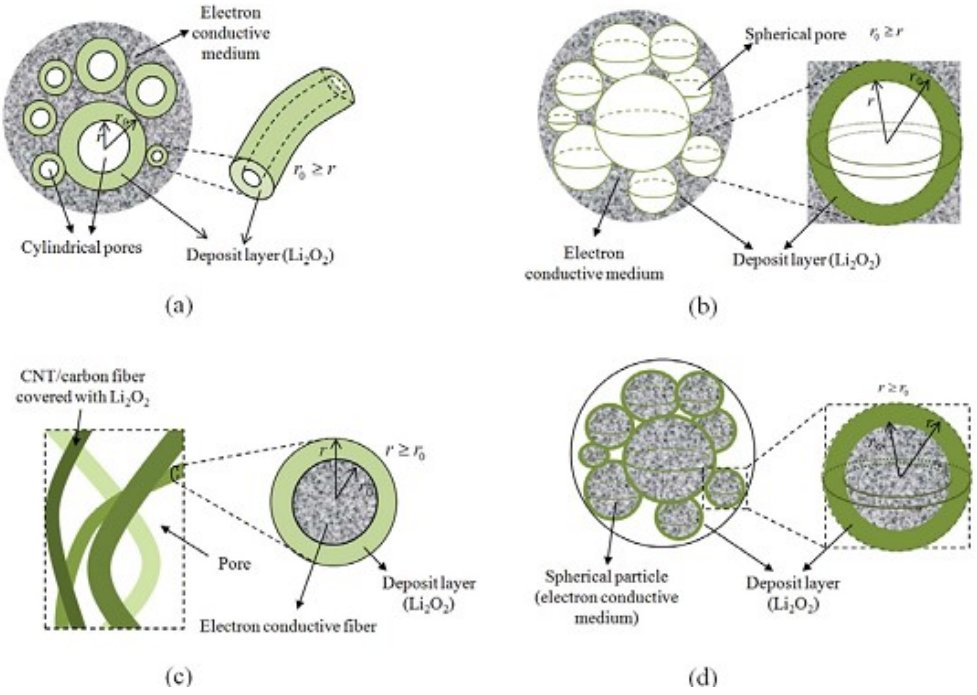

Figure 2.22: Deposition of the discharge product for the four structures: (a) cylindrical pores, (b) spherical pores, (c) carbon nanotube and carbon nanofibers, and (d) spherical nanoparticles. The initial radius is denoted by r_0, while the instantaneous radius is r.[149]

Due to the formation of Li_2O_2 as well as Li consumption, the volume of solid phase in positive electrode varies during discharge. This volume change was studied by Yoo *et al.* [140] In their model, it is assumed that the gap between the Li anode and the separator increases during discharge due to the decrease of total volume of the solid phase. Therefore, the electrolyte level in the cell will decrease, resulting in electrolyte depletion in some part of the positive electrode. The simulation results indicate that this volume change will cause the capacity loss and potential drop. Huang *et al*. also investigated the volume change during discharge and in addition, the evaporation of volatile solvent has been also considered in their model.[150] However, their model

suggested that the decrease of electrolyte level can increase the discharge capacity because of a more uniform Li_2O_2 distribution and better pore utilization. As the position with the highest Li_2O_2 deposition rate shifts with the electrolyte level, Li_2O_2 is said to form more uniformly, leading to a higher capacity as compared to electrode with constant electrolyte level.

III.2.b Mechanistic models

In contrast to the structural models with oversimplified reaction mechanisms, mechanistic models provide more insights into reaction details such as the competition between different mechanisms, the nucleation and growth of Li_2O_2 and impacts of redox mediators.

Safari *et al.* proposed a kinetic model depicting the oxygen reduction in non-aqueous LOBs, where the key steps included O_2 reduction, LiO_2 reduction and LiO_2 desorption.[146] The competition between the solution mechanism and surface mechanism was represented by the competition between the reduction and desorption of LiO_2, which are characterized by the electrode potential (discharge current density) and Li_2O_2 desorption time constant. However, the model is unrealistic as it considers only a monolayer formation of Li_2O_2, which is much thinner than the critical tunneling distance. Moreover, as a kinetic model, it is not able to capture the impacts of electrode texture.

At the same time, a comprehensive model was proposed by Xue *et al.* at LRCS, which was able to capture the competition between the solution mechanism and surface mechanism in a more realistic way.[97] In this model, it is assumed that the large Li_2O_2 particles were only formed in the large pores, noted as "Hall" (**Figure 2.23 a**). The soluble LiO_2 formed in the smaller pore either convert to Li_2O_2 locally via surface mechanism or escape to the Hall so as to form Li_2O_2 via solution mechanism. A hierarchical pore network has been used to describe the pore structure of the positive electrode (**Figure 2.23 b**) and the escape probability was described with an escaping factor ξ. In high DN solvent, such as DMSO, the higher $LiO_{2(ip)}$ solubility resulted in a larger ξ and lead to a higher discharge capacity as compared to that in low DN solvent, which agreed well with the experimental results (**Figure 2.23 c**). Nevertheless, the versatility of this model has been reduced due to the simplification of the discharge mechanism.

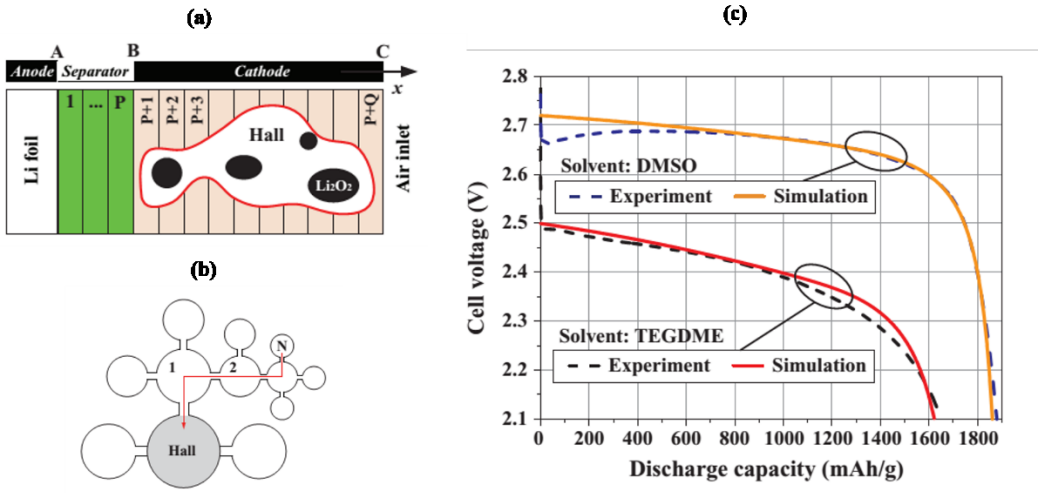

Figure 2.23: (a) Schematic illustration of the LOB model with the implemented finite difference bins, where it was assumed that the large Li_2O_2 particles were formed only in large pores, noted as "Hall". **(b)** Hierarchical pore network model of the pore structure; **(c)** Simulated discharge curves in DMSO and TEGDME in comparison with experimental results. [97]

In order to achieve a more detailed description of the electrochemical reactions in LOBs, Hostmann *et al.* used nucleation theory but in an aqueous environement.[151] Recently, Lau *et al*. reported a nucleation model to simulate the nucleation and growth of Li_2O_2 in non-aqueous LOBs.[152]. By combining atomistic nucleation theory and Kolmogorov's phase transformation theory, the model has provided a good description of the discharge profile obtained from experiments at low current density. But in this model, the discharge mechanism was simplified and mass transport was not considered. As a result, the spatial distribution of the Li_2O_2 deposit cannot be captured by this model.

Furthermore, Welland *et al.* proposed an atomistically informed mesoscale model for the deposition of discharge product in a LOB.[153] This model includes particle growth and coarsening as well as a simplified nucleation model. Instead of Li_2O_2, the nucleation, growth and coarsening were considered with LiO_2. The simulation results suggested that particle coarsening, in which large particle grow and small particles disappear, had a substantial effect on the particle size distribution during the discharge process. However, the assumption of LiO_2 nucleation and growth is contradictory to the experimental observation, where Li_2O_2 are determined as the main discharge product.

Most of the present continuum models focus on the discharge process, while only few papers have included the charge process.[154,155] Recently, by coupling a kinetic model with multistep reaction mechanism to a 1D porous-electrode transport model, Grübl *et al.* studied the cycling of LOBs and analyzed the impacts of redox mediator.[145] The simulation results confirmed that the use of redox mediator could help decrease the charge voltage by transferring the electron from carbon surface to Li_2O_2. While the model reproduced the discharge profiles well, the simulated charge profile showed deviation from experimental observation, which was ascribed to partially irreversible discharge step. Moreover, Li_2O_2 was assumed as a film with a constant thickness, which is not consistent with the experimental observations.

IV. Conclusions

Non-aqueous LOBs are highly complex systems, where many factors interoperate to determine the cell performance.

The discharge capacity is limited by both electrode passivation and pore clogging which depends strongly on the Li_2O_2 morphology. Small Li_2O_2 particles or thin-film leads to fast electrode passivation, while large Li_2O_2 particles can block the pores of the electrode. The morphology of Li_2O_2 is determined by the effects of electrolyte components, electrode nature and discharge current density. The electrode texture, which is mainly characterized by the specific surface area, pore size and pore volume, also shows impacts on the discharge capacity. Electrodes with large specific surface area, large pore size and large pore volume are favored. Large specific surface area can provide more active site for the electrochemical reactions, a pore of large size is less likely to be clogged, and large pore volume can accommodate more Li_2O_2. However, it is difficult to maximize all these texture properties at the same time due to interplays among them, which makes the optimization of electrode to be a challenging issue.

The charge of LOBs suffers from the high overpotential and high electrode potential, which is correlated to the insulating nature of Li_2O_2. The shapes of the charge profiles present a large variance in different electrolyte and with different electrode materials, indicating that the charge mechanism can be complex. Various mechanisms of charge have been proposed, but there is still no consensus.

Though the computational modeling of LOBs is still in the early development stages, there has been an increasing number of works reported in recent years. Both microscopic and macroscopic modeling methods have been applied. The microscopic models provide molecular-level insights to various aspects including the charge transport across Li_2O_2, stability of electrolyte and catalytic impacts. The macroscopic models simulate the LOBs at cell-level, with their emphasis on either electrode texture or reaction kinetics. However, comprehensive models are still needed to predict macroscopic features (*e.g.* discharge/charge profile) from the chemical and textural properties of the cell components. Moreover, mesoscopic models are also needed to bridge the microscopic and macroscopic scales with the hope to provide more insights into the unsolved puzzles of Li-O_2 system, such as the role of catalysts and the origin of the potential rising during charge process.

Chapter 3 : Charge Model of Li-O_2 Batteries

Comparing to discharge processes, the modeling of the charge process is more challenging due to the unclear charge mechanism. Though different theories have been proposed based on experimental observations[110,156,157] or DFT calculations,[106] there is a lack of cell models to simulate the charge process of LOBs. To fill the blank, in this chapter, we propose a continuum model combining the mathematical descriptions of elementary reaction kinetics and mass transport to simulate the charge process of Li-O_2 cells. In complementary addition, alternative kinetic models have been built to further investigate dependence of the charge process on Li_2O_2 particle size. Part of the content of this Chapter is based on the paper: Y. Yin, C. Gaya, A. Torayev, V. Thangavel, and A. A. Franco, *J. Phys. Chem. Lett.*, **7**, 3897–3902 (2016).

I. Model description

I.1 Charge mechanisms and reaction kinetics

The initial condition of the charge process strongly depends on the discharge history, which determines the morphology and spatial distribution of the primary discharge product Li_2O_2. The surface mechanism gives a layer of Li_2O_2 thin film or small particles with a thickness of 5−10 nm[35,99] while the solution-phase mechanism forms large particles up to hundreds of nanometers in size and these particles usually have a toroidal morphology.[36] Though either of these two mechanisms can be dominant depending on the discharge conditions, surface mechanism is expected to happen all the time. This is because LiO_2 is formed close to the electrode surface and generally has a limited solubility. In this context, the Li_2O_2 thin film or small particles can coexist with large Li_2O_2 particles. This coexistence is supported by the experimental observation: though the large Li_2O_2 particles in discharged electrodes did not cover all the surface of the electrode, the electrode was found to be completely passivated, possibly due to the Li_2O_2 thin film which is too thin to be observed in SEM.[35,107]

In this model, a bi-modal particle size distribution (PSD) of Li_2O_2 is considered as the initial condition. As shown in **Figure 3.1**, Li_2O_2 is represented as hemispherical particles with different sizes deposited on the electrode surface. On one hand, Li_2O_2 formed through the surface mechanism is represented by small hemispheres, marked as $Li_2O_{2(f)}$. The radius of small particles is around 7 nm, which is close to the reported

critical electronic tunneling distance.[99] On the other hand, Li_2O_2 formed through the solution mechanism are assumed to be large hemispheres, noted as $Li_2O_{2(p)}$.

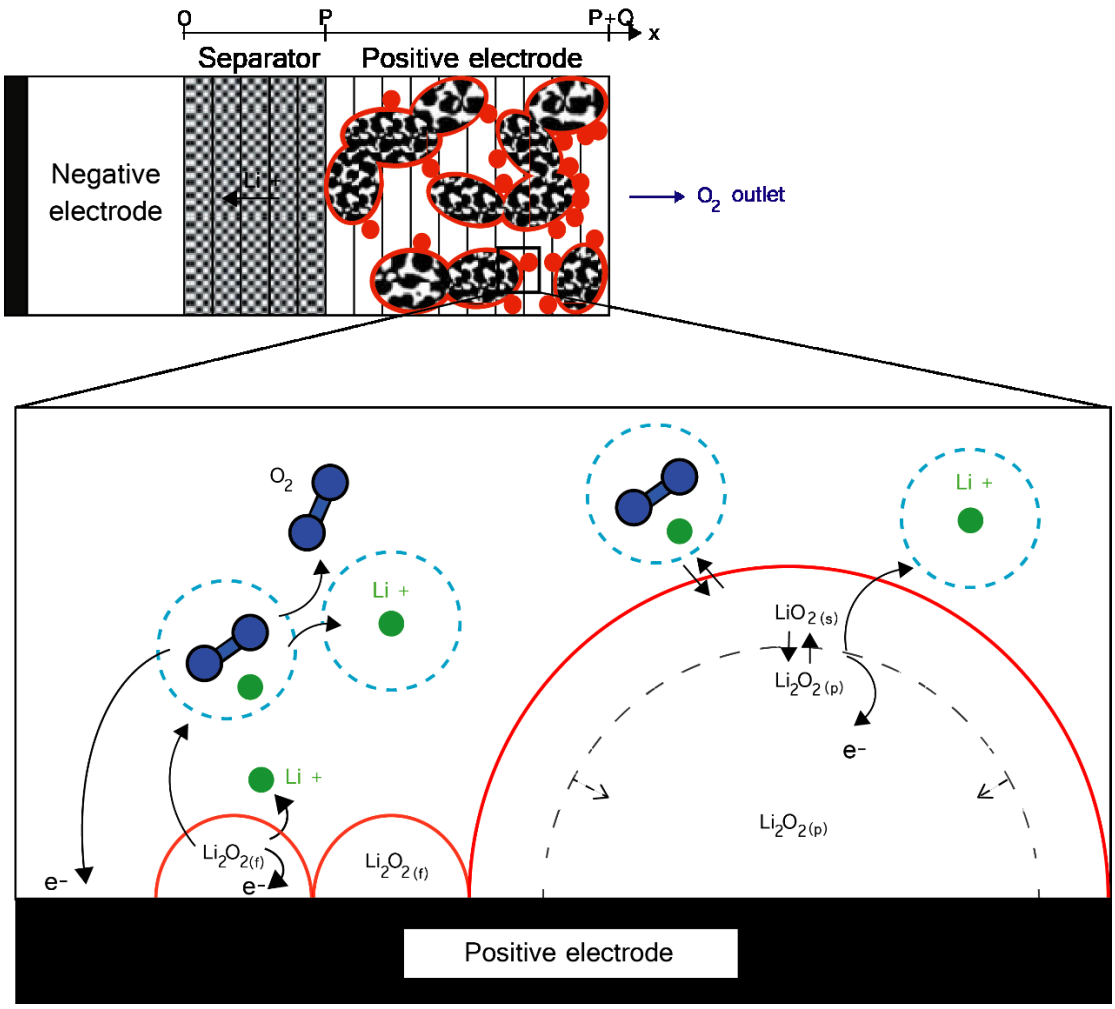

Figure 3.1: Schematic illustration of the cell configuration and charge mechanisms considered in this model. The large particles represent Li_2O_2 formed via the solution mechanism and small particles represent Li_2O_2 formed from the solution mechanism.

During the charge process, different decomposition mechanisms have been assigned to Li_2O_2 particles depending on their sizes. For $Li_2O_{2(p)}$, the oxidation starts with the de-intercalation of Li^+ from its particle surface, forming LiO_2-like species, marked as $LiO_{2(s)}$:

$$Li_2O_{2(p)} \rightarrow LiO_{2(s)} + Li^+ + e^- \qquad 3.1$$

As suggested by Kang *et al*,[106] the above step needs an activation energy around 0.4-0.5 V. $LiO_{2(s)}$ is then dissolved into the electrolyte in the form of ion pair, noted as $LiO_{2(ip)}$:

$$LiO_{2(s)} \leftrightarrows LiO_{2(ip)} \tag{3.2}$$

which is further oxidized on the electrode surface to produce Li^+ and O_2:

$$LiO_{2(ip)} \rightarrow Li^+ + O_2 + e^- \tag{3.3}$$

By contrast, the $Li_2O_{2(f)}$ is considered to decompose directly to $LiO_{2(ip)}$:

$$Li_2O_{2(p)} \rightarrow LiO_{2(ip)} + Li^+ + e^- \tag{3.4}$$

Because of the very fast decomposition of $LiO_{2(ip)}$, the oxidation of $Li_2O_{2(f)}$ can be regarded as a one-step reaction involving two electrons. At the same time when Li_2O_2 is oxidized at the positive electrode, Li deposition takes place at the negative electrode:

$$Li^+ + e^- \rightarrow Li \tag{3.5}$$

The reaction kinetics of the electrochemical reaction j is characterized by the local Faradaic current density i:

$$i_j = nF\left\{k_{f,j}\prod_i a_i^{s_{i,j'}}\exp\left(\frac{(1-\alpha)nF(\Psi-\phi)}{\mathrm{RT}}\right) - k_{b,j}\prod_i a_{i,j}^{s_{i,j}}\exp\left(\frac{-\alpha nF(\Psi-\phi)}{\mathrm{RT}}\right)\right\} \tag{3.6}$$

where n is the number of electrons transferred in the reaction, F is the faraday's constant, $k_{f,j}$ and $k_{b,j}$ are the heterogeneous rate constants, a_i is the activity of species i which has a stoichiometric coefficient of $s_{i,j}$, α is the charge transfer coefficient, Ψ is the electrostatic potential in the electron-conductive phase (electrode) and ϕ is the electrostatic potential in the electrolyte phase. The activity here is defined as the ratio between the concentration c_i and the corresponding standard concentration c_i^0:

$$a_{i,sol} = \frac{c_i}{c_i^0} \tag{3.7}$$

The standard concentration of Li^+ equals 1 M but that of O_2 and $LiO_{2(ip)}$ equal their saturation concentration in electrolyte.

It is worth noting that while Ψ is identical for the entire electrode and for all electrochemical reactions, ϕ varies along the thickness of positive electrode depending on the local activities of the reactants. The value of ϕ is calculated from the Nernst relationship:[158]

$$\Phi = E^0 + \frac{RT}{nF}\ln\frac{a_{Li^+}^2 a_{O_2}}{a_{Li_2O_2}} \quad 3.8$$

where E^o represents the standard potential of the reaction.

The cell voltage is calculated as the potential difference between the positive electrode and the negative electrode:

$$U_{cell} = \Psi_{pos} - \Psi_{neg} \quad 3.9$$

Under galvanostatic conditions, integrating the current density over the corresponding active surface in the volume of the electrode equals the total applied current (I_{input}):

$$I_{input} = \int \sum_j \frac{A_j}{V} i_j dV \quad 3.10$$

where A_j is the active surface area of the electrochemical reaction j, i_j is the Faradaic current density (A/m^2) of the electrochemical reaction j with respect to the active surface, and V is the electrode volume.

The value of A_j depends on the reaction. For the oxidation of immobile Li_2O_2 particles, either in the form of large or thin-film particles, the active surface refers to the surface area of the particle, as the reactions happen at the particle/electrolyte interface which can be written as:

$$A_p = 2\pi r_p^2 N_p V \quad 3.11$$

$$A_f = 2\pi r_f^2 N_f V \quad 3.12$$

where r_p and r_f are the radius of large and small particles, respectively. N_p and N_f are the particle densities (number per unit of electrode volume). For the oxidation of $LiO_{2(ip)}$, which takes place mainly on the uncovered part of the electrode (*e.g.* carbon) the corresponding active surface area ($A_{LiO_2(ip)}$) is then calculated as:

$$A_{LiO_{2(ip)}} = A_C - \pi r_f^2 N_f V - \pi r_p^2 N_p V \qquad 3.13$$

with A_C being the electrode (carbon) surface area.

Apart from the electrochemical reactions, the net rate of the $LiO_{2(s)}$ dissolution can be obtained by summing up the rates of the $LiO_{2(s)}$ dissolution and $LiO_{2(ip)}$ deposition as follows:

$$v = k_f A_p \theta - k_b a_{LiO_{2(ip)}} \qquad 3.14$$

where θ stands for the surface coverage of $LiO_{2(s)}$ on the Li_2O_2 large particle surface.

When the $LiO_{2(s)}$ film is a monolayer, its surface coverage over the large Li_2O_2 particles is determined by the ratio between the surface area of adsorbed $LiO_{2(s)}$ and the surface area of the large Li_2O_2 particles (**Figure 3.2**). The surface coverage is assumed to be 1 if $LiO_{2(s)}$ consists of multiple layers. The mathematical criterion for the surface coverage by $LiO_{2(s)}$ on the large Li_2O_2 particles is written as:

$$\theta = \begin{cases} \dfrac{V_{LiO_2(s)}}{\delta \times N_p V 2\pi {r_p}^2} & , \quad \dfrac{V_{LiO_2(s)}}{\delta} < N_p V 2\pi {r_p}^2 \\ 1 & , \quad \dfrac{V_{LiO_2(s)}}{\delta} \geq N_p V 2\pi {r_p}^2 \end{cases} \qquad 3.15$$

where $V_{LiO_2(s)}$ is the volume of the $LiO_{2(s)}$.

Besides, the dissolution kinetics of $LiO_{2(s)}$, which are formed on the surface of the large Li_2O_2 particles, depends on their particle size according to:[159]

$$k_f = k^{\infty} exp\left(\frac{2\boldsymbol{\sigma_{LiO_{2(s)}}}\boldsymbol{\omega_{LiO_{2(s)}}}}{RTr_p}\right) \qquad 3.16$$

where k^{∞} is a prefactor, $\sigma_{LiO_{2(s)}}$ is the $LiO_{2(s)}$ surface tension and $\omega_{LiO_{2(s)}}$ is the molar volume of $LiO_{2(s)}$.

Figure 3.2: Schematics of the $LiO_{2(s)}$ formed on the surface of a large Li_2O_2 particle: To the left, a case is represented where the $LiO_{2(s)}$ monolayer covers less than the large Li_2O_2 particle surface ($\theta < 1$), and to the right, a case is represented where $LiO_{2(s)}$ completely covers the large Li_2O_2 particle surface and forms a multilayer ($\theta = 1$).

I.2 Mass Transport

The mass transport of Li^+, O_2 and $LiO_{2(ip)}$ are solved in the domains of positive electrode and separator. Diffusion is considered as the main driven force for the mass transport, which could be solved according to the porous electrode theory based on the combination of first and second Fick's laws,[160]

$$\frac{\partial(\varepsilon c_i)}{\partial t} = -\frac{\partial J_i}{\partial x} + S_i = \frac{\partial}{\partial x}\left(\varepsilon^{\beta} D_{0,i} \frac{\partial c_i}{\partial x}\right) + S_i \qquad 3.17$$

where ε is the porosity of the positive electrode or separator, β is the Bruggeman coefficient equaling to 0.5, $D_{0,i}$ is the bulk diffusion coefficient of species i and S_i is a source term resulting from the reactions.

The source term S_i, which refers to the overall formation/consumption rate of species i, is solved by summing up formation or consumption rates of species i in all the involved reactions as follows:

$$S_i = \frac{\sum_j s_{i,j} A_j v_j}{V} \qquad 3.18$$

Similarly, the rate of volume change of the large Li_2O_2 particles can be obtained by:

$$\frac{\partial V_p}{\partial t} = \sum_j s_{i,j} A_j v_j \, \omega_{Li_2O_2} \qquad 3.19$$

Assuming the shape of particle is self-similar, the relationship between the radius and total volume of particles is given by:

$$r_p(t) = \left(\frac{3}{2\pi N_p V} V_p(t)\right)^{\frac{1}{3}} \qquad 3.20$$

The volume and size of $Li_2O_{2(f)}$ can be calculated through a anologous approach.

The flowchart of the model is presented in **Figure 3.3**. During each iteration in the simulation, the electrode potential is firstly solved with concentrations and activities of species from the previous time-step. Afterwards, the rates of all the reactions are solved accordingly, followed by the calculation of the source term S_i, the porosity, the passivation and the PSD. Then, the iteration ends up by updating the concentrations by solving the mass transport together with the S_i.

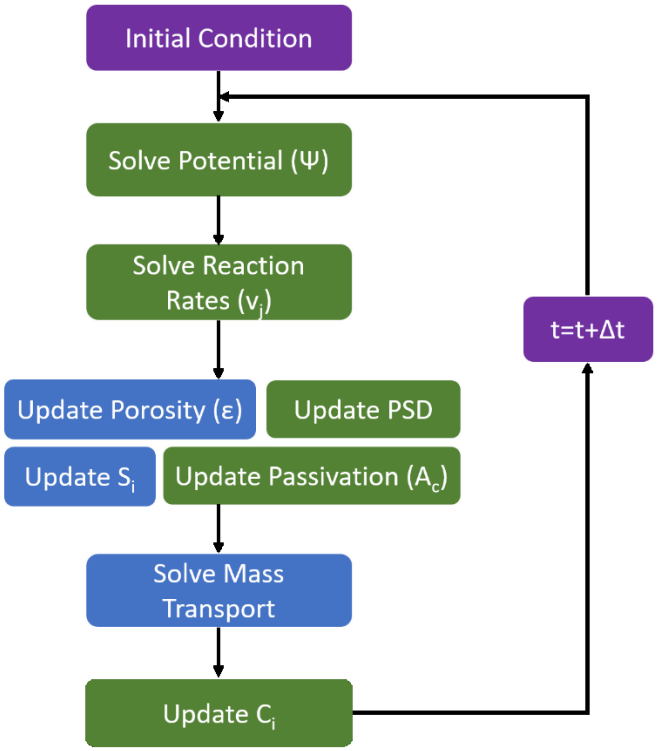

Figure 3.3: Flowchart of the model, where the blue parts have direct impacts on the mass transport and the green parts are related to the reaction kinetics.

The cell parameters in the simulation are adapted from the experiments reported by Zhai *et al*,[107] where high surface area active carbon (AC) is used as cathode materials. The loading of the carbon materials is 1.6 mg/cm^2, and the geometric surface area of the cathode is considered to be 1 cm^2. Same as in the experimental reference, prior to the charging process, the electrode was firstly discharged to 1000 mAh/g_{AC}. The baseline value for the charging current density is 0.1 mA/cm^2 with respect to the geometrical surface area of the cathode. The particle densities of $Li_2O_{2(f)}$ and $Li_2O_{2(p)}$ are not given in the experimental references. As an assumption, it is considered that the total volume of each form of Li_2O_2 are equal and each of them accounts for half of the total capacity. Parameters used in the simulation are summarized in

Table 3.1.

Table 3.1: Values of parameters used in the cell model for charge process.

Parameters	Values	Units	Sources
Physical constants			
Gas constant	8.31	$J.K^{-1}.mol^{-1}$	/
Faraday constant	96485	$C.mol^{-1}$	/
Boltzmann constant	1.38×10^{-23}	$m^2.kg.s^{-2}.K^{-1}$	/
Cell parameters			
Cathode thickness	4.86×10^{-5}	m	Ref[107]
Electrode specific surface area	7.68×10^{9}	$m^2.m^{-3}$	Ref[107]
Bruggeman coefficient	1.5	/	
Pristine cathode porosity	0.791	/	Ref[107]
Separator porosity	0.5	/	Assumed
Li^+ initial concentration	1×10^{3}	$mol\ m^{-3}$	Ref[107]
O_2 initial concentration	4.43	$mol\ m^{-3}$	Ref[161]
$LiO_{2(ip)}$ initial concentration	1	$mol\ m^{-3}$	Assumed
$LiO_{2(s)}$, Li_2O_2 molar volume	1.98×10^{-5}	$m^3\ mol^{-1}$	Ref [106]
$LiO_{2(s)}$ monolayer thickness	3×10^{-10}	m	Assumed
Li^+ diffusion coefficient	1×10^{-9}	$m^2\ s^{-1}$	Ref[161]
O_2 diffusion coefficient	1.67×10^{-9}	$m^2\ s^{-1}$	Ref[161]
$LiO_{2(ip)}$ diffusion coefficient	1.3×10^{-9}	$m^2\ s^{-1}$	Assumed
Electrochemical parameters			
Applied charge current	1	$A\ m^{-2}_{geometric}$	Ref[107]
Standard potential of LiO_2/Li_2O_2	3.1	V v.s. Li^+/Li	Ref[161]
Standard potential of LiO_2/O_2	2.96	V v.s. Li^+/Li	Ref [35]
Charge transfer coefficients	0.5	/	Assumed
Surface tension ($\sigma_{LiO_{2(s)}}$)	10	$J.m^{-2}$	Assumed
Kinetic parameters			
rate constant of $Li_2O_{2(p)}$ oxidation	1×10^{-11}	$mol.s^{-1}.m^{-2}$	Fitted
rate constant of $Li_2O_{2(f)}$ oxidation	1×10^{-10}	$mol.s^{-1}.m^{-2}$	Fitted
rate constant of $LiO_{2(ip)}$ oxidation	1×10^{-8}	$mol.s^{-1}.m^{-2}$	Fitted

II. Results Analysis and Discussion

The simulated charge profile of the Li-O_2 cell consists of two voltage plateaus at 3.6 V and 4.1 V, respectively (**Figure 2.4 a**). This stepwise profile is in agreement with the successive decomposition of the $Li_2O_{2(f)}$ and $Li_2O_{2(p)}$. As shown in **Figure 2.4 b**, the radius of $Li_2O_{2(f)}$ is shrinking at the initial stage of the charge process and it continues until its complete removal. After that, the decomposition of Li_2O_2 starts. Therefore, the oxidation of $Li_2O_{2(f)}$ accounts for low voltage plateau, while the oxidation of $Li_2O_{2(p)}$ is related to the high voltage plateau. This is also consistent with the evolution of faradaic current due to the oxidation of $Li_2O_{2(f)}$, $Li_2O_{2(p)}$ and $LiO_{2(ip)}$ along the charge process (**Figure 2.4 c**). It is found that the oxidation current of $LiO_{2(ip)}$ always accounts for half of the total applied current, with the other half coming successively from $Li_2O_{2(f)}$ oxidation and $Li_2O_{2(s)}$ decomposition. Consequently, the electron/O_2 ratio is always $2e^-/O_2$ during the charge process, which accords with the DEMS results as reported by McCloskey.[86] Besides, the steady oxidation current of $LiO_{2(ip)}$ indicates that the $LiO_{2(ip)}$ is decomposed soon after its formation as in agreement with short lifetime of $LiO_{2(ip)}$ due to its fast reaction kinetics. Though the $LiO_{2(ip)}$ concentration is generally low along the charge process, a relative higher value is found at the low voltage plateau (**Figure 2.4 d**), which can be explained by the direct formation of $LiO_{2(ip)}$ via $Li_2O_{2(f)}$ oxidation.

The stepwise charge profile as well as successive decomposition of $Li_2O_{2(f)}$ and $Li_2O_{2(p)}$ is in good agreement with the experimental results reported by Zhai *et al*.[107] As shown in **Figure 3.5**, the experimental charge profile also presents two voltage plateaus, which are located at 3.4 and 4.1 V, respectively. By tracking the morphology change of large Li_2O_2 toroids, it is found that those large particles did not shrink until the charge potential rising above 4 V. This indicates that the high voltage plateau corresponds to the decomposition of large Li_2O_2 particles as same as that in the simulation results. Moreover, the unchanged size of Li_2O_2 particles also implies that other electrochemical process occurred at the low voltage plateau, which may be the oxidation of LiO_2 formed during discharge as suggested by the authors,[107] but also can be the oxidation of $Li_2O_{2(f)}$ that is too small to be observed by SEM as proposed by our model.

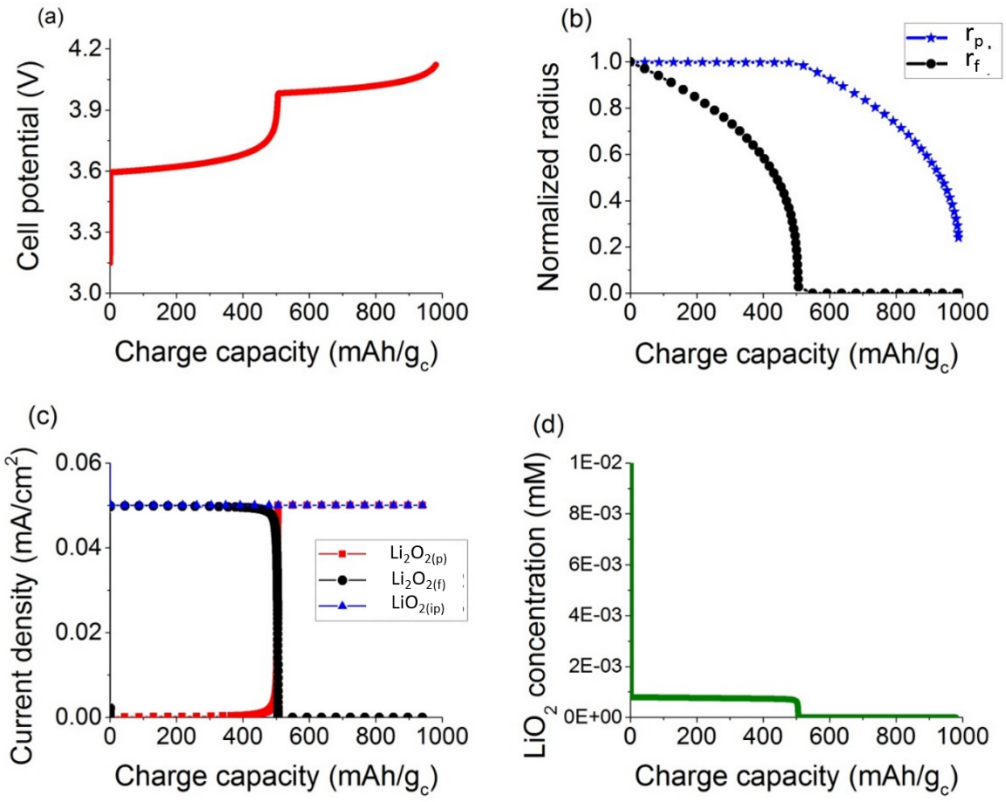

Figure 3.4: Simulated results of **(a)** potential evolution as a function of charge capacity. **(b)** Size evolution of large particles ($Li_2O_{2(p)}$) and small particles ($Li_2O_{2(f)}$) during the charge processes; the displayed sizes are normalized to the initial radius (75 and 7 nm for $Li_2O_{2(p)}$ and $Li_2O_{2(f)}$,respectively). **(c)** Evolution of Faradaic current densities due to the oxidation of $Li_2O_{2(p)}$ (red), $Li_2O_{2(f)}$(black), and $LiO_{2(ip)}$(blue) as a function of the charge capacity. **(d)** Concentration of $LiO_{2(ip)}$ as a function of the charge capacity. All cell parameters are adapted from Zhai *et al.*,[5] and the assumed charge current in the simulation is equal to 0.1 mA/cm^2.

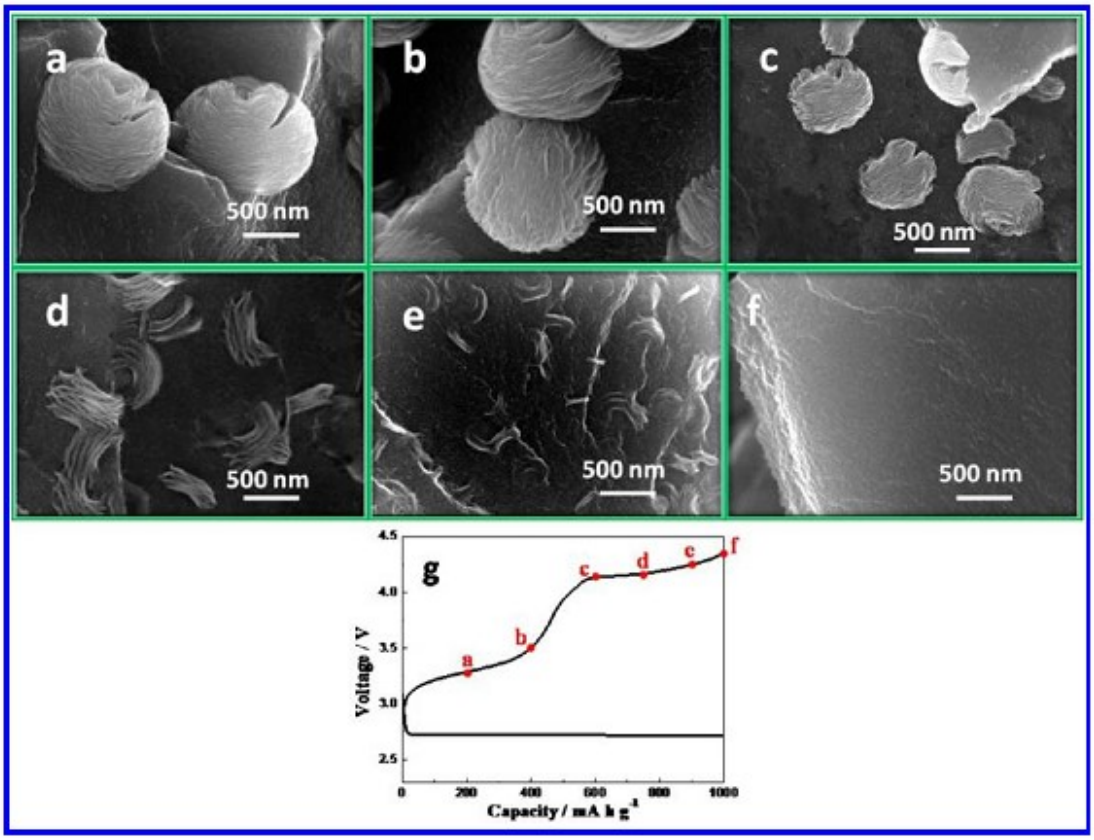

Figure 3.5: (a)-(f) The SEM images of the discharged electrode at different depth correpondting to different points in the charge profile in **(g)**.[107]

The voltage difference between the two plateaus results mainly from the assumed size-dependent charge mechanism. Because the de-lithiation of $Li_2O_{2(p)}$ (**Eq. 3.1**) requires an activation energy of 0.4 V,[106] which is not necessary for $Li_2O_{2(f)}$, $Li_2O_{2(p)}$ are decomposed at higher voltage than $Li_2O_{2(f)}$. In the cell model, it is assumed that as long as the radius of the large particles is larger than 7 nm, the activation energy remains unchanged. However, as the resistivity of Li_2O_2 is high, it is expected that the charge transport through Li_2O_2 particles can result in an ohmic drop and influence the charge voltage, which depends also on the size of Li_2O_2. Thus, to further investigate the dependence of the charge voltage on the Li_2O_2 particle size, we built in the next section a series of kinetic models which focus on the charge transport and reaction kinetics, by neglecting the mass transport in the cell.

III. Kinetic models for charge process

III.1 Potential rising during the charge process

As aforementioned, the charge voltage is influenced by the charge transport through L_2O_2 and reaction kinetics, both of which depend on the Li_2O_2 particles size. For simplicity reasons, the reaction kinetics is described with respect to the overall charge reaction:

$$Li_2O_2 \rightarrow 2Li^+ + O_2 + 2e^- \qquad 3.21$$

but the one electron process of LiO_2 formation is considered as the rate-limiting step. The current density i drawn from a Li_2O_2 particle can be calculated from the Bulter-Volmer relationship:[158,162]

$$i = i_0[\exp(\frac{\alpha n_e F}{\mathrm{RT}}\eta) - \exp(\frac{-(1-\alpha)n_e F}{\mathrm{RT}}\eta)] \qquad 3.22$$

where i_0 is the exchange current and n_e is the number of electrons transferred in the rate-limiting step. The exchange current density i_0 is defined as

$$i_0 = nFk_0 a_{Li}^{2a} a_{O_2}^{1-a} \qquad 3.23$$

Given the activities of Li^+ and O_2 are equal to 1, and their variation during the charging are negligible (which is reasonable when the Li^+ concentration is high and the cathode is thin) **Eq. 3.22** becomes

$$i = nFk_0[exp(\frac{\alpha n_e F}{\mathrm{RT}}\eta) - \exp(\frac{-(1-\alpha)n_e F}{\mathrm{RT}}\eta)] \qquad 3.24$$

Assuming Li_2O_2 as a resistor with a resistivity ρ, the resistance of the Li_2O_2 deposit is proportional to its thickness δ, which is approximated to be the radius r of the Li_2O_2 deposit in the model. Thus, the charging overpotential η can be calculated as follows:

$$\eta = \Psi - \Phi - i\rho r \qquad 3.25$$

By introducing the hyperbolic function and assuming α equal to 0.5, **Eq. 3.24** is further simplified to

$$i_I = 2nFk_0 sinh[\frac{\alpha n_e F}{RT}(\Psi - \Phi - i_I \rho r)] \quad 3.26$$

As *i* appears at both sides, there is not analytical solution for the above equation. However, it can be solved numerically with the Newton-Raphson method. The parameters used in the kinetic models are summarized in

Table 3.1.

The evolution of the current density as function of the L_2O_2 radius is plotted in **Figure 3.6 a** (Mechanism I), where the electrode potential and the Li_2O_2 resistivity is set at 4.0 V and 10^8 Ω·m. For comparison, simulation results by considering only the **charge transport limitation** (Mechanism II) or **reaction kinetics limitation** (Mechanism III) are also shown in the **Figure 3.6 b-c**. In the former case, the relationship between the *i* and electrode potential could be calculated by using Ohm's law

$$i_{II} = -\frac{\Psi - \Phi}{\rho r} \qquad 3.27$$

while in the latter case, similar equation as **Eq. 3.26** with neglecting the *iρr* term as follows:

$$i_{III} = 2nFk_0 sinh[\frac{\alpha n_e F}{\mathrm{RT}}(\Psi - \Phi)] \qquad 3.28$$

The simulated *i-r* curve from Mechanism I has a similar shape as the curve from Mechanism II, though the current density in the former case is generally lower than in the latter case by an order of magnitude. In these two cases, the current density obtained from the Li_2O_2 particles increases with the reduction of the particle size, mainly due to a lower resistance for the charge transfer. Thus, two conclusions can be drawn:

(1) with the same electrode potential, smaller Li_2O_2 particles are decomposed faster;

(2) the current density from the same Li_2O_2 particle increases along the charging process due to the decrease of resistivity.

However, when only the reaction kinetics exerts its effects as in **Mechanism III**, the current density maintains constant for Li_2O_2 with all sizes.

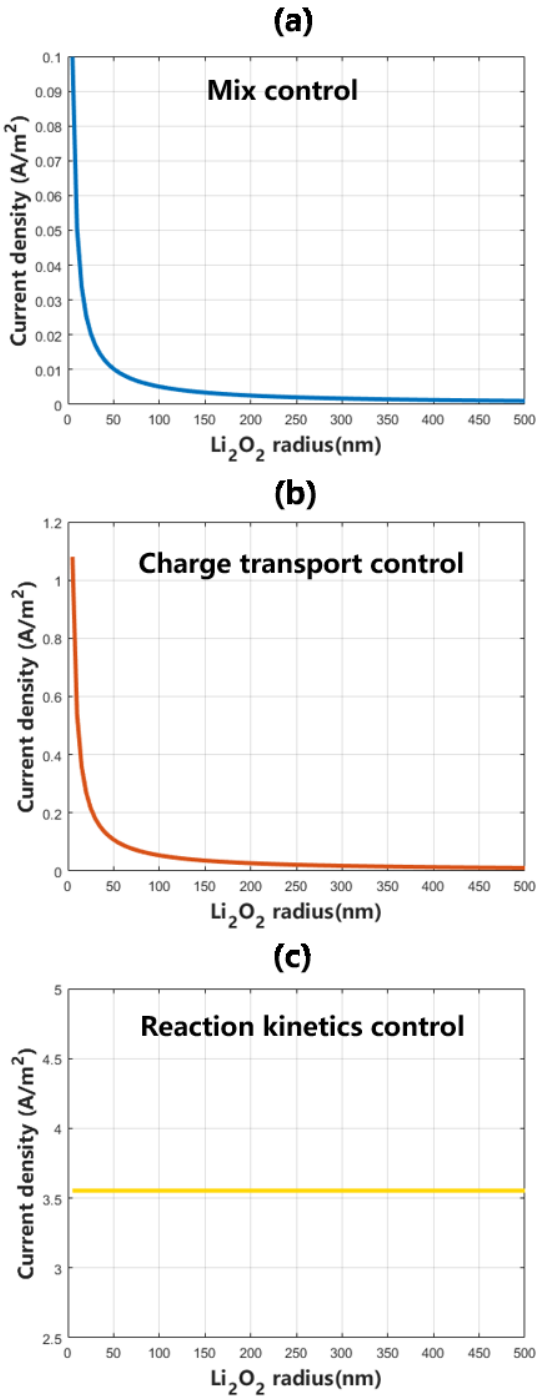

Figure 3.6: The evolution of local current density as a function of particle radius by assuming the rate of Li_2O_2 decomposition is controlled by (a) both charge transport and reaction kinetics; (b) only charge transport and (c) only reaction kinetics. The electrode voltage is set at 3.5 V in the simulations with Li_2O_2 resistivity of 10^8 Ω·m.

Under galvanostatic conditions, the total applied current is linked with the local current by:

$$i = \frac{I_{input}}{N\pi r^2} \tag{3.29}$$

where N is the population of the particles. Therefore, the relationship between the electrode potential and the Li_2O_2 particle size under a current I can be obtained as follows:

Mechanism I (Mix control):

$$\Psi_I = \frac{RT}{an_eF}\, arsinh\left(\frac{I_{input}}{2k_0nFN\pi r^2}\right) + \Phi + \frac{I_{input}\rho}{N\pi r} \tag{3.30}$$

Mechanism II (Charge transport control):

$$\Psi_{II} = \Phi + \frac{I_{input}\rho}{N\pi r} \tag{3.31}$$

Mechanism III (Reaction kinetics control):

$$\Psi_{III} = \frac{RT}{an_eF}\, arsinh\left(\frac{I_{input}}{2k_0nFN\pi r^2}\right) + \Phi \tag{3.32}$$

The corresponding Ψ-r profiles are provided in **Figure 3.7**, by assuming N equals 10^{15}. It is shown that the charge potential keeps rising when the particle radius is reduced from 1000 nm to 5 nm in all the three mechanisms. While the potential increases in a relatively moderate way in Mechanism III, in the other two mechanisms, the charge potential rises rapidly when the particle radius is smaller than 50 nm and reaches the potential cut-off of 5V even before the particle radius becomes zero. This potential rising is not due to the charge transport limitation, because the resistance of Li_2O_2 particles decreases with the reducing size. Instead, it results from the shrinkage of the active surface area. Unlike in LIBs where the active surface area is merely changed, in LOBs, the active surface area of the Li_2O_2 decomposition continuously decreases during the charge process due to the particle shrinking. Consequently, under a constant total applied current, the local current density increases and thus leads to the increase of the charge potential.

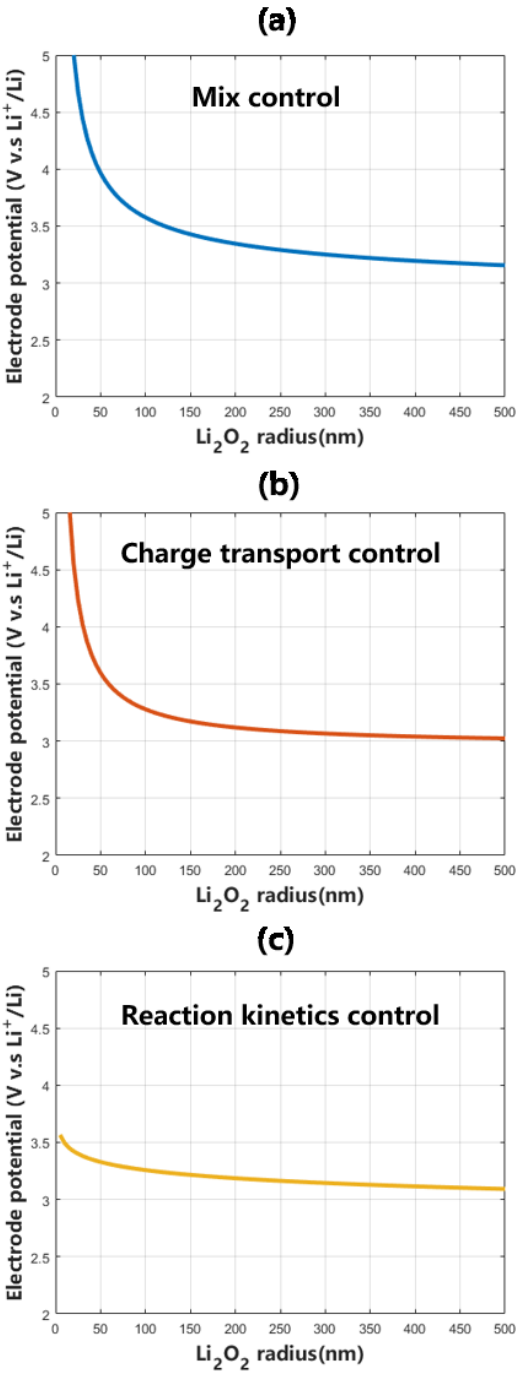

Figure 3.7: The evolution of electrode potential a function of particles radius by assuming the rate of Li_2O_2 decomposition is controlled by (a) both charge transport and reaction kinetics; (b) only charge transport and (c) only reaction kinetics. The population of Li_2O_2 in simulations is set as 1×10^{15} and the Li_2O_2 resistivity is 10^8 Ω·m.

Moreover, the success in explaining the uphill trend of electrode potential disproves the idea of assuming Li_2O_2 as a homogeneous layer deposited on the electrode.

This is because that in the layer assumption, the decomposition of Li_2O_2 only results in the decrease of Li_2O_2 thickness while the contact area between Li_2O_2 and electrode surface maintains constant. According to this assumption, the electrode potential is expected to decrease since the charge transport is improved, which is in contradiction with the experimental observations. Therefore, compared to the layer assumption, the particle assumption of the Li_2O_2 morphology constitutes a reasonable assumption in the model.

III.2 Bi-modal PSD and stepwise charging profile

Following the same initial condition as assumed in the cell model, the kinetic models are applied to simulate the oxidation of Li_2O_2 particles with an initial bi-modal PSD. In kinetic models, the evolution of PSD is solved in a discretized way. The Li_2O_2 particle size, which ranges from 0 to 500 nm, is divided into a series of size classes with a size step of 5 nm and the change of the particle size is considered as a particle flow between adjacent size classes *j* to *j-1*, which is marked as ΔN_j as follows,

$$\Delta N_j = -\frac{I_j F V_m}{\Delta V_j} dt \qquad 3.33$$

where I_j is the current obtained from decomposition of Li_2O_2 particles in radius *j*, V_m is the molar volume of Li_2O_2, ΔV_j is the volume difference of one particle between size class *j* and size class *j+1*. For particles in the first size class, the ΔV_1 is considered to be the volume of the particle. Therefore, the number of particle in size class *j* after *dt* can be obtained as

$$N_j^{t+dt} = N_j^t - \Delta N_j + \Delta N_{j+1} \qquad 3.34$$

The current obtained in radius class *j*, I_j, is solved according to

Mechanism I (mix control):

$$I_{I,j} = 2N_j \pi r_j^2 n F k_0 sinh(\frac{-\alpha n_e F\left(\Psi - \Phi + i_j \rho r_j\right)}{\mathrm{RT}} \qquad 3.35$$

Mechanism II (Charge transport control):

$$I_{II,j} = -\frac{\Psi - \Phi}{\rho} N_j r_j \quad 3.36$$

Mechanism III (Reaction kinetics control):

$$I_{III,j} = 2N_j \pi r_j^2 nFk_0 sinh(\frac{-\alpha n_e F(\Psi - \Phi)}{\mathrm{RT}}) \quad 3.37$$

where N_j is particle population in size class j. Summing up I_j from all the size classes should equal to the overall applied current,

$$I_{input} = \sum_j I_j \quad 3.38$$

The flowchart of the simulation is shown in **Figure 3.8** and the value of parameters used in the simulation are summarized in **Table 3.2.** A bi-modal size distribution is assumed as the initial condition of the model, where peak radius is at 10 and 500 nm. The size of large particles is determined from the SEM images as in the experimental work by Zhai *et al*,[107] and the size of the small particles is set to be close to the critical tunneling distance. After the initial condition being set, the time loop starts. In each iteration, we solved firstly the Ψ and I_j with the PSD updated from initial condition or previous iteration. Then, according to the I_j, we further solve the volume change of Li_2O_2 in each size class and update the PSD, which will be used in the next iteration. The time loop repeats until reaching the stop condition (the Ψ reaches the cut-off potential).

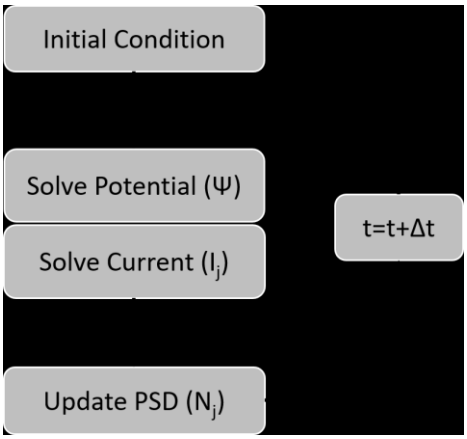

Figure 3.8: Flowchart of the charge model discussed in this section.

Table 3.2: Symbols of the parameters with associated values in the simulations.

Symbol	Parameters	Unit	Value
$I_{applied}$	Applied current density	mA/cm^2	0.1
Φ	Equilibrium potential	V v.s Li^+/Li	2.96
ρ	Resistivity of Li_2O_2	$\Omega \cdot m$	1×10^7
k_0	Heterogeneous rate constant	$mol/(s\cdot m^2)$	1×10^{-9}
dt	Time step	S	0.01

The simulation results of the baseline case, where the total volumes of small particles and large particles are considered to be equal, are presented in **Figure 3.9.** In all the cases, the charge profiles reveal two voltage plateaus. The potential gap between two plateaus is obviously larger in Mechanism I and II (**Figure 3.9 a and c**) as compared to Mechanism III (**Figure 3.9 e**), showing that the charge transport has a stronger dependence on the particle size.

This is confirmed by the PSD evolution as displayed in **Figure 3.9 b, d and f.** In all the three cases, the initial PSD, is shown with the blue curve, where two peaks with the same height are found at radius of 10 nm and 500 nm respectively. When the charge process proceeded to point B (250 mAh/g), located at the middle of low voltage plateau, the corresponding PSD is shown in red curve. It is observed that the height of peak at 10 nm decreases in all the three cases, indicating the decomposition of small particles. However, large particles change differently among the three cases. In Mechanism I and II, the height of the peak at radius of 500 nm is almost unchanged, indicating that large particles are not decomposed at the low voltage plateau. By contrast, in Mechanism III, it is observed that the peak at 500 nm becomes lower and wider, implying the decomposition of the large particles.

The PSD at the transition between the low voltage plateau to the high voltage plateau, as plotted with the yellow curves, confirms again the preferential decomposition in Mechanisms I and II. In these two cases, the peak at 10 nm completely

disappears, evidencing that the small particles are fully decomposed during the low voltage plateau. Meanwhile, large particles start to be involved in the charge reaction as revealed by the decrease of the height of peak at 500 nm. In contrast, the peak at 10 nm in Mechanism III is still visible, showing that there is still a certain number of small particles in the system during the transition between the two voltage plateaus. At the same time, the peak at 500 nm in Mechanism III not only becomes lower but also starts moving towards smaller radius, confirming that the large particles here participate in the charge reaction even before reaching the high voltage plateau.

When it comes to the high voltage plateau, the PSD of the three mechanisms are similar, as shown by the purple lines. At point D where the depth of charge equaling to 750 mAh/g, there are only large particles left in the system in all the three cases. Thus, the decomposition of large particles dominates the system.

These simulation results show that in all cases, smaller particles are preferentially decomposed at the low charge potential and large particles are oxidized at high charge potential. In Mechanisms I and II, the voltage difference is attributed to the dependence of ohmic drop on the particle size. However, in Mechanism III, where the ohmic drop is not considered, the stepwise charge profile is mainly correlated to the variation of local current density. Due to high surface-to-volume ratio, small particles have a larger active surface area as compared to large particles. As a result, the local current density is low at the initial stage of the charge process. Meanwhile, the fraction of total current attributed to the small particles is larger than that to large particles. Therefore, small particles decompose faster, consequently, the active surface area shrinks and the potential increases. However, the large particles shrink at a lower rate, resulting in a slower change in active surface area. Thus, when the potential is controlled by the decomposition of large particles, the cell voltage is relatively stable as a “plateau”.

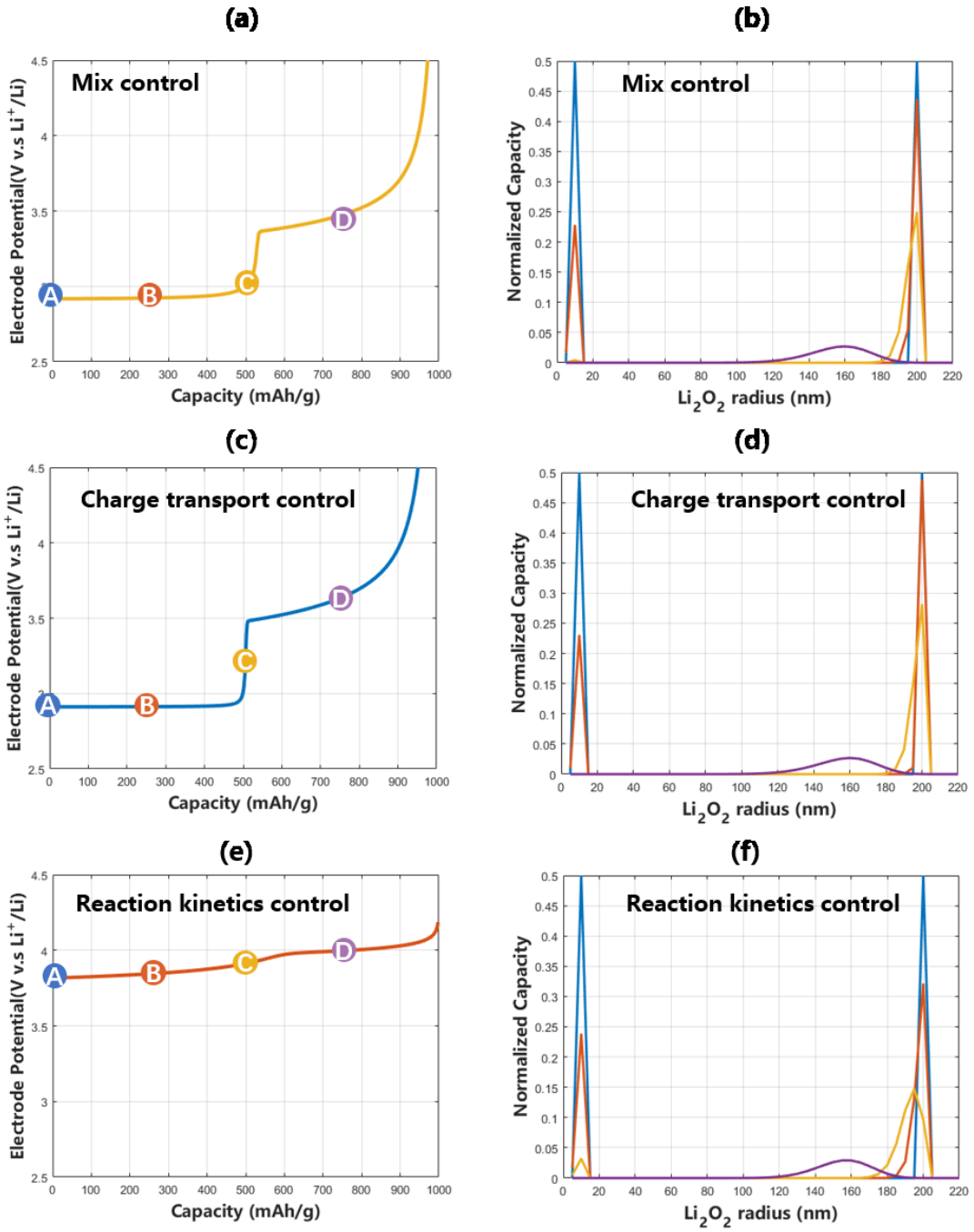

Figure 3.9: The simulated charging profile from the kinetic models considering the charge potential is controlled by: **(a)** both charge transport and reaction kinetics; **(c)** only charge transport and **(e)** only reaction kinetics. The PSD evolutions of Li_2O_2 obtained from these kinetic models are accordingly shown in **(b)**, **(d)** and **(f)**.

Moreover, it is found that the charge voltage reaches the cut-off voltage (4.5 V) before completed oxidation of Li_2O_2 in Mechanisms I and II. However, the charge voltage in experiments remains around 4.5 V even at the end of the charge process. This deviation of simulation results from the experiments is ascribed to the overlook of the

side reactions in the model, such as the decomposition of electrolyte and carbonate formed from carbon corrosion. Though the current density drawn from Li_2O_2 oxidation kept decreasing due to the shrinking of the particles, the side reactions made it up and thus prevent the electrode potential from continuous rising. However, these side reactions can bring about a low columbic efficiency and indicate that the formed Li_2O_2 could not completely oxidized unless with over-charging.

Furthermore, it is reported in the experimental references that the discharge current densities showed impact on the charging profiles. With the same charging current density, the charge profile has a longer low voltage region if the cell discharged at a higher current. Bearing in mind the influence of discharge current densities on the size of Li_2O_2 particles,[35,79] we proposed that the variation of the charging profiles is due to the changes of Li_2O_2 PSD as resulted from different discharge current densities. At higher discharge rates, it is expected to have larger proportion of the Li_2O_2 in the form of small particles (thin-film), whereas at lower rates Li_2O_2 particles get coalesced into larger particles.

The simulation of the impact of discharge history on charging profiles requires information of the Li_2O_2 PSDs obtained from different discharge current densities. That information is missing in the experimental references and there is a lack of available modeling tool for that at the moment we develop the charge model. However, a reverse-engineering approach could be applied by fitting the experimental charging profiles to obtain the population and sizes of the Li_2O_2 particles at each current density.

The simulated profiles obtained from the mix-control kinetic model were plotted in **Figure 3.10 a**, which reproduced well the experimental results from Zhai *et al.*[107] as shown in **Figure 3.10 b**. The size of the small particles was set at 10 nm in all the cases, yet the ratios of their total volume varies from 30% to 50% and 70%, associated to the discharge current densities of 0.05, 0.1 and 0.2 mA/cm^2 in experiments. While for the large particles, except for the volumetric ratio, their sizes also changed correspondingly to 500, 400 and 380 nm. Though there is not quantitative confirmation from experiments, the calculated decreasing trend of the size of Li_2O_2 particles agrees with the experimental observations.

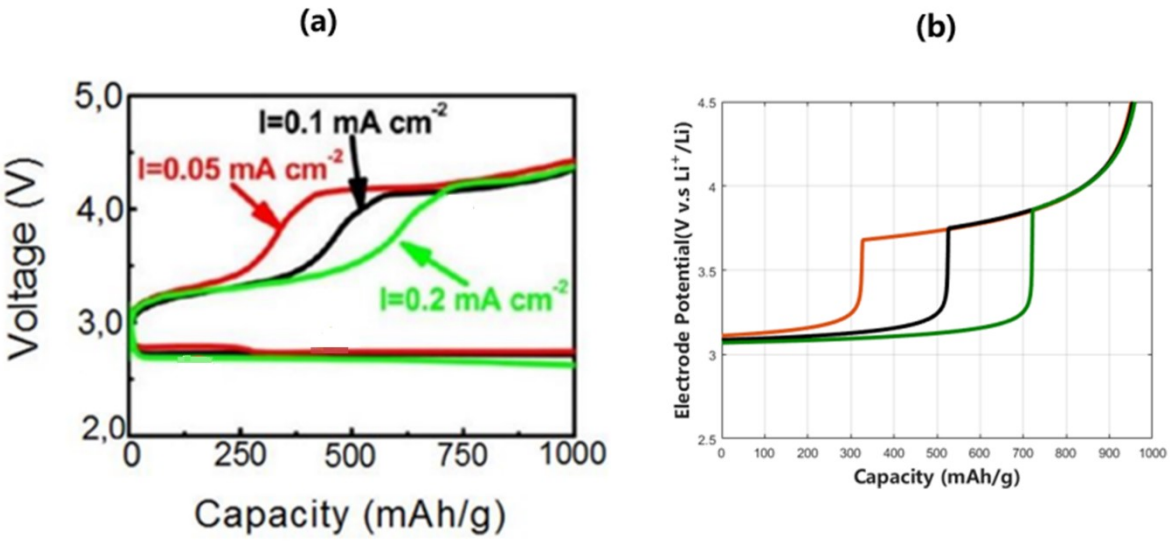

Figure 3.10: Experimental voltage profiles of Li-O_2 batteries that discharged at rate of 0.05, 0.1 and 0**(a)**.2 mA/cm^2 until 1000 mAh/g_{AC} respectively, then all charged at rate of 0.1 mA/cm^2; **(b)** Simulated charging profiles from the presenting charge model with different PSD of Li_2O_2. The volumetric ratios of large particles are 70%, 50% and 30%, respectively with a radius of 500, 450 and 380 nm correspondingly. Figure **(a)** is reprinted from reference [107].

IV. Conclusions

In this chapter, a cell model based on a continuum approach has been proposed to simulate the charge process. Both reaction kinetics and mass transport are considered in the model. It is considered that the charge mechanisms depend on the particle size. For large particles formed from the solution mechanism, their decomposition requires to overcome an activation energy barrier of 0.4 V, which is not necessary for small Li_2O_2 particles formed through the surface mechanism. As a result, smaller particles are preferentially decomposed at lower voltage in comparison to the large particles, resulting in a stepwise charge profile.

In parallel, kinetic models have been developed and used to study the dependence of the charge potential on the particle size. The simulation results show that the potential rising during the charge process is due to the shrinking of the active surface area. Besides, with the assumption of bi-modal PSD of Li_2O_2, these models also reproduced the stepwise charging profiles as obtained from experimental results and further correlated the two voltage plateaus to the decomposition of Li_2O_2 particles with different sizes. Moreover, according to the model, the dependence of charging profiles

on the discharge history can be explained by the changing of Li_2O_2 PSD at different discharge current densities.

However, compared to the experimental results, the transition between the two voltage plateaus in the simulation results is less smooth, which could be improved by replacing the bi-modal PSD with a detailed PSD. Thus, a discharge model that is capable to provide the Li_2O_2 PSD is required, which motivated us to develop the Li_2O_2 nucleation model as presented in the next chapter.

Chapter 4 : Continuum Model for Discharge Process of Li-O_2 Batteries

As suggested by the charge model, the charging process is correlated closely to the particles size distribution of Li_2O_2 formed upon discharge. However, this has not been implemented in previous discharge models developed at LRCS.[97,142] Thus, during this PhD thesis, a novel continuum model was built by combining classical nucleation theory, detailed reaction kinetics and mass transport, to simulate the discharge process in LOBs and to track the evolution of Li_2O_2 size distribution. The content of this Chapter is based on the paper: Y. Yin, A. Torayev, C. Gaya, Y. Mammeri, and A. A. Franco, *J. Phys. Chem. C*, **121**, 19577–19585 (2017).

I. Model Descriptions

The discharge model is built on a 1D representation of the cell along the direction from the anode surface to the separator and cathode (**Figure 4.1**). The transport of soluble species is solved by using the finite volume method in the domains of cathode and separator, which have been discretized into P and Q bins respectively, and the reaction kinetics are solved only in the cathode.

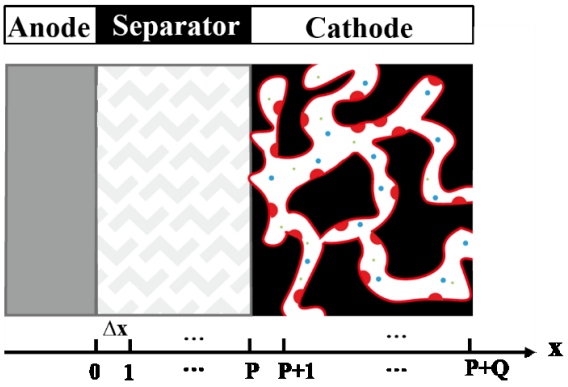

Figure 4.1: Finite volume scheme of our Li-O_2 battery model. The mass transport is solved from the anode/separator (0) to the air inlet (P+Q). The formation/consumption of species from reactions as well as the particle growth are solved in each bin of the cathode electrode.

I.1 Discharge mechanism

During the discharge process, the Li_2O_2 particles are formed and then grow through multiple steps as summarized in **Figure 4.2**.

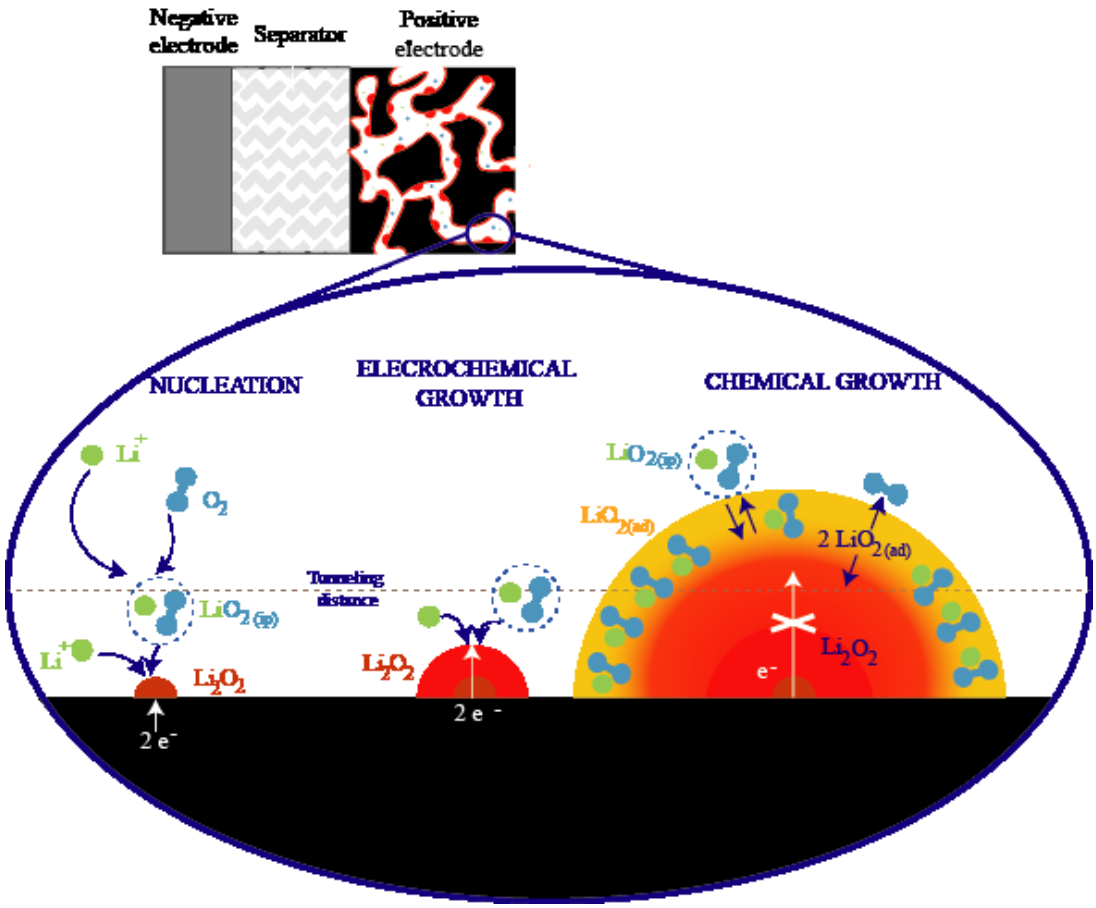

Figure 4.2: Schematic illustration of the configuration and discharge process of a Li-O_2 battery cell.

At first, the dissolved O_2 diffuses to the electrode surface, being reduced with the presence of Li^+ to form LiO_2:

$$Li^+ + O_2 + e^- \leftrightarrow LiO_{2(ip)} \qquad 4.1$$

It is reported that this reaction occurs by outer sphere charge transfer without O_2 adsorption on the electrode and the formed LiO_2 is more likely in the form of ion pair in the solution,[85,163] noted as $LiO_{2(ip)}$. When being close to the electrode surface, $LiO_{2(ip)}$ can be further reduced to Li_2O_2 with another Li^+:

$$LiO_{2(ip)} + Li^+ + e^- \rightarrow Li_2O_2 \qquad 4.2$$

This reduction can take place either on the electrode surface or on the surface of Li_2O_2 if the charge transfer through the Li_2O_2 by tunneling is still available.To distinguish the above two processes, the former is named *nucleation* while the latter is referred as *electrochemical growth* of Li_2O_2.

Simultaneously to the reduction, $LiO_{2(ip)}$ could also be adsorbed on the surface of Li_2O_2 particles as $LiO_{2(ad)}$:

$$LiO_{2(ip)} \leftrightarrow LiO_{2(ad)} \tag{4.3}$$

especially when the particle size is too large to support the tunneling current.[99,164] The existence of LiO_2-like component on the surface of Li_2O_2 is confirmed by Raman spectroscopy[110] and DFT calculations show that the adsorption of $LiO_{2(ip)}$ is thermodynamically favored.[165] If still within the tunneling distance, the $LiO_{2(ad)}$ could also be reduced to Li_2O_2 with Li^+:

$$LiO_{2(ad)} + Li^+ + e^- \rightarrow Li_2O_2 \tag{4.4}$$

which is also considered as *electrochemical growth* of Li_2O_2.

Moreover, Li_2O_2 could also grow through a disproportionation reaction. Considering that the interactions between $LiO_{2(ip)}$ are generally weakened by the solvation shell, disproportionation occurs more likely with partial desolvated $LiO_{2(ad)}$:

$$LiO_{2(ad)} \rightarrow Li_2O_2 + O_2 \tag{4.5}$$

This growth pathway of Li_2O_2 does not involve the electron exchange with electrode, thus it is named in this manuscript as *chemical growth*.

I.2 Nucleation of Li_2O_2

The Gibbs free energy (ΔG) correlated to the formation of a Li_2O_2 cluster in the electrolyte consists of two terms: the bulk free energy (ΔG_V) which is proportional to its volume (V), and the surface free energy (ΔG_S) which is proportional to its surface area (A). As the volume and surface area of the cluster are functions of its radius r, ΔG also evolves with r which is mathematically formulated as follows,

$$\Delta G(r) = \frac{V(r)}{\omega_{Li_2O_2}} \Delta\mu + \sigma A(r) \quad 4.6$$

where $\omega_{Li_2O_2}$ is the molar volume of Li_2O_2, $\Delta\mu$ is the excess potential which refers to the difference of (electro)chemical potential between the electrolyte and Li_2O_2 cluster and σ is the average surface tension. Assuming Li_2O_2 as hemispherical particles, their volume and surface area are written as

$$V(r) = \frac{2}{3}\pi r^3 \quad 4.7$$

$$A(r) = 2\pi r^2 \quad 4.8$$

In spontaneous nucleation, $\Delta\mu$ is usually negative while σ is usually positive. The interplay between volume and surface free energy leads to a bending shape of the *ΔG-r* profile as shown in **Figure 4.3**. With the increase of the particle radius, *ΔG(r)* rises at the beginning due to the large surface energy of smaller particles. However, while the surface area increases quadratically with the radius, the volume of the cluster grows even faster in a cubic manner. Therefore, the increase of *ΔG(r)* slows down and after reaching a maximum point, it starts to decrease when the particle radius further increases.

The maximum point of *ΔG* is called *nucleation barrier* (ΔG_{crit}) and the corresponding radius is the critical radius (r_c). Particles having a radius below r_c are unstable nucleus, which are prone to decrease rather than grow to have a smaller *ΔG*. Several unstable nuclei may also coalesce to form a larger particle, which forms a seed once its radius exceed r_c. The growth of seed is thermodynamically favored as the *ΔG* decreases. Moreover, when the *ΔG* decreases to zero, the corresponding *r* is noted as r_0. Stable particles are formed when the radius of seed becomes larger than r_0.

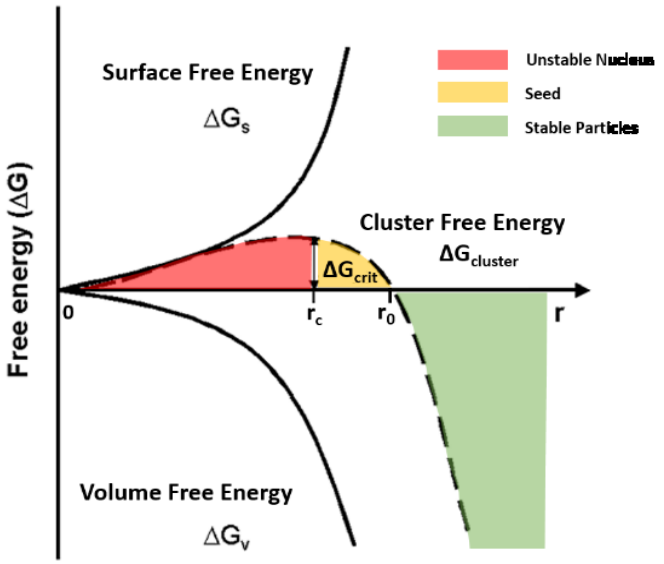

Figure 4.3: Free energy diagram for nucleation.[166]

It is obvious that the derivative of ΔG at r_c equals zero as follows

$$\left.\frac{\partial \Delta G(r)}{\partial r}\right|_{r=r_c} = 0 \qquad 4.9$$

Therefore, r_c and ΔG_{crit} can be solved by combining **Eqs. 4.6-4.9** as follows

$$r_{crit} = \frac{2\sigma V_m}{\Delta u} \qquad 4.10$$

$$\Delta G_{crit} = \frac{8\pi V_m^2 \sigma^3}{3\Delta \mu^2} \qquad 4.11$$

However, when the nucleation takes place on the substrate surface, the interaction between the nuclei and the substrate should be also considered and heterogeneous nucleation should be applied. The energy barrier of a heterogeneous nucleation has the following relationship with the homogeneous nucleation[167]

$$\Delta G_{crit}^{het} = \Delta G_{crit}^{hom} \frac{\sigma + \sigma_i - \sigma_s}{2\sigma} \quad 4.12$$

where σ, σ_i and σ_s refer to the specific surface energies of the precipitate face, precipitate/electrode interface and electrode surface. According to the Dupré relation:[167]

$$\sigma_i = \sigma + \sigma_s + \frac{E_b}{A_i} \quad 4.13$$

where E_b is the binding energy of the solid on the electrode and A_i is the contact area between. Applying **Eqs. 4.12-13** to **Eq. 4.11** gives,

$$\Delta G_{crit}^{het} = \frac{8{V_m}^2\sigma^3}{3\Delta\mu^2}\left(1 + \frac{E_b}{2\sigma A_i}\right) \quad 4.14$$

Considering the nucleation barrier as the activation energy of the nucleation process, the nucleation rate (v_{nu}) is then given by

$$v_{nu} = k_{nu}\exp\left(-\frac{\Delta G_{crit}^{het}}{k_b T}\right) \quad 4.15$$

where k_{nu} is the kinetic rate constant for the nucleation process, k_b is the Boltzmann constant. According to **Eq. 4.15**, the larger is the ΔG_{crit}^{het}, the slower will be the nucleation process.

Looking back to **Eq. 4.14**, it can be noticed that the ΔG_{crit}^{het} is a function of σ and E_b, which describes the Li_2O_2/electrolyte interaction and Li_2O_2/electrode interaction, respectively. **Thus, both the electrolyte and the electrode properties will impact the nucleation process.**

Moreover, ΔG_{crit}^{het} depends also on $\Delta\mu$, which is correlated to the electrochemical overpotential η. Since η is defined as the potential difference between the discharge potential E and the equilibrium potential of $LiO_{2(ip)}$ reduction E^{eq}, $\Delta\mu$ can be written as follows

$$\Delta u = ze\eta = ze(E - E^{eq}) \quad 4.16$$

Consequently, the change of the electrode potential causes variation of $\Delta\mu$ and thus impacts on the ΔG_{crit}^{het} and nucleation rate.

I.3 Reaction kinetics

Similar to the charge model described in **Chapter 3**, the kinetics of the electrochemical reaction is solved with:

$$i_j = nFv_j = nF\left\{k_{f,j}\prod_i a_i^{s_{i,j}}\exp\left(\frac{(1-\alpha)nF(\Psi-\phi)}{RT}\right) - k_{b,j}\prod_i a_{i,j}^{s_{i,j}}\exp\left(\frac{-\alpha nF(\Psi-\phi)}{RT}\right)\right\} \quad 4.17$$

For the electrochemical reactions that occurs on the Li_2O_2 surface which depends on charge tunneling, the reaction rates are function of the Li_2O_2 size,

$$v_j(\delta) = v_j(0)\cdot\tau(\delta) \quad 4.18$$

where δ is the tunneling distance while $\tau(\delta)$ is the tunneling efficiency which can be described with an error function as follows[99,142]

$$\tau(\delta) = \frac{1 - erf(\delta - 7)}{2} \quad 4.19$$

The evolution of the tunneling efficiency with the tunneling distance is shown in **Figure 4.4**. It is found that once the tunneling distance reaches a critical value (δ_{crit}), which is around 5-10 nm, the tunneling coefficient drops to 0 and no electrochemical growth can take place any more. Though the distances between the electrode and different parts of the same particle varies, the particle radius is considered as the tunneling distance applied to the entire particle to be consistent with the assumption of isotropic growth.

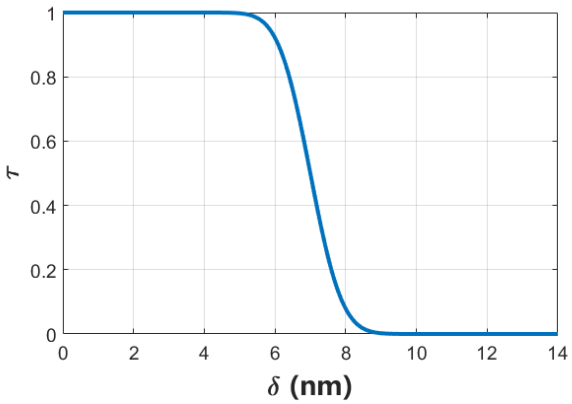

Figure 4.4: The efficiency of charge tunneling across Li_2O_2 particles as a function of tunneling distance.

Integrating the current density over the surface area of charge transfer gives the overall current from reaction j

$$I_{input} = \int \sum_j \frac{A_j}{V} i_j dV \qquad 4.20$$

For reactions taking place on the electrode surface, A_j refers to the surface area of the uncovered part. For reactions on the surface of Li_2O_2 particles, A_j then equals the contact surface area between the particle and the electrode surface. The overlap of the particles is not considered in the model, but the following numerical constrain is applied to prevent the surface area from becoming negative:

$$A_j = \begin{cases} A_j, & A_j \geq 0 \\ 0, & A_j < 0 \end{cases} \qquad 4.21$$

The chemical reactions that are considered in the model are the adsorption of $LiO_{2(ip)}$ and disproportionation of $LiO_{2(ad)}$. The rate of the $LiO_{2(ip)}$ adsorption is assumed to be proportional to the difference between the $LiO_{2(ip)}$ concentration in electrolyte and its saturation concentration ($c^0_{LiO_{2(ip)}}$),

$$v = k(c_{LiO_{2(ip)}} - c^0_{LiO_{2(ip)}}) \qquad 4.22$$

where k is the rate constant of the adsorption/desorption. When $c_{LiO_{2(ip)}}$ is larger than the saturation concentration, the $LiO_{2(ip)}$ is supersaturated and its adsorption is favored; on the contrary, when the $c_{LiO_{2(ip)}}$ is smaller than $c^0_{LiO_{2(ip)}}$, the $LiO_{2(ad)}$, if there is any, would dissolve back to the electrolyte and the adsorption rate will become negative.

However, the saturation concentration is not constant and it shows dependence on the particle radius according to the Ostwald-Freundlich equation as follows:[168,169]

$$c^0_{LiO_{2(ip),r}} = c^0_{LiO_{2(ip),\infty}} \exp\left(\frac{2\sigma_{LiO_2}\omega_{LiO_2}}{RTr}\right) \quad 4.23$$

where $c^0_{LiO_{2(ip),\infty}}$ is the saturation concentration for bulk LiO_2 solid, σ_{LiO_2} is the surface tension of $LiO_{2(ad)}$, ω_{LiO_2} is the molar volume of $LiO_{2(ad)}$ which is assumed to be similar to that of Li_2O_2. r is the radius of a lithium oxides hemispherical particle. Combining **Eq. 4.21**, the adsorption kinetics can be rewritten as:

$$v = kc_{LiO_{2(ip)}} - k_b \exp\left(\frac{2\sigma_{LiO_2}V_{e,LiO_2}}{RTr}\right) \quad 4.24$$

with $k_b = kc^0_{LiO_{2(ip),\infty}}$ According to the above equation, the adsorption of $LiO_{2(ip)}$ on smaller particles will be slower than that on larger particles.

As for the disproportionation of $LiO_{2(ad)}$, the reaction is assumed to have a first order kinetics with respect to $LiO_{2(ad)}$ as suggested by Peng *et. al.* from experimental observation:[50]

$$v = kn_{LiO_{2(ad)}} \quad 4.25$$

The reason of the inconsistency between the observation and reaction stoichiometry is still unclear, which relies on further investigations to provide more insight. Moreover, as Li_2O_2 is the most stable phase under the conventional operation condition of LOBs (298K, 1 atm),[170] the disproportionation reaction is considered as an irreversible process that follows only the forward direction.

I.4 Evolution of Li_2O_2 particle size distribution

Solving the evolution of Li_2O_2 particle size distribution (PSD) is not trivial and its complexity comes from the following aspects:

(a) Li_2O_2 can grow through both electrochemical and chemical pathway;

(b) the growth rate of Li_2O_2 has dependence on the particle size due to the size-dependent $LiO_{2(ip)}$ adsorption and charge tunneling;

(c) the PSD may vary at different depths of the electrode.

In our model, the range of particle radius in discretized into K classes and as mentioned previously, the positive electrode has been divided into Q bins along the electrode thickness. Thus, the PSD, is recorded in a K×Q matrix, marked as *f*. As shown in **Figure 4.5**, the element at row *i* and column *j* in *f* is noted as $N_{i,j}$, which represents the particle number of radius class *i* in bin *j*. The evolution of PSD in each bin is solved independently. The size change of particles, growth or shrinkage, is considered as the particle flow between size classes.

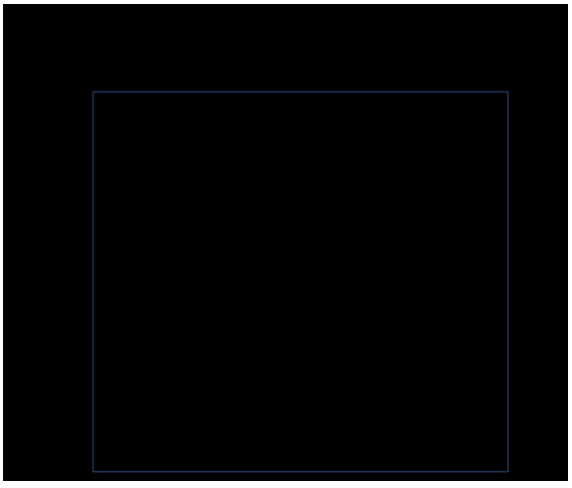

Figure 4.5: Schematic representation of the matrix *f* which records the PSD of Li_2O_2 in positive electrode.

The total volume change of the k_{th} radius class (ΔV_k^{total}) equals to the product of particle number (N_i) and the volume change of a single particle (ΔV_k,) in the radius class:

$$\Delta V_k^{total} = N_k \Delta V_r \tag{4.26}$$

Positive value of ΔV_k^{total} indicates the growth of the particle, which negative value means the shrinkage. Dividing the ΔV_k^{total} by the volume difference Δw of adjacent size classes gives the number of particles leaving the size class as follows

$$\begin{aligned} \Delta N_k^+ &= \frac{\Delta V_k^{total}}{\Delta w_{k\to k+1}} \quad if \quad \Delta V_k^{total} > 0 \\ \Delta N_k^- &= -\frac{\Delta V_k^{total}}{\Delta w_{k\to k+1}} \quad if \quad \Delta V_k^{total} < 0 \end{aligned} \tag{4.27}$$

To have a more general mathematical formation, it is also defined that

$$\begin{aligned} \Delta N_k^- &= 0 \quad if \quad \Delta V_k^{total} > 0 \\ \Delta N_k^+ &= 0 \quad if \quad \Delta V_k^{total} < 0 \end{aligned} \tag{4.28}$$

Considering the conservation of the particle number, the new particle number equals to the previous particle number minus the number of particles that flow out (ΔN_k^+, ΔN_k^-), then plus the number of particle that flow in (ΔN_{k-1}^+, ΔN_{k+1}^-), in addition to the number of particles formed from the nucleation ($\Delta N_{nu,k}$)

$$N_k(t+\Delta t) = N_k(t) - \Delta N_k^+ - \Delta N_k^- + \Delta N_{k-1}^+ + \Delta N_{k+1}^- + \Delta N_{nu,k} \tag{4.29}$$

when r_k is the critical radius, $\Delta N_{nu,k}$ can be calculated from the nucleation rate (v_{nu}) as follows,

$$\Delta N_{nu,k} = \frac{v_{nu} A_{nu}}{V_{crit}} \tag{4.30}$$

where A_{un} is the electrode surface area that is available for nucleation and V_{crit} is the volume of a particle at critical radius. Otherwise, $\Delta N_{nu,k}$ equals to zero.

I.5 Mass Transport

Similarly to in **Chapter 3**, diffusion is considered as the main driven force for the mass transport, which can be solved according to the porous electrode theory based on the combination of first and second Fick's law (**Eq. 3.17**, page 56 of this manuscript).

The cell parameters are mainly adapted from in-house experiments based on gas-diffusion layer electrodes and 1M $LiClO_4$/DMSO electrolyte. Values of parameters used in the simulations are summarized in **Table 4.1.**

Table 4. 1: Values of parameters used in the cell model for charge process.

Parameters	Values	Units	Sources
Cell parameters			
Cathode thickness	2.35×10^{-4}	m	Measured
Electrode specific surface area	0.231	$m^2.g^{-1}$	Measured
Bruggeman coefficient	1.5	/	
Pristine cathode porosity	0.81	/	Measured
Separator porosity	0.5	/	Assumed
Li^+ initial concentration	1×10^3	mol m^{-3}	Measured
O_2 initial concentration	1.86	mol m^{-3}	Ref[161]
$LiO_{2(ip)}$ initial concentration	0.1	mol m^{-3}	Assumed
$LiO_{2(s)}$, Li_2O_2 molar volume	1.98×10^{-5}	m^3 mol^{-1}	Ref [106]
Li^+ diffusion coefficient	1×10^{-9}	m^2 s^{-1}	Ref[161]
O_2 diffusion coefficient	1.67×10^{-9}	m^2 s^{-1}	Ref[161]
$LiO_{2(ip)}$ diffusion coefficient	1.3×10^{-9}	m^2 s^{-1}	Assumed
Surface energy of Li_2O_2/electrolyte	0.75	$J.m^{-2}$	Ref[177]
Binding energy of Li_2O_2/carbon	-0.26	eV	Ref[181]
Electrochemical parameters			
Applied charge current	0.2	A $m^{-2}_{geometric}$	Measured
Standard potential of LiO_2/Li_2O_2	2.96	V v.s. Li^+/Li	assumed
Standard potential of LiO_2/O_2	2.96	V v.s. Li^+/Li	Ref[35]
Charge transfer coefficients	0.5	/	Assumed
Kinetic parameters			
rate constant of O_2 reduction	1×10^{-7}	$mol.s^{-1}.m^{-2}$	Fitted
rate constant of nucleation	1×10^{-60}	$mol.s^{-1}.m^{-2}$	Fitted
rate constant of $LiO_{2(ip)}$ reduction	1×10^{-7}	$mol.s^{-1}.m^{-2}$	Fitted
rate constant of $LiO_{2(ip)}$ adsorption	1×10^{-8}	$mol.s^{-1}.m^{-2}$	Fitted
rate constant of $LiO_{2(ad)}$ reduction	1×10^{-7}	$mol.s^{-1}.m^{-2}$	Fitted
rate constant of $LiO_{2(ad)}$ disproportionation	2.9×10^{-3}	$mol.s^{-1}.m^{-2}$	Ref[50]

II. Results Analysis and Discussion

II.1 Bending shape of the discharge curve

The textural parameters (porosity, specific surface area) correspond to an electrode made from gas diffusion layer (GDL) and the electrolyte is a 1M $LiClO_4$/DMSO solution, where the saturation concentration of $LiO_{2(ip)}$ is assumed to be 0.1 mM. The baseline discharge rate is 0.2 A/m^2 with respect to the geometrical surface area of the electrode.

It is commonly observed in literature that there is a potential dip at the initial stage of a galvanostatic discharge of a LOB, especially when high DN solvents such as DMSO are used in the electrolyte.[34,37,97,171,172] As shown in **Figure 4.6 a**, this behavior is well captured by the present model, which is closely correlated to the nucleation process.

By plotting the reaction rates during the discharge process (**Figure 4.6 b**), it is found that the discharge current is mainly from the reduction of O_2, which thus drives the electrode potential. During the initial stage of discharge (stage I), $LiO_{2(ip)}$ is accumulating in the electrolyte (**Figure 4.6 c**), leading to the decrease of the equilibrium potential of the O_2 reduction according to the Nernst equation,

$$E^e = E^0 + \frac{RT}{zF}\ln\frac{c_{Li^+}c_{O_2}}{c_{LiO_{2(ip)}}} \qquad 4.31$$

To maintain the galvanostatic condition, the electrode potential also decreases accordingly. However, the energy barrier of the electrochemical nucleation is lowered by this drop of electrode potential and nucleation of Li_2O_2 is enhanced. As a result, a lot of Li_2O_2 nuclei are formed, along with the successive quick $LiO_{2(ip)}$ adsorption, leading to the decrease of $LiO_{2(ip)}$ concentration and raising of the electrode potential.

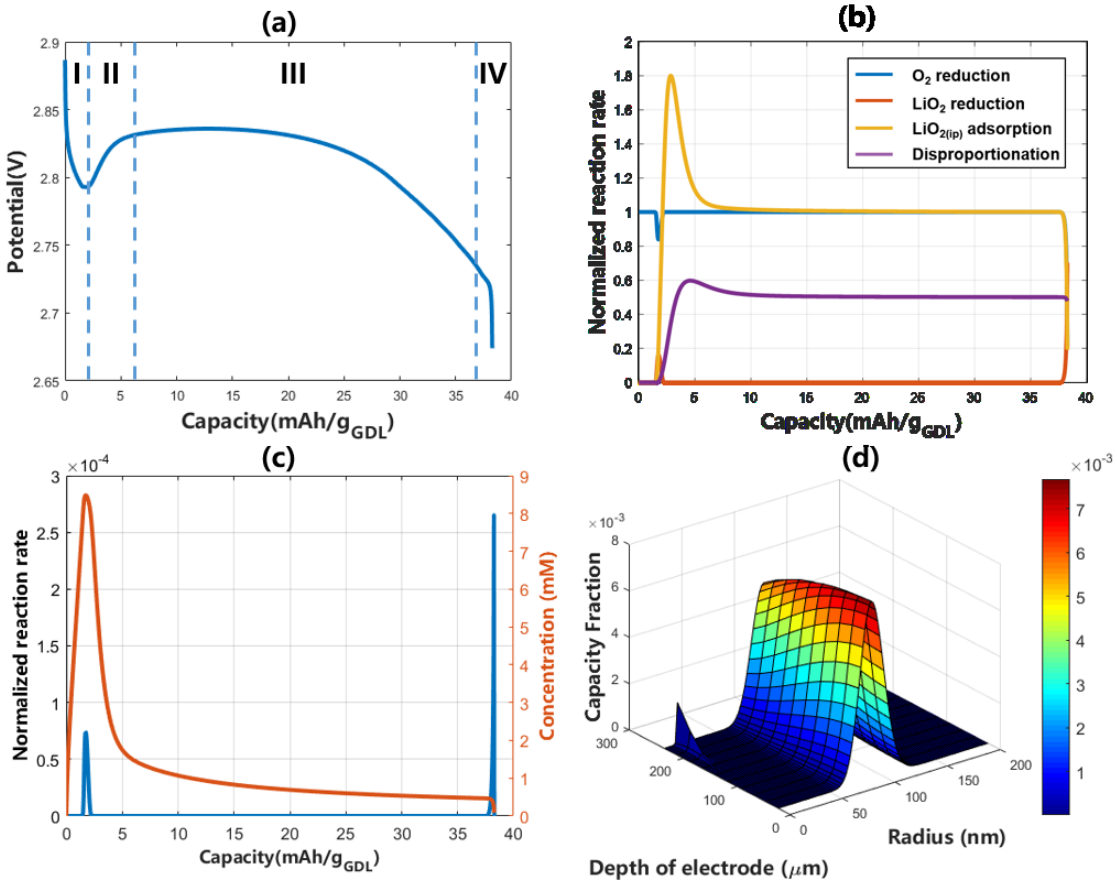

Figure 4.6: Simulation results for a Li-O_2 cell with a GDL cathode: **(a)** the calculated potential profile during the discharge process and its four stages; **(b)** the reaction rate of O_2 reduction (blue), electrochemical growth of Li_2O_2 (reduction of $LiO_{2(ip)}$ and $LiO_{2(ad)}$, red), chemical growth of Li_2O_2 (adsorption of $LiO_{2(ip)}$, yellow) and LiO_2 disproportionation (purple); **(c)** the evolution of the nucleation rate and $LiO_{2(ip)}$ concentration during the discharge process; **(d)** the PSD at the end of the discharge process. The reaction the **(b)** and **(c)** are normalized to the input current.

Under the simulated condition, the present model predicts that the nucleation is more likely to occur in an instantaneous way as shown in **Figure 4.6 c**. This behavior can be explained by the dependence of the nucleation rate on the $LiO_{2(ip)}$ and electrode potential. As plotted in **Figure 4.7 (a)**, rather than a progressive change as a function of the $LiO_{2(ip)}$, the nucleation rate raises suddenly when the system arrives at the nucleation zone in the *c*-E map. While the $LiO_{2(ip)}$ concentration decreases below the threshold value, which is around 7 mM at 2.8 V, nucleation rate drops until reaching zero (**Figure 4.7 b**). By considering that the thin film can be represented by a layer of small particles, this abrupt change of the nucleation rate agrees with the experimental observations that the transition of Li_2O_2 morphologies between thin film and large particles occurs at a small current range.

Afterwards, the system reaches a quasi-steady state as evidenced by a voltage plateau in the discharge profile (stage III). On one hand, the rates of $LiO_{2(ip)}$ formation is almost equal to its adsorption rate, leading to an almost constant $LiO_{2(ip)}$ concentration with a slight decreasing trend; on the other hand, the rates of $LiO_{2(ad)}$ formation is close to its consumption rate in the disproportionation reaction. As a result, the overall O_2/e^- of the system is predicted to be around 2, which is consistent with the DEMS results reported by Lepoivre *et al.* [173]

However, with the growth of the particles, the reaction surface area of O_2 reduction, which refers to the uncovered area of the electrode, keeps shrinking. To maintain the galvanostatic discharge, the overpotential of the electrode increases to enhance the local kinetics of the O_2 reduction, leading to the decrease of the electrode potential (Stage III). The second nucleation process starts when the electrode potential drops to a threshold value (**Figure 4.7 c**). The formation and growth of the newly formed Li_2O_2 nuclei aggravates the electrode passivation, resulting in the "sudden death" in the discharge process (Stage IV).

The two nucleation processes at the initial and final stage of the discharge account for the bi-modal size distribution of the Li_2O_2 particles at the end of discharge as revealed in **Figure 4.6 d**. Li_2O_2 particles that are formed during the first nucleation grown into large particles with radius of ~100 nm, while the Li_2O_2 formed during the second nucleation have radius less than 10 nm due to the limited growth time. Moreover, the spatial distribution of the two groups of Li_2O_2 differs from each other. More larger

particles are formed closed to the O_2 inlet than the part close to the separator, which can be correlated to the $LiO_{2(ip)}$ concentrations gradient. The small particles have the opposite trend due to the difference in the surface area of uncovered electrode surface.

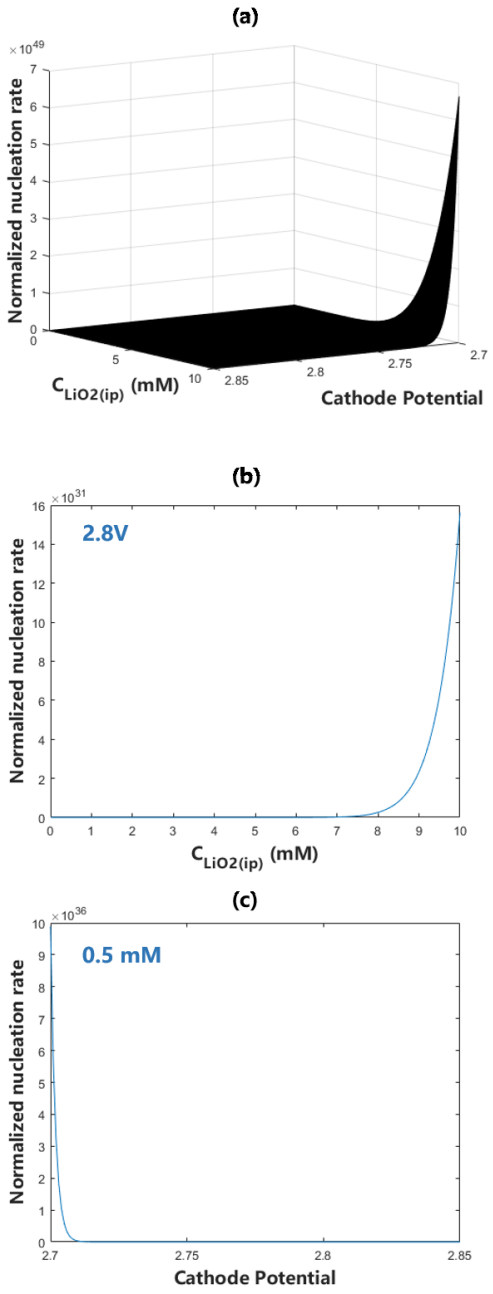

Figure 4.7: Simulated nucleation rate **(a)** as a function of cathode potential and $LiO_{2(ip)}$ concentration; **(b)** as a function of Li^+ concentration at 2.8 V; **(c)** as a function of cathode potential with a $LiO_{2(IP)}$ concentration at 0.5 mM.

II.2 Impact of current density

The impact of the current density on the discharge of LOBs have been investigated with the present model. Though the cathode materials are not the same, the discharge profiles obtained from the model at current densities of 0.1, 0.5 and 1 A/m^2 (**Figure 4.8 a**) are in good qualitative agreement with the experimental results reported by Girishkumar *et al.* (**Figure 4.8 b**) after adding an ohmic series resistance.[174]

Higher discharge current requires higher overpotential and results in faster formation of $LiO_{2(ip)}$, leading to more fierce nucleation which could even occur in a continuous way as found in the case with current of 1A/m^2. As a result, more particles are formed at high current condition, leading to fast passivation of the electrode and a relative low discharge capacity. Consistently, owing to sufficient space and time for growth, the radius of Li_2O_2 particle formed during the first nucleation process at current of 0.1 A/m^2 could reach ~125 nm, which is much higher than those formed at current of 0.5 A/m^2 (50 nm) and 1 A/m^2 (20 nm). The two peaks in the PSD of Li_2O_2 become closer and closer with the increase of discharge current (**Figure 4.8 c**), implying that they may merge together at a current higher than 1 A/m^2 according to the simulation. However, considering that the $LiO_{2(ip)}$ concentration on the electrode surface is larger than the average value as used in the model, this merging may occur even below 1 A/m^2.

Moreover, the capacity fraction from Li_2O_2 formed after the first nucleation process also increases with the ris of discharge current. As the oxidation of the Li_2O_2 during the charge process shows dependence on the particle size, [175,176] the influence of the discharge history on the charge profiles, which have already been observed in experiment,[107] can be correlated to the varying PSD of Li_2O_2 as a function of the discharge current.

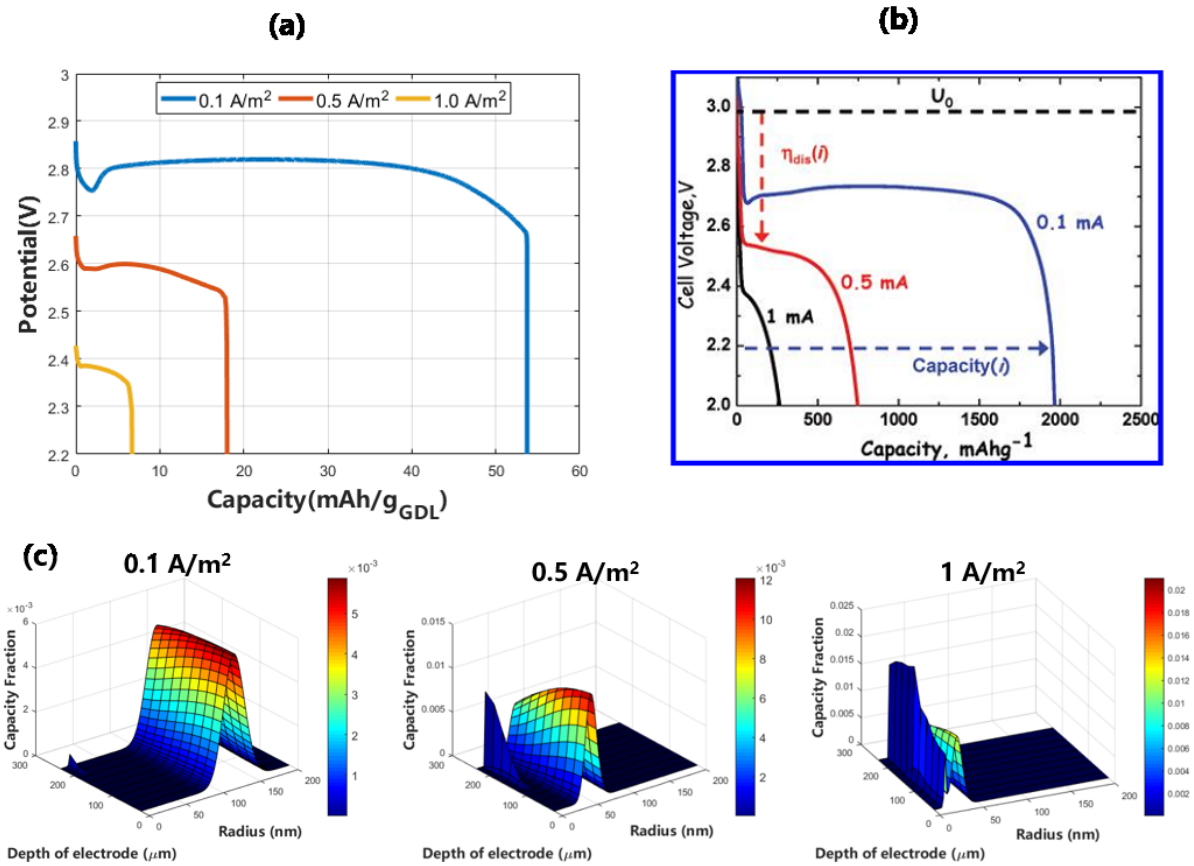

Figure 4.8: **(a)** Calculated discharge curves of Li-O_2 batteries at 0.1 (blue), 0.5 (red), 1.0(yellow) mA/cm^2; **(b)** Experimental discharge curves for an aprotic Li-O_2 cell (based on a Ketjenblack cathode) at 0.1, 0.5 and 1 mA/cm^2; **(c)** Simulated final PSD corresponding to the discharge curves in **(a)**. **(b)** is from Ref. [174].

II.3 Impact of electrolyte property

The impact of the electrolyte on the nucleation process has been captured with the parameter σ, which represents the surface energy between the Li_2O_2 and electrolyte. Though the exact value of σ for Li_2O_2 in DMSO is not available in the literature, the average surface energy of Li_2O_2 in the O_2 atmosphere is found to be around 0.77 J/m^2 according to DFT calculations.[177] Considering that the immersion of Li_2O_2 in the electrolyte usually leads to a decrease of the surface energy, a series of simulations were conducted with σ equaling to 0.75, 0.65 and 0.55 J/m^2, respectively.

As shown in **Figure 4.9 (a)**, the discharge capacity decreases with the decreasing of the σ, along with the potential dip that correlated to nucleation process becoming shallow. This trend is consistent with the **Eq. 4.14**, which indicates that the energy barrier of nucleation can be lowered by reducing σ. Consequently, more nuclei are formed, leading to faster electrode passivation as evidenced by a smaller average size (**Figure 4.9 b-d**).

In addition, as presented in **Figure 4.10 a** and **b**, a potential oscillation is observed in the simulation where the surface energy equals to 0.55 J/m^2, accompanied by the oscillation of the nucleation rate and $LiO_{2(ip)}$ concentration. The contour map of the nucleation rate (v_{nu}) as function of the $LiO_{2(ip)}$ concentration and electrode potential is plotted in **Figure 4.10 c** and the color bar is in logarithm scale. By tracking the trajectory of the system in the map (red curve), it is found that the system swings between the nucleation zone and non-nucleation zone. Similar oscillation have been already reported in other chemical systems and explained in the framework of non-equilibrium thermodynamics.[178,179]

The interaction between an electrolyte and $LiO_{2(ip)}$, expressed in terms of solubility and consequently concentration of $LiO_{2(ip)}$ was seen as the only part of the discharge mechanism impacted by the nature of the electrolyte. However, our work revealed that this may not be the whole picture to demonstrate the influence of an electrolyte. The interaction between the electrolyte and Li_2O_2, expressed in terms of surface energy, also has significant consequence on the discharge mechanism with respect to the nucleation process.

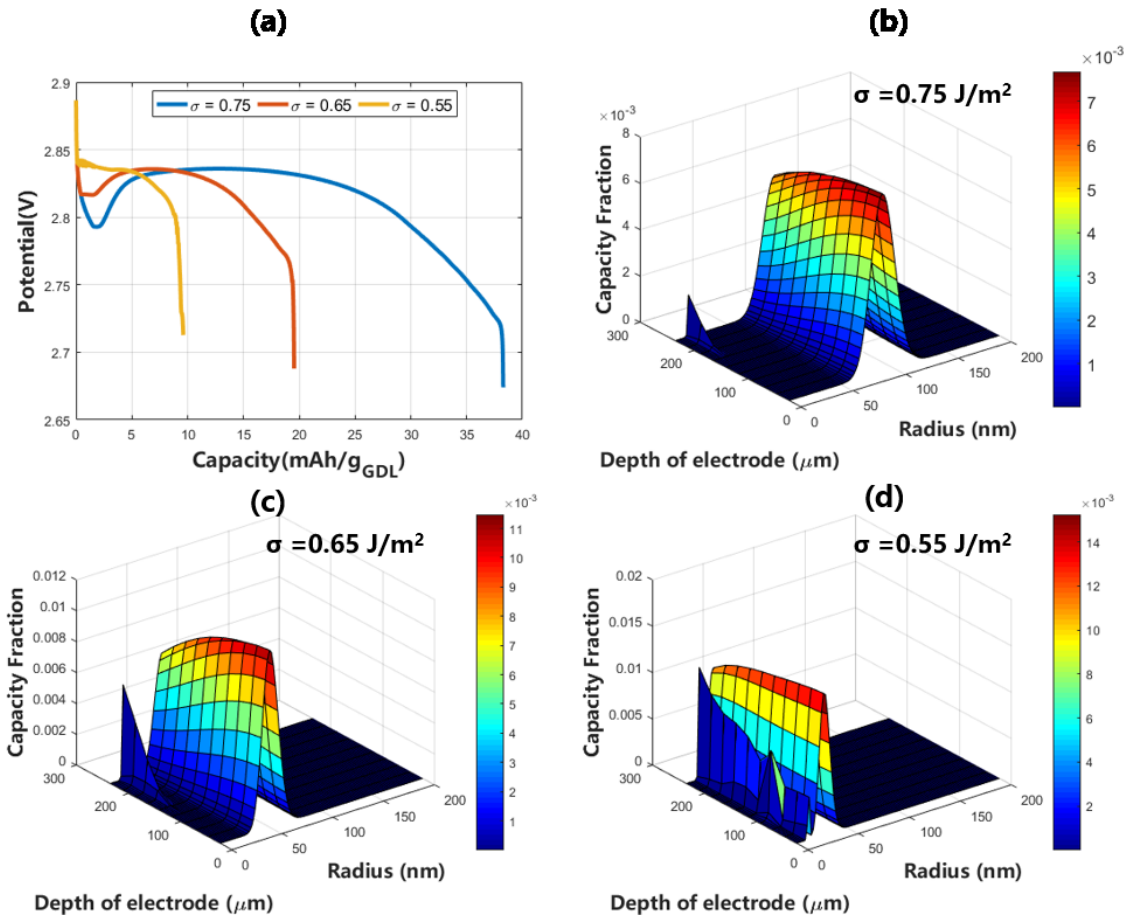

Figure 4.9: **(a)** Simulated discharge curves of Li-O_2 batteries with surface energies of Li_2O_2/electrolyte equaling to 0.75 (blue), 0.65 (red), 0.55 (yellow) J/m^2 and their final PSD **(b-d)**.

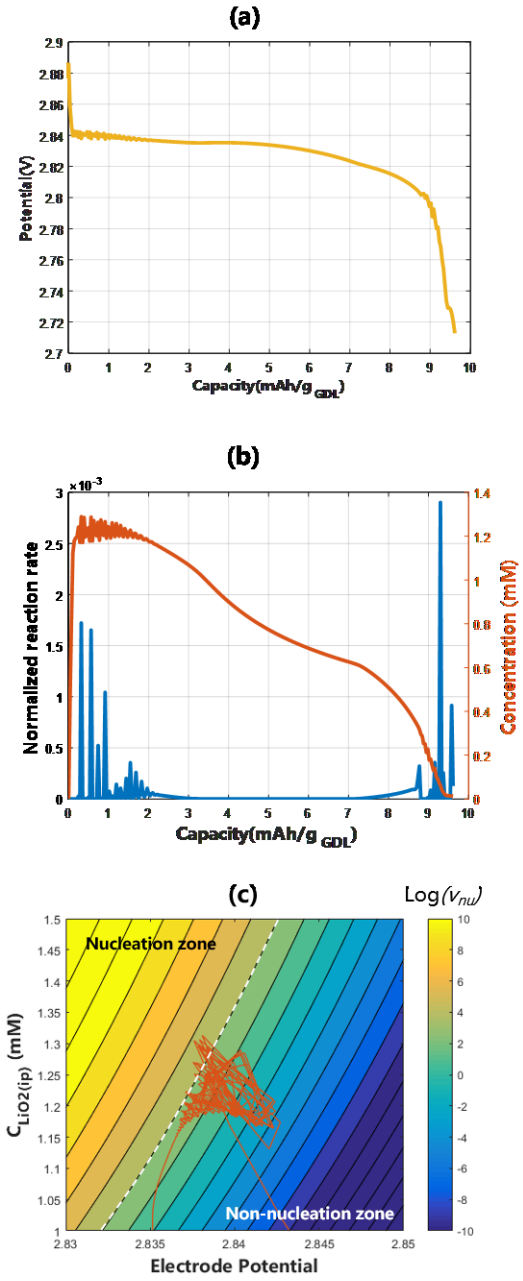

Figure 4.10: The simulated **(a)** potential variation and **(b)** the evolution of nucleation rate along with $LiO_{2(ip)}$ concentration during the discharge of a LOB with surface energy of Li_2O_2 in an electrolyte equaling to 0.55 J/mol. A potential oscillation as well as a concentration oscillation are observed during the nucleation processes ;**(c)** trajectory of the system (red line) in contour map of nucleation rate as function of $c_{LiO2(ip)}$ and electrode potential. The color bar is in logarithm scale and each color stripe in the color map represents 1 scale unit.

II.4 Impact of the electrode surface property

As heterogeneous nucleation is considered in the present model, the interaction between the substrate, *i.e.* the electrode surface in this case, and the Li_2O_2 nuclei also influences the nucleation process, which is reflected by the binding energy (E_b). A more negative value of the binding energy indicates a stronger binding between the Li_2O_2 and the electrode.

It is reported that the binding energy of Li_2O_2 on perfect graphene is around -0.26 eV, while on the defective site, it could decreased to -0.7 ~ -0.9 eV.[181] Thus, simulations are conducted with the present model with the binding energies ranging from -0.26 eV to -0.50 eV and -0.7 eV, obtaining discharge capacities of 38 to 24 and 12 mAh/g_{GDL}, respectively (**Figure 4.11a**). At the same time, the sizes of Li_2O_2 at the end of discharge are found to be smaller, implying that more Li_2O_2 are formed as resulted from a lower nucleation barrier. This suggests that strong binding between the Li_2O_2 and the electrode can enhance the Li_2O_2 nucleation.

Due to a stronger binding between the surface groups on carbon with Li_2O_2, the average binding energy of the carbon electrode decreases with the increase of the quantities of surface groups. In view of the nature of surface groups, which are usually -COOH and –OH groups, the O/C ratio on carbon surface could be a quantitative descriptor. By different surface treatments, Wong *et al.* obtained a series of carbon nanotubes with various O/C ratios. When using them as cathodes for LOBs, it is found that the discharge capacity decreases with the rising of the O/C ratio of the carbon nanotube (**Figure 4.11**),[84] which provide experimental supports for our simulation results.

Moreover, in a catalyst-loaded cathode, the binding energy of Li_2O_2 on the surface of catalyst (Pt, Au, TiO_2, etc.) is usually much lower than that on carbon surface,[182–184] leading to a preferential nucleation on the surface of the catalyst. Though the formed Li_2O_2 inactivates the catalyst fast by surface passivation, the pre-seeding effects delay the accumulation of $LiO_{2(ip)}$ at the initial stage of discharge and alleviate the side reactions due to the high activity of $LiO_{2(ip)}$, thus lead to the enhancement of the cycling life.

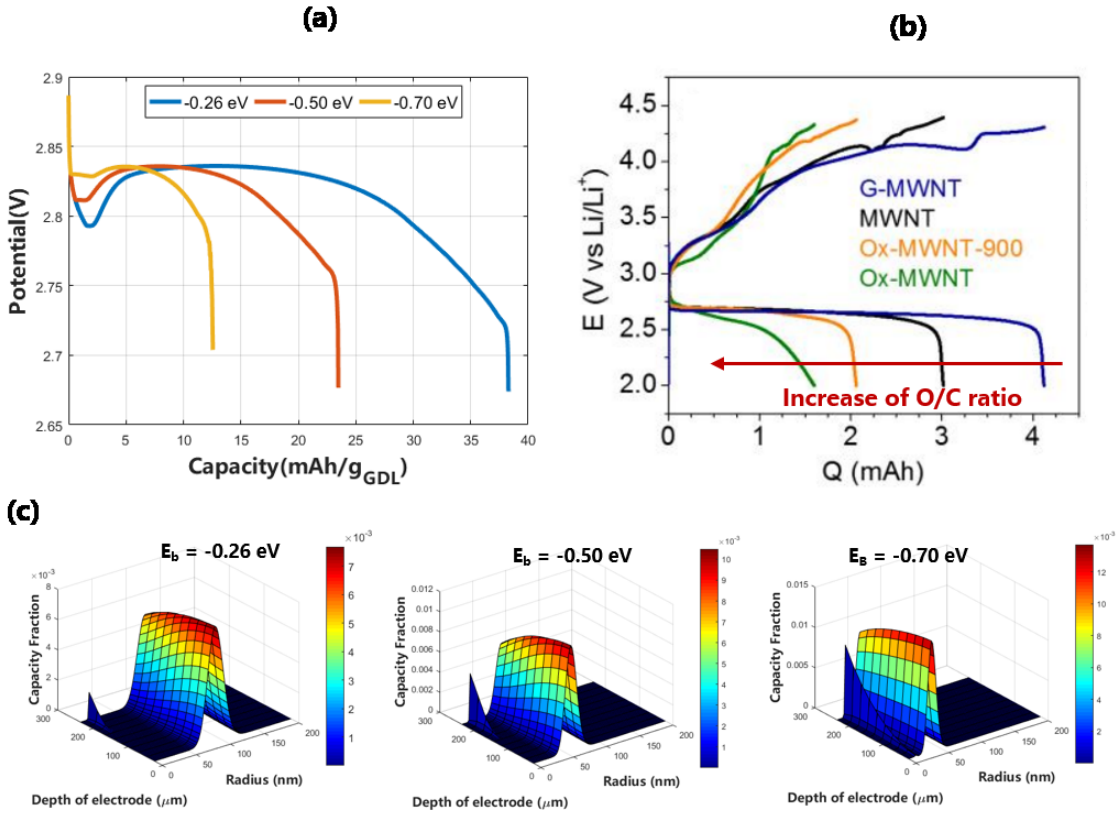

Figure 4.11: **(a)** Calculated discharge curves of Li-O_2 batteries with a binding energy of Li_2O_2/electrode equaling to -0.26 (blue), -0.50 (red), -0.70 (yellow) eV; **(b)** Calculated discharge and charge profiles of Li-O_2 batteries with electrodes of different O/C ratios, which implies different binding energies of Li_2O_2/C; **(c)** Calculated final PSDs corresponding to the discharge curves in **(a). (b)** is reprinted from Ref. 10.

III. Conclusions

In this chapter, we introduced a Li_2O_2 nucleation and growth model combining classical nucleation theory and detailed mathematical descriptions of the mass transport and the discharge mechanism in a LOB.

The simulation results reproduced the typical shape of voltage profiles in DMSO, which is characterized by the potential dip at the initial stage and "sudden" death at the last stage, which reflected the dynamic change of the $LiO_{2(ip)}$ concentration and the surface coverage of the electrode materials.

Moreover, the present model brings an innovative single cohesive theory to capture the Li-O_2 battery performance dependence on the discharge rate, electrolyte property and electrode surface property due to the nucleation process, providing deep insights into the discharge reaction mechanism of these devices.

Chapter 5 : Stochastic Modeling of Discharge Process in Li-O_2 Batteries

While the continuum approach succeeds in providing insights into the textural changes and reaction process of LOBs at the cell level, it may reach its limits when the target of investigation scales down to the mesoscopic level where the collision frequency of species with boundaries (*e.g.* pores, channel walls) is comparable to the intermolecular collision frequency. To describe the reaction kinetics and transport dynamics at the local level, discrete models with atomistic and molecular representation of the entities are required. However, microscopic modeling methods, such as Density Functional Theory (DFT) and Molecular Dynamics (MD), have limitation in terms of length scale and short time-span which are not applicable for mesoscale. In contrast, the so-called Monte Carlo (MC) method, due to its significant flexibility, can overcome the gap between the microscopic and the continuum modeling frameworks.[185]

There are two types of Monte Carlo methods: Metropolis Monte Carlo (MMC) method and kinetic Monte Carlo method (kMC). The former generates configurations according to the desired statistical mechanics distribution to study the equilibrium properties.[186] However, without description of physically relevant time, this method is not able to simulate the temporal evolution of a system. On the contrary, kMC can address kinetics with transition rates that depend on the energy barrier between the states.

In this Chapter, we report an innovative kMC method, as far as we know, applied for the first time to simulate the discharge process in the porous cathode of a LiO_2 cell. We apply this method to two particular problems: the effect of pore morphology and defects on the Li_2O_2 growth mechanisms. The content of this Chapter is based on the papers published in (i). G. Blanquer, Y. Yin, M. A. Quiroga, and A. A. Franco, *Journal of The Electrochemical Society*, **163**, A329–A337 (2016); (ii) Y. Yin, R. Zhao, Y. Deng, and A. A. Franco, *J. Phys. Chem. Lett*., **8**, 599–604 (2017).

I Brief Introduction to the Kinetic Monte Carlo Method

I.1 State-to-state transition and escape time

The kMC is a general approach for modeling the dynamic evolution of a system that can be decomposed into a collection of discrete events and their associated rate constants.[187] The evolution of the system is depicted as the state-transitions of the system. Here, the state of the system refers to the chemical composition of the system

and spatial distribution (configuration) of various species in the system. Let the state of the system before a transition be defined as state *i*. The system can escape from state *i* through different pathways which correspond to the occurrences of possible events such as displacement and reactions between species. For a possible escape pathway *j*, its probability per unit of time to escape from state *i* is characterized by its rate constant $k_{i,j}$, Therefore, the probability of the system to escape from state *i* within Δt is given by

$$P(\Delta t) = 1 - \exp(-k_{tot}\Delta t) \quad 5.1$$

where k_{tot} is the total escape rate by summing up the rates of all pathway as

$$k_{tot} = \sum_j k_{i,j} \quad 5.2$$

Then, the probability distribution of the escape process, which corresponds to the probability that the escape occurs at time *t*, is given by the time derivative of *P(t)*:

$$p(\Delta t) = k_{tot}\exp(-k_{tot}\Delta t) \quad 5.3$$

The average escape time t_{avg} is obtained by

$$\Delta t_{avg} = \int_0^\infty \Delta t p(\Delta t) dt = \frac{1}{k_{total}} \quad 5.4$$

Taking the weight of the probability distribution into consideration, the escape time Δt can be calculated as

$$\Delta t = -\frac{\ln(X_1)}{k_{tot}} \quad 5.5$$

where X_1 is a uniform random number in the interval (0,1]. As the escape time obtained from **Eq. 5.5** is generated from a random number and it may change even with the same k_{tot} value, this approach is called *variable step size method* (VSSM).

I.2 General procedure of kMC

The flow chart of the kMC algorithm is provided in **Figure 5.1** and the general procedures includes the following steps:[188]

a) Initialization

Setting the electrode and solution domain with desired geometry. Setting the initial state of the system as well as stop condition for the simulation.

b) Event selection and execution

Listing all the possible events under the current system state and counting the associated rates. Selecting an event from the above list to execute. The selection procedure is illustrated in **Figure 5.1**, where the rate corresponding to each is represented by a bar of proportional length. All the bars stacked together in a list represent the total rate of the system and a bar is randomly selected to choose an event. The selection process is numerically accomplished by generating a uniform random number X_2 on (0,1] and an event *j* is then chosen when it meets the following criteria:

$$\sum_{i=1}^{j} k_i < X_2 k_{tot} \leq \sum_{i=1}^{j+1} k_i \qquad 5.6$$

Since the probability of an event being chosen is weighted by the rate, the events with higher rate is more likely to take place.

c) Time and state updating

According to the execution of the chosen event from the previous step, the system is updated from state *i* to a new state *j*. At the same time, the clock of the system is advanced by a time increment referring to the escape time Δt in **Eq. 5.6**.

d) Continuation

If the stop conditions are fulfilled, the time loop stops. If not, the step b is repeated by considering the state *j* as the current state of the system.

With the time loop going on, the system transits from state to state. Concurrently, the dynamic properties of the system is therefore assessed.

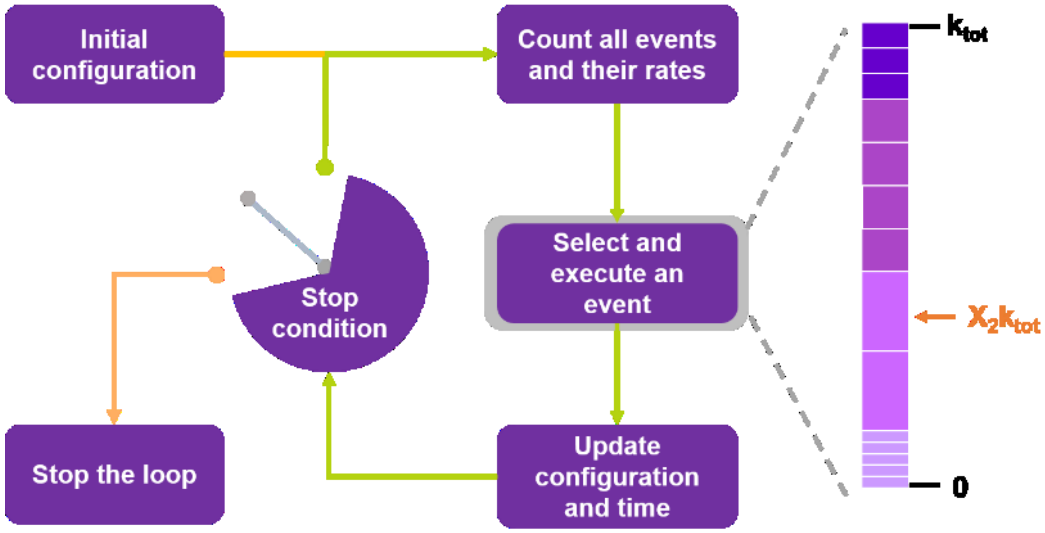

Figure 5.1: Flow chart of the general KMC procedures, where the green lines link the steps in the time loop. The left part of the figure illustrates the event selection process by generating an uniform random number X_2.

II General settings of the kMC model to simulate the discharge process in Li-O_2 batteries

On the basis of the general kMC procedure, we build relevant models to simulate the discharge process in the cathode of a LOB at local level. The system represents either a meso-pore or a nano-fiber in the electrode. In this Section, we present some general settings of our kMC model.

II.1 General assumptions

The general assumptions made in the model are summarized as follows,

a) The system is assumed to be in contact with a thermal reservoir of fixed temperature, thus the isothermal condition is applied here by neglecting the thermal fluctuation;

b) Parasitic reactions, such as electrolyte decomposition and carbon degradation, are not considered in the model;

c) The electrochemical double layer (EDL) effects are neglected;

d) The potential of the electrode does not change during the discharge process.

II.2 Species and system grid

The kMC model in our work is developed in three-dimensions (3D) and the system is initially divided into two domains, namely the solid domain and the liquid domain. The solid domain represents the electrode material, while the liquid domain represents the electrolyte where the soluble species (Li^+, O_2 and $LiO_{2(ip)}$) move around.

The systems can be designed with various geometries by constructing the solid and liquid domains differently, while maintaining the same partitioning into cubic grids. The length of the grid unit is 0.5 Å which corresponds to the size of solvated Li^+ ion in an organic solvent,[189] which illustrates the molecular resolution of the model.

The species taken into account explicitly in the model include Li^+, O_2, $LiO_{2(ip)}$, $LiO_{2(ad)}$ and Li_2O_2, while the solvent is considered implicitly in the background. The counter ions of the lithium salt are neglected. With the bond length around 121 pm, the O_2 molecule in the model is considered to occupy one grid unit like Li^+. The reaction between Li^+ and O_2 gives $LiO_{2(ip)}$, which occupies two joint grid units since it is considered as the combination of the solvated Li^+ and O_2^- ions. However, when the $LiO_{2(ip)}$ reacts further with Li^+, the resulting Li_2O_2 is again assumed to occupy only one grid unit due to the removal of the solvation shell. This assumption agrees with the cell parameter of the Li_2O_2 crystal structure.[190] As the $LiO_{2(ad)}$ is formed from partial desolvation of $LiO_{2(ip)}$ and is considered to have similar cell parameter than Li_2O_2 crystal, the size of a $LiO_{2(ad)}$ occupies also one grid unit.

II.3 Events in the model

Defining the possible events and their corresponding rates are the key issues in kMC simulations. For electrochemical system such as LOBs, there are two main types of events: displacements and reactions.

II.3. a Displacement Events

The displacement events refer to the motion of mobile species (Li^+, O_2 and $LiO_{2(ip)}$) in the liquid domain and there are two modes of displacements: translation and rotation. The translation mode represents the displacement when a mobile specie moves from one grid unit to an adjacent grid unit that is not occupied by other mobile species. The rates of translation (k_{jp}) are characterized by the jumping frequencies, which can be obtained from the Einstein equation of random walk as follows

$$k_{jp} = \frac{2D}{z^2} \quad 5.7$$

where z is the size of the grid unit and D is the diffusion coefficient given by the Stokes-Einstein equation,

$$D = \frac{k_b T}{6\pi\mu r} \quad 5.8$$

where z is the size of a grid unit, k_b is the Boltzmann constant, μ is the viscosity of the electrolyte and r is the hydrodynamic radius of the mobile species

By combining **Eq. 5.8** and **Eq. 5.9** we obtain

$$k_{jp} = \frac{kT}{3\pi\mu r z^2} \quad 5.9$$

For species occupying one grid unit, r equals the length of the grid unit. While for $LiO_{2(ip)}$ that occupies two grid units, the values of r equal to one or two grid units when the translation direction is parallel to the long or short edge of $LiO_{2(ip)}$, respectively.

Considering DMSO as the solvent, the calculated diffusion coefficients of all the mobile species that occupy one grid unit are at the magnitude of 10^{-10} m^2 s^{-1} which is similar to the values of Li^+ and O_2 reported in literature.[39,191] With the grid size of 0.5 nm in the model, the jumping frequency is set at the magnitude of 10^{10} s^{-1}.

The rotation mode of displacement is only applied to the $LiO_{2(ip)}$ due to the geometry of the molecules. One of the grid unit of $LiO_{2(ip)}$ rotates 90° with another grid unit of the same $LiO_{2(ip)}$ as axis. The rotating rate is estimated to be at the same magnitude as that of the jumping frequency, namely, 10^{10} s^{-1}.

A 2-D illustration of the displacement events is provided in **Figure 5.2**, where the black part refers to the electrode and white part refers to the electrolyte domain. Under the present system state, there is a Li^+ (yellow, position A) next to a $LiO_{2(ip)}$ (blue, position BC). Thus, the possible events for Li^+ are translations to D or E or F, and the translation rate is obtained from **Eq. 5.9** with r equaling z, marked as k_1. As for $LiO_{2(ip)}$, both translation and rotation are possible. If the $LiO_{2(ip)}$ translates along the BC direction to the new position GB or CJ, the corresponding rates also equal k_1; if the

translation is normal to the BC direction, arriving at the position HI, the rate of this process is then equal half of the k_1. $LiO_{2(ip)}$ can also move through rotation to the right side as Li^+ bloccks the rotation path at the left side. As a result, the new position of $LiO_{2(ip)}$ after the rotation is then either BH or CI.

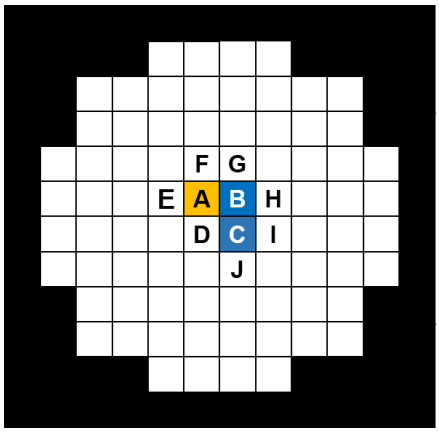

Figure 5.2: Illustration of the translation and rotation events in 2D with Li^+ (yellow) and $LiO_{2(ip)}$ (blue) as examples.

II.3. b Reaction Events

The reactions considered in our kMC model are listed as follows,

$$O_2 + Li^+ + e^- \longrightarrow LiO_{2(ip)} \quad 5.10$$

$$LiO_{2(ip)} + Li^+ + e^- \longrightarrow Li_2O_2 \quad 5.11$$

$$LiO_{2(ip)} \longrightarrow LiO_{2(ad)} \quad 5.12$$

$$LiO_{2(ad)} + Li^+ + e^- \longrightarrow Li_2O_2 \quad 5.13$$

$$2LiO_{2(ad)} \longrightarrow Li_2O_2 + O_2 \quad 5.14$$

The formation of $LiO_{2(ip)}$ occurs when a O_2 encounters a Li^+ and at least one of them is in contact to the electro-active material (**Eq. 5.10**), which refers to the electrode or Li_2O_2 within the critical tunneling distance. The formed $LiO_{2(ip)}$ can either be further reduced at the electro-active surface with the presence of a Li^+ to form Li_2O_2, or move into the solution. Due to the affinity between $LiO_{2(ip)}$ and Li_2O_2, the adsorption process

can take place if they come in contact with each other, leading to the formation of $LiO_{2(ad)}$. If still within the hole tunneling distance, the adsorbed $LiO_{2(ad)}$ can also react with a Li^+ to form Li_2O_2. Moreover, once two $LiO_{2(ad)}$ meet, the disproportionation reaction can happen, leading to formation Li_2O_2 and O_2.

For a better demonstration, a 2D illustration is presented in **Figure 5.3** to show how the reactions are performed in the kMC model. Under the as-shown system state, the possible reaction events are as follows:

a) since Li^+ (yellow, position C) is in contact with Li_2O_2 (orange, position G) which is within the tunneling distance, this Li^+ can react with the O_2 (purple, position A) to form a $LiO_{2(ip)}$ at position AC;

b) the Li^+ can also react with the $LiO_{2(ip)}$ (blue, position BF) to form a Li_2O_2 at position F or C that is in contact with electro-active surface and the relative probabilities to have Li_2O_2 formed at these two positions are weighted by their corresponding hole tunneling probability as explained later;

c) another possible reaction of Li^+ is to react with the adjacent $LiO_{2(ad)}$ (green, position D) to form a Li_2O_2 at position C or D with equal relative probability;

d) being in contact with a Li_2O_2 (orange, postion G), the $LiO_{2(ip)}$ at position BF can adsorb on the Li_2O_2 to form a $LiO_{2(ad)}$ at the position F;

e) disproportionation reaction can occur with the two $LiO_{2(ad)}$ (green, position D and E) that are in contact and one of them is randomly chosen to become a O_2 while the other is then transformed to a Li_2O_2.

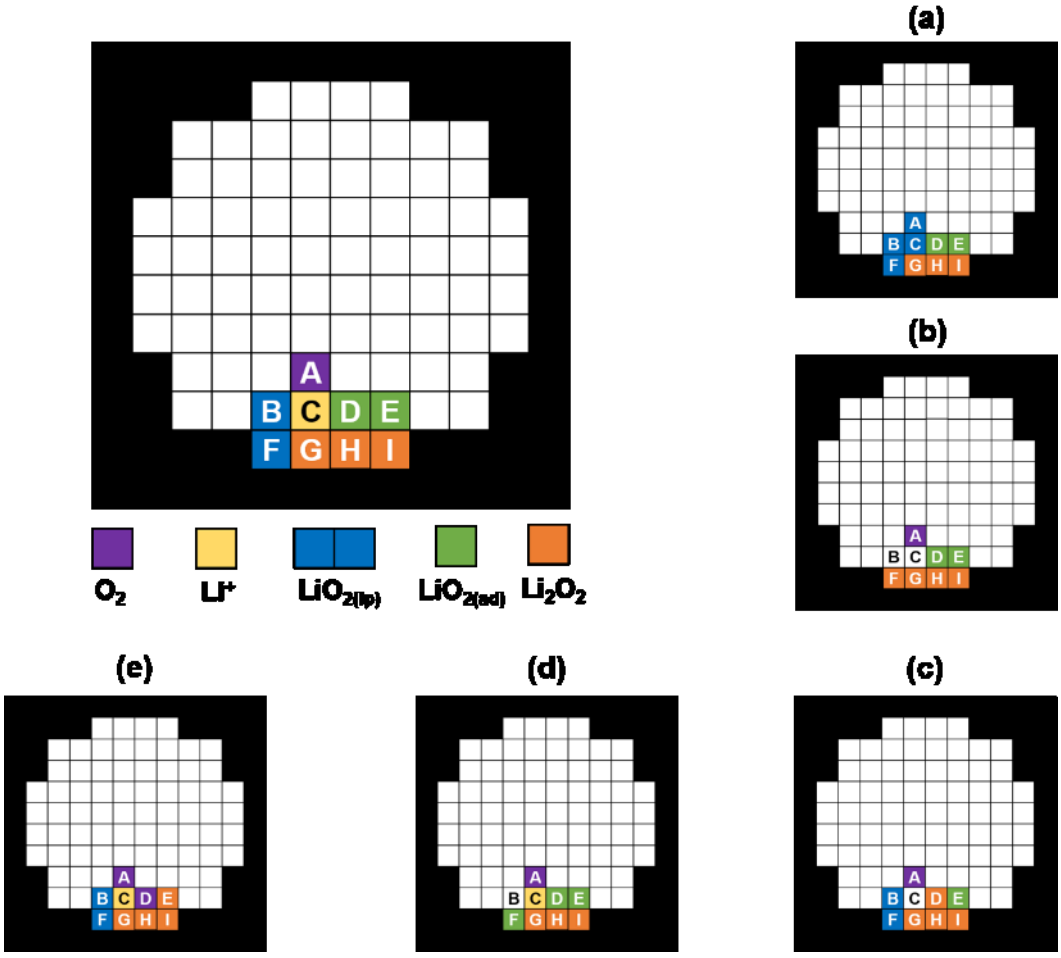

Figure 5.3: Illustration of the reaction events in 2D. **(a)-(e)** shows the new states of system resulting from the possible reaction events from the system states shown in the middle figure.

The rates of the electrochemical reactions (k_e) depend on the Li_2O_2 thickness as the charge transfer through hole tunneling becomes less efficient with the increasing Li_2O_2 thickness. This impact is captured in the kMC model through the tunneling probability P_t as follows

$$k_e = k_e^0 P_t \tag{5.15}$$

where k_e^0 is the reaction rate on the electrode surface; P_t is approximated with an error function similarly to the nucleation model described in **Chapter 4**, as follows:

$$P_t = \frac{1 - erf(\delta - d_m)}{2} \tag{5.16}$$

where δ is the thickness of the Li_2O_2 and d_m is the critical tunneling distance corresponding to the thickness of Li_2O_2 when the P_t drops to 0.5. The **Eq. 5.16** is directly applied in the fiber model; while in the pore model, it is further simplified to the following step function:

$$P_t = \begin{cases} 1, & \delta \leq 5\ nm \\ 0, & \delta > 5\ nm \end{cases} \tag{5.17}$$

One of the challenges in the kMC approach is to define the reaction rates. Though the heterogeneous rate constant k^o of the O_2 reduction in LOBs can be found in literature,[161] k^o is not imported as k_e^o in the present models due to the following reasons:

a) the two parameters have different physical meanings: k_e^o refers to the rate of charge transfer which is the reaction rate considering that the reactants are already present at the electro-active surface; while k^o represents the rate of the whole processes including the motion of the reactants toward the electro-active surface plus the charge transfer. As the reciprocal of the rate constants represents the average time for the occurrence of an event, the k^o and k_e^o can be linked by

$$\frac{1}{k^o} = \frac{1}{k_e^o} + \frac{1}{k_{cls}} \tag{5.18}$$

where k_{cls} is the frequency of an effective collision between reactants and electro-active surface. These effective collisions are captured intrinsically by the kMC algorithm.

b) the k^o reported in the literature is measured with glassy carbon electrodes, the surface property of which may differ from the electrode in Li-O_2 batteries. As the electrode surface property shows strong impacts on the formation kinetics of Li_2O_2,[85] the frequently reported assumptions that k_e^o can be estimated directly from k^o, may not be valid.

Due to the lack of available sources to determine the k_e^o, as one of the primary assumption, the baseline rates of all the electrochemical reactions are set to be the same as the diffusion rates. This assumption corresponds to a discharge process where the overall discharge rate is controlled by both reaction kinetics and diffusion. The rate constant of the adsorption process and disproportionation are also unavailable in literature; thus, they are also assumed to be similar as the diffusion process. With the kMC method being mesoscopic, it would be possible to incorporate rate values arising from lower scale computations, such as through DFT and/or MD approaches.

III. Pore model

Our first kMC model is built to simulate the discharge process inside a meso-pore in the porous cathode of a LOB (**Figure 5.4**).

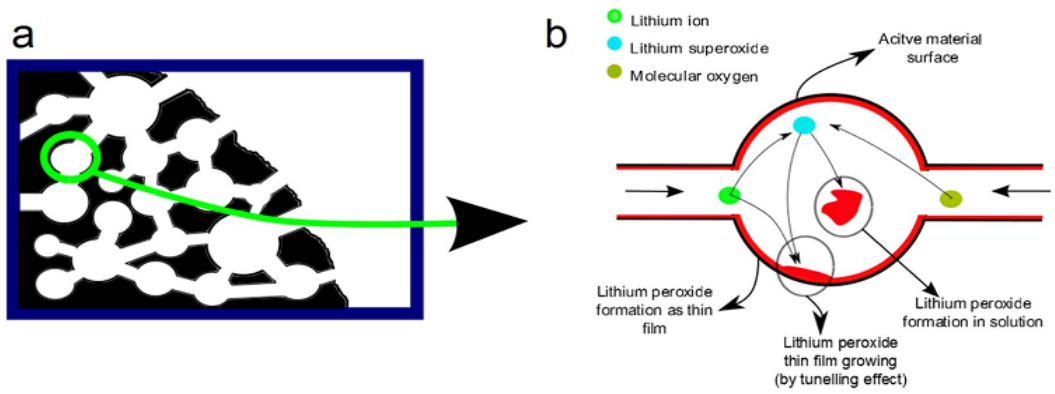

Figure 5.4: Schematics of **(a)** the nano-porous cathode structure and **(b)** different reactions considered in the present model.

III.1 Geometry of the system

In the pore model, the shape of the liquid domain is designed as a spherical pore with two cylindrical channels, while the wall of the pore and channels represents the electrode material (**5**).

One of the channels is assumed to link to an infinite O_2 reservoir, from where the O_2 molecules are injected into the system. The O_2 flux density (j_{O2}) through the channel-O_2 reservoir boundary is considered to be constant according to

$$j_{O_2} = c_{o_2}^{sat}\overline{v} \tag{5.19}$$

where $c_{o_2}^{sat}$ is the O_2 concentration in the reservoir equaling to the saturation concentration of O_2 in the solvent and $\overline{v}$ is the average molecular velocity of O_2, which can be calculated from

$$\overline{v} = k_{jm}z \tag{5.20}$$

Combining **Eqs. 5.7**, **5.19** and **5.20** gives

$$j_{O_2} = c_{o_2}^{sat}\frac{2D}{z} \tag{5.21}$$

The number of O_2 molecules entering the system is then obtained as follows,

$$N_{O_2} = j_{O_2}V_{bd}\,\Delta t_{inj} \tag{5.22}$$

where V_{bd} is the volume of solution domain at the channel-O_2 reservoir boundary, Δt_{inj} is the time interval from the O_2 injection. Here, N_{O_2} is said to increase with the accumulation of Δt_{inj}. Once N_{O_2} is larger than 1, O_2 molecules are put randomly at the boundary and Δt_{inj} is updated according to

$$\Delta t_{inj} = \Delta t_{inj}^{old} - \frac{1}{j_{O_2}V_{bd}} \tag{5.23}$$

The other channel is considered to link with the separator, where Li^+ ions enter the system. As the concentration of Li^+ (0.1-1 M) is much higher than the concentration

of O_2 (0-1.6 mM), the variation of Li^+ concentration is negligible during the discharge process in the system. Thus, in the model, once a Li^+ is consumed in the reaction, another Li^+ will be generated randomly at a unoccupied position.

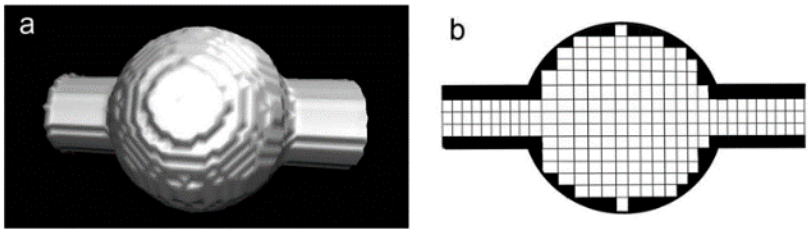

Figure 5.5: **(a)** 3D visualization of the simulated pore-channel system; **(b)** 2D projection of the simulated pore-channel system with the cut-view of the grid structure.

III.2 The reference case

The system with the pore radius of 10 nm and channel radius of 5 nm is chosen as the reference case to set the baseline for the further comparison. Five parallel simulations of the reference case were conducted with the parameters listed in **Table 5.3**. In spite of the stochastic property of the kMC method, good reproducibility of the parallel simulations was achieved with a relative disperse as small as 2% (**Figure 5.6**).

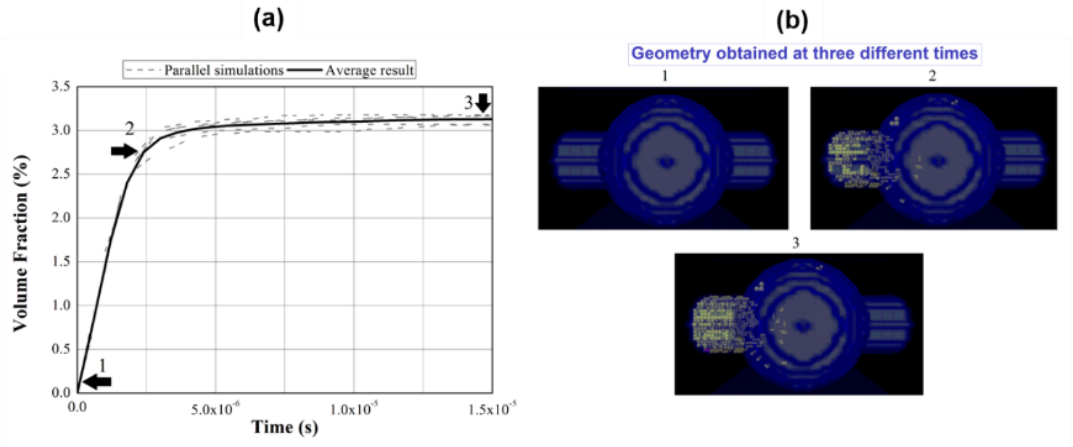

Figure 5.6: **(a)** Evolution of Li_2O_2 volume fraction (to the initial volume of solution domain) with time; **(b)** snapshots of the system configuration at initial '1', intermediate '2' and final '3' stages during the discharge process.

As shown in **Figure 5.6** (a), the growth of the Li_2O_2, as revealed by its volume fraction with respect to the initial volume of the liquid domain, can be divided into two stages: an initial slopy region implying a fast formation, followed by a quasi-plateau region indicating the slow and even stopped growth of Li_2O_2. According to the snapshot of the system configuration at different times during the discharge process (**Figure 5.6** (b)), the slopy region of the profile corresponds to the Li_2O_2 formation in the channel linking to the O_2 reservoir. Due to the low O_2 solubility in DMSO, the discharge reactions rely mainly on the O_2 that enters the system during discharge, thus Li_2O_2 was preferentially formed close to the O_2 inlet. As the channel radius in the reference case is similar to the passivation thickness, the channel was clogged when its surface was fully passivated by the Li_2O_2, leading to the blockage of O_2 transport pathway to the deeper parts of the system. Consequently, only 3% of the solution domain is filled by Li_2O_2 at the end of the discharge process and most of the electrode surface area remains unexploited.

Table 5.1: List of symbols and parameters in the simulation. The values of parameters correspond to the reference case.

Symbol	Parameters	Unit	Value
r_p	Pore radius	nm	10
r_c	Channel radius	nm	5
L_c	Channel length	nm	5
Z	Size of grid unit	nm	0.5
c_{Li^+}	Li^+ concentration	M	1
$c_{O_2}^{sat}$	Saturated concentration of O_2	M	1.6×10^{-3} [192]
μ	Dynamic viscosity of DMSO	cP	2.0 at 25 °C [193]
k_e^o	Charge transfer rate	s^{-1}	2×10^{10}
k_{jp}	Jumping frequency	s^{-1}	2×10^{10}
k_r	Rotation rate	s^{-1}	2×10^{10}
k_{ad}	Adsorption rate of $LiO_{2(ip)}$	s^{-1}	2×10^{10}
k_{disp}	Disproportionation rate	s^{-1}	
T	Temperature	K	300
R	Ideal gas constant	J $mol^{-1}J^{-1}$	8.314

III.3 Impact of system geometry

The impact of geometric parameters, *i.e.* pore and channel radius, were first investigated. Four systems with pore radius of 10 or 15 nm, combining channels with radius of 7.5 or 5 nm were studied and are discussed in this part.

The number of the Li_2O_2 species formed in each system as a function of time have been plotted in **Figure 5.7 a**. It is found that under the simulated conditions, the Li_2O_2 formation profiles from systems with the same channel radius were alike, indicating that the discharge performance was controlled by the channel radius. Regardless of the pore radius, there were always more Li_2O_2 formed in the system with channel radius of 10 nm than the systems with channel radius of 5 nm. This trend can be ascribed to the channel clogging, which has been confirmed by the final configurations of the systems (**Figure 5.7 b**). As explained with the reference case, the passivation of the channel surface was accompanied by the channel clogging for the system with channel radius of 5 nm. While for the systems with channel radius of 7.5 nm, the O_2 can still enter the pore after the channel surface were passivated by Li_2O_2, leading to the continuous formation of Li_2O_2, though with a smaller rate.

The slowing down of Li_2O_2 formation in the pore compared to the same process in the channel can be explained by two aspects. Firstly, the average time for O_2 arriving at the electro-active surface in the pore is longer than that in the channel. Secondly, the surface-to-volume ratio of the channel is larger than the pore, thus the collision frequency of active species with the electro-active surface is higher in the channel than in the pore. Thus, though the k_e^0 is the same, the k^o obtained in the channel and the pore are different.

The impacts of the collision frequency on the Li_2O_2 formation rates were also observed in the systems with different pore radius. As displayed in **Figure 5.7 c**, for the two systems with the same pore radius of 7.5 nm, Li_2O_2 were formed faster in the system with pore radius of 10 nm than in that of 15 nm. Therefore, reducing the pore radius can improve the overall rate of Li_2O_2 formation.

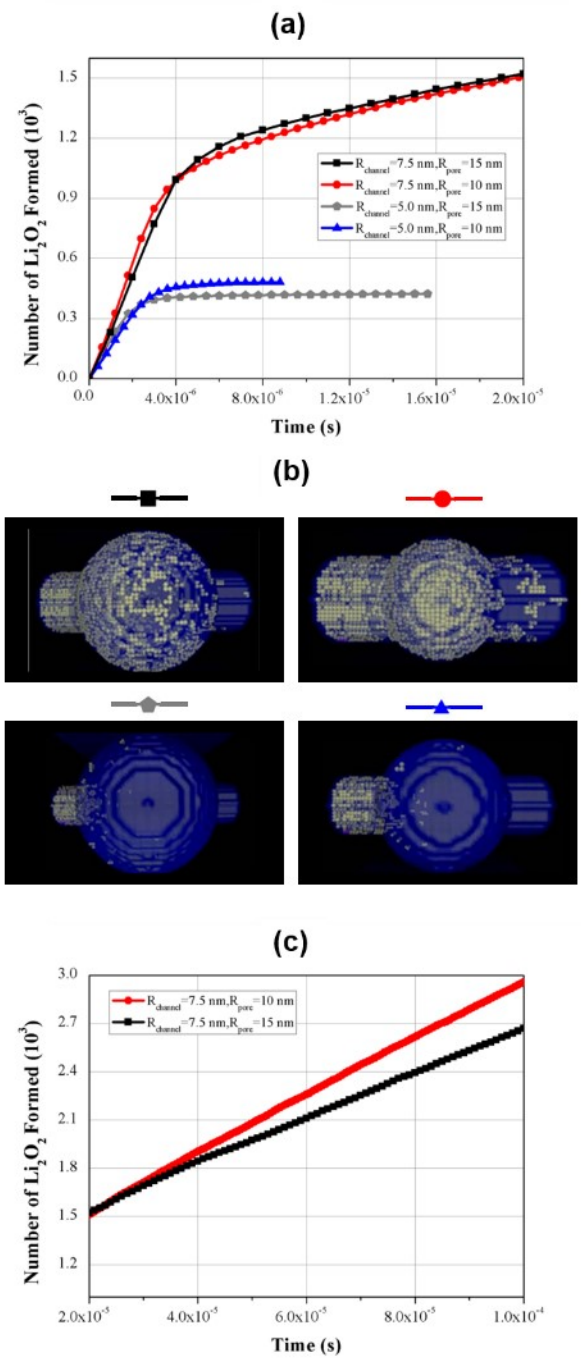

Figure 5.7: **(a)** The number of formed Li_2O_2 as a function of time in systems with various pore radius up to 20 μs; **(b)** the final configurations of these systems; **(c)** the evolution of the Li_2O_2 formation in systems with the channel radius of 7.5 nm from 20 to 100 μs.

III.4 Impact of O_2 and Li^+ concentrations

In this part, the impact of O_2 and Li^+ concentrations on the discharge process were investigated, where different trends were found according to the simulation results.

As presented in **Figure 5.8 a**, increasing the saturation concentration of O_2 in the solvent, led to a faster Li_2O_2 formation. The acceleration of the Li_2O_2 formation, as revealed by the shape of the slope of the volume fraction profile of Li_2O_2, is mainly due to the increase of the average number of O_2 in the system, leading to a higher collision frequency and hence enhancement of the overall reaction rate. Also, the amount of the Li_2O_2 formed during the discharge process was seen to increase with the rise of O_2 saturation concentration, though they are not in a proportional relation. The channel clogging is still the main limiting factor of the discharge process (**Figure 5.8 b**) and the improvement of Li_2O_2 volume fraction at high O_2 concentration is merely because there were slightly more O_2 entering the pore before the clogging at that condition.

On the contrary, more Li_2O_2 were formed in the system when the Li^+ concentration decreased from 1 to 0.1 M as shown in **Figure 5.9 a**. This concentration effect is in agreement with the experimental observation reported by Read *et al.*[39] They showed that with discharge capacity of LOB decreased with increasing Li^+ concentration. Moreover, the simulations showed that in the system with 1 M Li^+, the Li_2O_2 species formed were localized in the O_2 inlet channel; while with the decreasing Li^+ concentration, the Li_2O_2 can be found in the part farther from the O_2 reservoir. In the system with 0.1 M Li^+, there was Li_2O_2 formed even in the channel linking to the separator. These results indicated that the enhancement of Li_2O_2 formation directly resulted from the promotion of O_2 transport. Coexisting in the system, Li^+ ions were hindering the O_2 transport by steric effects. Thus lowering the Li^+ concentration can reduce the hindrance, improve the O_2 mobility, and delay the channel clogging to allow more O_2 to enter the pore.

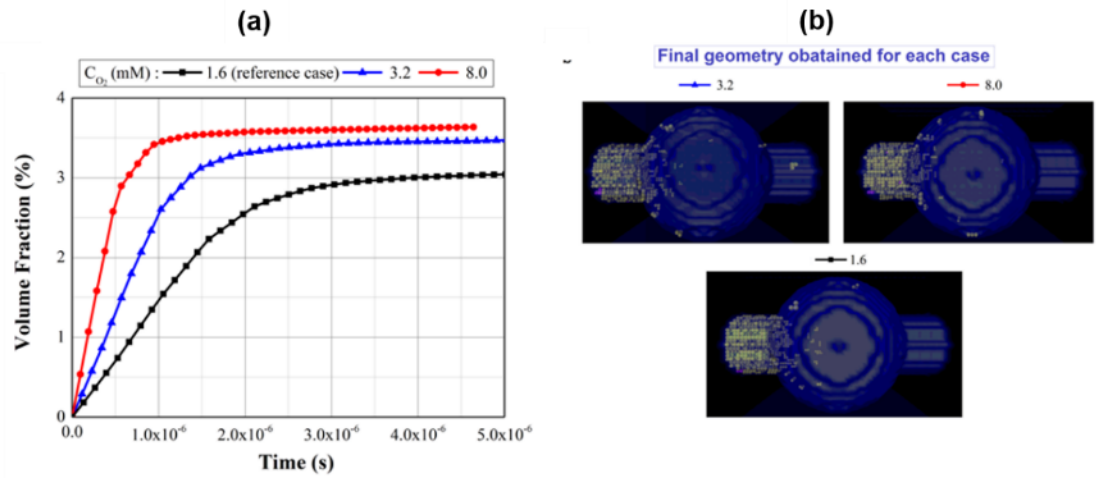

Figure 5.8: Simulation results of **(a)** Li_2O_2 formation in the systems with O_2 saturated concentration of 1.6 (black), 3.2 (blue) and 8.0 (red) mM, respectively, along with **(b)** their final configurations.

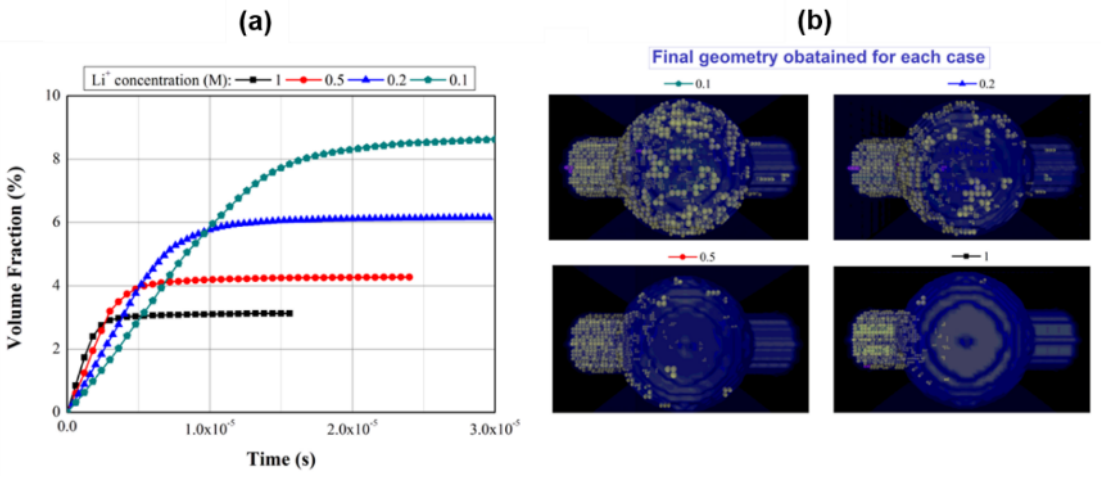

Figure 5.9: Simulation results of **(a)** Li_2O_2 formation in the systems with Li^+ concentration of 1.0 (black), 0.5 (red), 0.2 (blue) and 0.1 (green) M, respectively, along with **(b)** their final configurations.

III.5 Impact of overpotential

The relationship between the charge transfer rate and the overpotential is described by:

$$k_e^0 = k(\exp\left(-\frac{\alpha F\eta}{RT}\right) - \exp\left(\frac{(1-\alpha)F\eta}{RT}\right)) \quad 5.24$$

where the k is the prefactor. When the overpotenetial is not too small, the above equation can be simplified to the following form by neglecting the second exponetial term:

$$k_e^0 = k\exp\left(-\frac{\alpha F\eta}{RT}\right) \quad 5.25$$

As the overpotential is always negative during the discharge process of LOBs, larger is the absolute value of the overpotential, higher is the rate of the electrochemical reaction can reach. Therefore, the impact of the overpotential on the discharge process was studies by varying the value of k_e^0 on the basis of baseline value in the system.

With the decreasing charge transfer rate, the volume fraction profiles of Li_2O_2 were found to reach the plateau region farther away, indicating the delay of channel clogging (**Figure 5.10 a**) with more Li_2O_2 can be formed at the end. In all these three cases of simulations, most of the Li_2O_2 was formed from electrochemical reduction. The ratio of Li_2O_2 formed from disproportionation reaction also varied with the charge transfer rate, mainly due to the rare encounter with $LiO_{2(ad)}$. The volume fraction of Li_2O_2 formed via disproportionation showed a 9 fold increment, from 0.015% to 0.11%, when the charge transfer rate was increased by a factor of 10, while the overall Li_2O_2 formation only doubled from 3% to 6.5%. This obvious enhancement of disproportionation reaction is attributed to the extension of the lifetime of $LiO_{2(ip)}$ and $LiO_{2(ad)}$, which refers to the time between their formation and consumption. As the charge transfer rate decreases, the average lifetime of electro-active species increases, and thus the probability for two $LiO_{2(ad)}$ species meeting each other increases, leading to a higher chance to have disproportionation reaction. Similarly, the lowering of charge transfer rate also leads to a longer lifetime of O_2. As a result, more O_2 enters into the pore before the channel clogging, ending up with a more homogeneous distribution of Li_2O_2 (**Figure 5.10 c**).

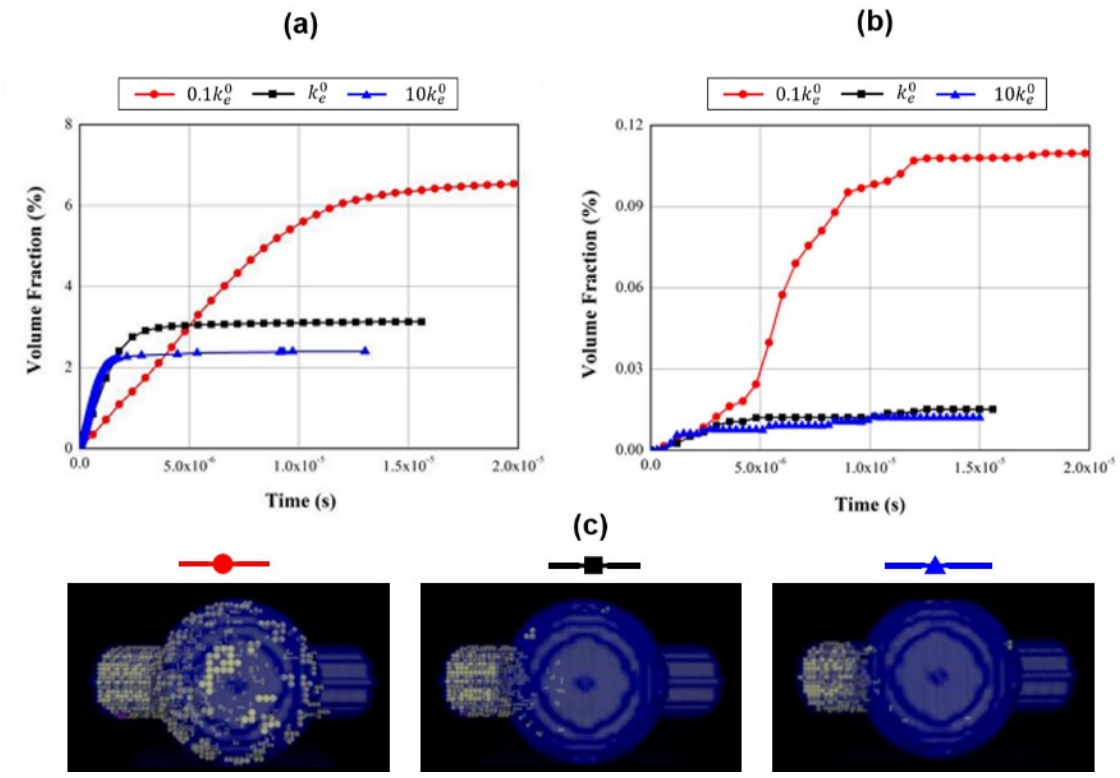

Figure 5.10: Simulation results of **(a)** overall Li_2O_2 formation and **(b)** Li_2O_2 formed from disproportionation reaction in the systems with the rates of electrochemical reactions equaling to 0.1 $\boldsymbol{k_e^0}$ (red), $\boldsymbol{k_e^0}$ (black) and 10 $\boldsymbol{k_e^0}$ (blue), respectively, along with **(c)** their final configurations.

IV. Collective motion of Li^+

As the concentration of Li^+ used in the model is 2~3 orders of magnitude larger than the saturated concentration of O_2, the number of the Li^+ ions is much larger than the number of O_2 molecules in the system. Thus, the displacement of the Li^+ is the dominant event, impacting most of the simulation time. However, due to the abundance of Li^+ in the system, the Li^+ transport is not the limiting factor and is less relevant to the discharge process compared to O_2 transport and reaction events. To improve the simulation efficiency, a shuffling algorithm has been developed to describe the displacement of Li^+ in the system by randomly redistributing all the Li^+ in the system at a certain frequency. As all the Li^+ ions in the system are involved in the shuffling approach, it is also called as the collective motion.

During the time between two shufflings, the Li^+ is considered as immobile and its displacement is no longer considered in the VSSM time loop. Hence, the average size of the time step obtained from the VSSM, which is reversely proportional to the

total rates, becomes large. As a result, less iterations are required to reach the same simulated time than in the conventional kMC algorithm and the computational time is thus reduced.

The key in the collective motion algorithm is to determine the time interval between two shuffles which can be obtained with the following steps:

a) The first step is to calculate the overlapping ratio of Li^+ position between two random fillings of the system. To ensure the statistical significance of the results, a large number of parallel simulations are carried out;

b) At the meantime, conventional kMC simulations of the system are also conducted with individual Li^+ displacement as the only event. Taking the initial states of the system as the reference, the evolution of the Li^+ position overlapping ratio is recorded at each time step. With the simulations going on, more and more Li^+ move away from their initial position and the overlapping ratio drops continuously;

c) Once the Li^+ overlapping ratio from kMC simulation reaches the same value as the random fillings, the corresponding simulated time is then defined as the shuffling time interval.

As a demonstration, let's assume the target system with a cylindrical solution domain, the wall of which represents the electrode. The cylinder has a length of 40 nm and the Li^+ concentration in the system is 1 M. The overlapping ratio of Li^+ position between two random fillings of systems with different diameters are summarized in **Table 5.2**. All the results are the average values from 500 parallel simulations and the overlapping ratios in these cases are between 7% and 8.5%.

Taking the cylinder with diameter of 40 nm as an example, the evolution of the Li^+ position overlapping ratio is displayed in **Figure 5.11**. As the kMC simulation proceeds, more and more Li^+ move away from their initial positions, leading to the continuous dropping of the overlapping ratio in the system. According to **Table 5.2**, the overlapping ratio for the system with cylinder of diameter of 40 μm is 8.51. The same value in **Figure 5.11** corresponds to the simulation time of 6.61 s, which is thus considered as the shuffling time interval for the system. Similar approach is applied to

system with other cylinder sizes respectively and the obtained shuffling time intervals for each system are shown in **Table 5.3.**

Table 5.2: The overlapping ratios between two random fillings of the cylindrical systems with various diameters. The presenting result for each system is averaged from 500 trials.

Diameter (nm)	10	20	30	40	50	60
Overlapping ratio	7.73%	7.17%	7.81%	8.51%	8.30%	8.47%
Standard deviation	0.60%	0.30%	0.21%	0.15%	0.14%	0.13%

Table 5.3: The shuffling time interval for the cylindrical systems with various diameters. The Li^+ concentration in the kMC simulation is 1 M.

Diameter (nm)	10	20	30	40	50	60
Shuffling time (ns)	6.049	6.427	6.549	6.611	6.434	6.587
Standard deviation (ns)	0.268	0.131	0.091	0.053	0.052	0.045

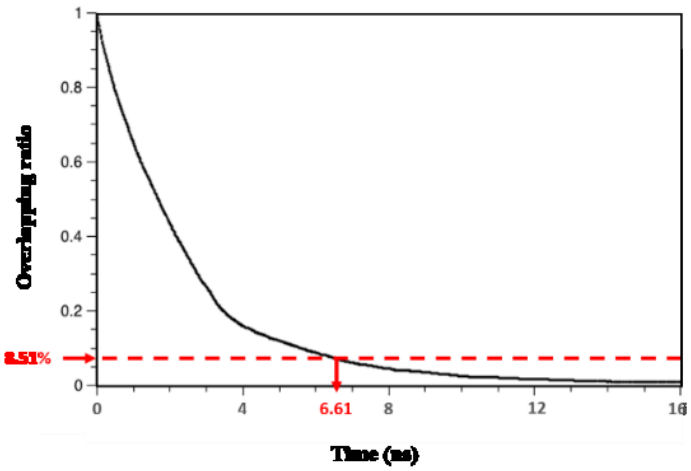

Figure 5.11: The evolution of Li^+ overlapping ration in the cylindrical system with diameter of 40 nm. The red dash line shows the overlapping ratio corresponding to the two random fillings of the system.

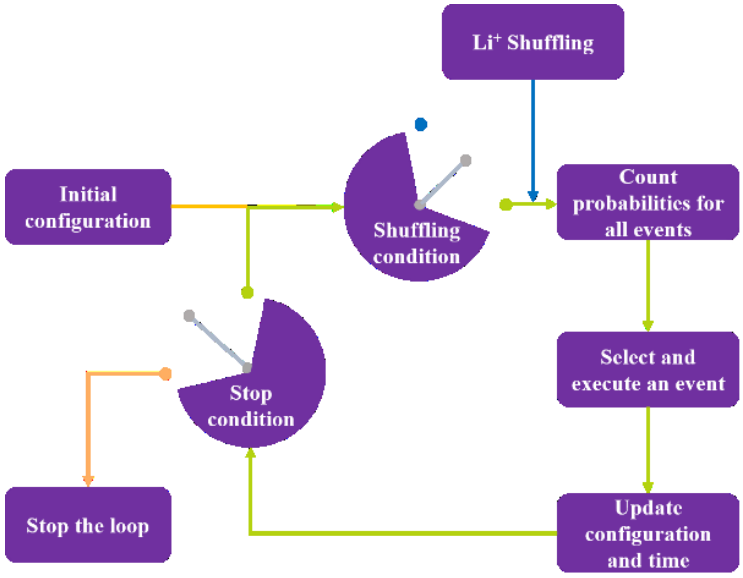

Figure 5.12:. Flowchart of kMC algorithm incorporating the shuffling.

The cross-checking between the Li^+ collective motion approach and conventional approach has been performed based on the system with diameter of 20 nm. It is shown that the wall time of the simulation can be reduced from 240 h to 5 min when the Li^+ collective motion was applied.

V. Fiber model

In the pore model, the discharge process and the Li_2O_2 formation are mainly limited by the O_2 transport due to the channel clogging. Thus, in order to bypass this limitation and put our focus on the growth of Li_2O_2, a new model is built by considering a cylindrical electrode domain, which refers to a carbon nanofiber (CNF) embedded in a rectangular cell filled with electrolyte. The diameter and the length of the fiber are 8 and 40 nm, while the dimensions of the cell are 30, 30 and 40 nm in height, depth and length, respectively.

The discharge process considered in the fiber model is almost same as in the pore model except for the disproportionation reaction, which is overlooked in the fiber model due to its rareness. Moreover, the collective motion of Li^+ is applied here to speed up the simulation.

V.1 Impact of the catalyst

In many of the experimental investigations, nano-particles of catalysts are loaded on the carbon materials to be employed as the cathode of LOBs. The nature of the catalysts can be either noble metal[113,194] or metal oxides,[78,195] which help to accelerate the electrochemical reactions. The corresponding catalyst-loaded system is set up with the fiber model by assuming that the catalysts nanoparticles are randomly distributed on the surface of CNF. The nature of catalysts in the model is arbitrary but their impacts are considered through attributing a higher rate of electrochemical reaction at the catalyst surface. Though still in doubt, the side reactions triggered by the loading of catalysts are assumed to be negligible at this stage.

Simulations of CNF system with or without catalysts were carried out and the results are provided in **Figure 5.13**. The evolution of Li_2O_2 formation in both systems are captured by the snapshots of the corresponding system at different simulated time. It is found that the Li_2O_2 in catalyst-free system is grown in a layer-by-layer manner (**Figure 5.13 a**), starting from the electrode surface. As the charge transfer rate is identical on the entire surface of CNF, the formation of the Li_2O_2 is homogeneous on the electrode. In contrast, the Li_2O_2 formation on the cat-CNF is inhomogeneous at the initial stage (**Figure 5.13 c**). Due to the higher reaction kinetics on the catalyst surface, Li_2O_2 grows faster around the catalysts and form separated islands, which keep growing and finally coalesce together. In this case, Li_2O_2 is prone to form first at the outset layer where there was a higher probability to capture O_2 and Li^+.

The final appearances of the discharge thin film formed in both systems were similar to an isotropic cylinder, yet the compactness of both are quite different. In the following we have employed a function *g(r)* to evaluate the compactness of the film according to:

$$g(r) = \frac{N(r)}{N^o(r)} \qquad 5.26$$

where *N(r)* is the number of particles that are at a distance from the fiber surface between *r* and *r*+*dr* (*dr* = 0.5 nm) from the fiber, $N^o(r)$ is the number of grid units that are away from the fiber within a distance of *r*, and *g(r)* lies within the interval [0,1]. When *g(r)* equals 1, the layer is fully compact, while if *g(r)* is equal to 0, the layer is empty. For the fully discharged CNF with a total length of 40 nm, we checked the cross-

sections at lengths of 5, 20 and 35 nm (plane 1, plane 2, and plane 3), which are presented in **Figure 5.13** b and d together with the corresponding RDF analysis.

It is found that the Li_2O_2 thin film formed on the CNF is dense with the compactness through the entire thickness maintaining above 0.95, which indicates a high degree of ordering. On the bare surface, the charge transfer rate (k_e^0) is similar to the diffusion rate (k_{jp}); however, with the increase of Li_2O_2 thin film thickness, k_e^0 decreased as described in **Eq. 5.16**, and it is gradually overwhelmed by the diffusion rates. Thus, the Li_2O_2 formation in this case is more controlled by the charge transfer rate and electrochemical reactions hardly take place until reaching the thinnest part of the film, where the charge transfer rate is the highest, leading to a layer-by-layer growth.

However, the Li_2O_2 thin film formed on the cat-CNF shows a lack of ordering evidenced by an average compactness of around 0.4. In some part, the compactness even dropped to 0.1. The disordering of Li_2O_2 is in agreement with the experimental findings by Yimaz *et al*. and Yang *et al.*, which shows that the Li_2O_2 formed with the presence of catalysts is noncrystalline.[118,196] This difference in the ordering degrees compared to CNF can be attributed to the competition between the diffusion and the reaction kinetics of the active species. Owing to the higher rate of charge transfer than the diffusion, the active species react immediately after arriving at the reaction interface (Li_2O_2/electrolyte interface) which is grounded on the catalyst. Thus, the Li_2O_2 formation in this case is more controlled by the transport of active species and the outer part of the thin film grows faster than the inner part because of higher accessibility to the active species. More than that, the formation of the outer part shows negative impacts on the growth of the inner part as it hinders and even blocks the mass transport towards the inner part, bringing about a low compactness in the middle part of the thin film.

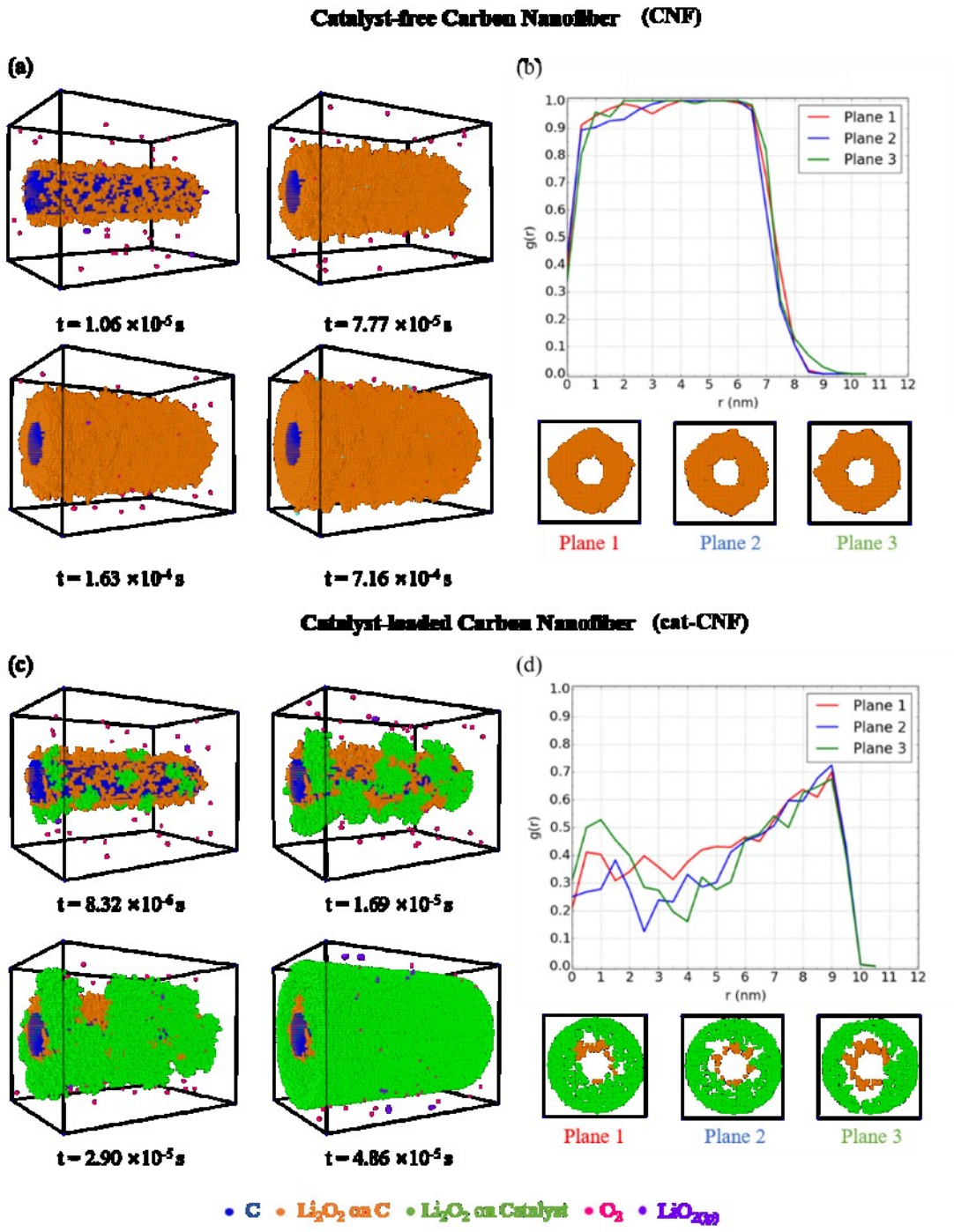

Figure 5.13: The evolution of the Li_2O_2 thin film formation on **(a)** CNF and **(c)** cat-CNF with the RDF analysis of the fully discharged **(b)** CNF and **(d)** cat-CNF. The diameter and the length of the fiber are 8 nm and 40 nm, the dimensions of the cell are 30×30×40 nm in height, depth

and length and the diffusion coefficient of $LiO_{2(ip)}$ is 1×10^{-10} m^2 s^{-1}. The Planes 1, 2 and 3 correspond to the intersection of the nanofiber at 10, 40 and 70 nm, respectively.

V.2 Impact of $LiO_{2(ip)}$ diffusion rate

Two more simulations were carried out to provide more insights into the influences of the diffusion rate and charge transfer rate on the compactness of Li_2O_2 thin film.

The first simulation simulates the formation of Li_2O_2 on a catalyst-free CNF when the charge transfer rate was increased by a magnitude than the baseline value, which can be resulted from the raise of the overpotential in cathode. As displayed in **Figure 5.14**, Li_2O_2 formed in this case is not as compact as in **Figure 5.13 b**. Moreover, the compactness of the Li_2O_2 increases from 0.2 to 0.9 along the direction of Li_2O_2 growth and the overall compactness is around 0.6. The drop of the film compactness indicates the decrease in the selectivity of the reaction site. When the reactants arrive at the surface of Li_2O_2 that is relatively far away from the carbon surface, they are still more likely to react here instead of diffusing away to have reaction at a position that is closer to the carbon fiber, as the charge transfer rate is still larger than the diffusion rate at this position.

The other simulation is conducted with the catalyst-loaded CNF and the diffusion rate of $LiO_{2(ip)}$ in this case is set to be 10 times of the baseline value. As displayed in **Figure 5.15,** the overall compactness of formed Li_2O_2 in the current case is similar to the baseline case in **Figure 5.13 d**. However, a more homogenous Li_2O_2 film along the thickness is found in the current case. This is due to the fact that with the increase of diffusion rate, more $LiO_{2(ip)}$ that is formed at the outer part can diffuse to the inner part and further reacts to form Li_2O_2 there, improving the homogeneity of the Li_2O_2 thin film.

The above cases confirmed that the compactness of Li_2O_2 formed is closely linked to the selectivity of reaction site, which is determined by the competition between the rates of diffusion and charge transfer. When the diffusion rate is much higher than the charge transfer rate, the reactants would select position of highest reaction rate to react, leading to the formation of compact film; on the other hand, if the charge transfer rate is higher, the reactants would react at any possible site rather than move away, resulting in a less ordered Li_2O_2.

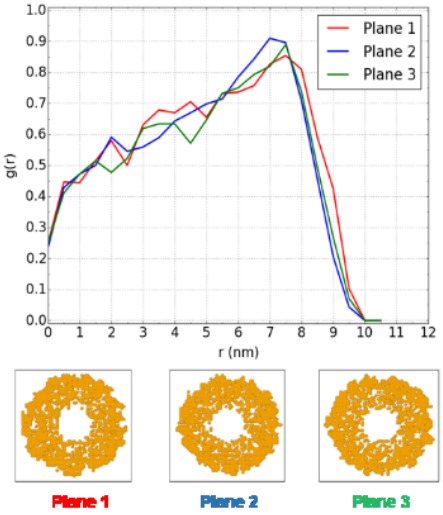

Figure 5.14: The RDF analysis of the Li_2O_2 formed on a catalyst-free CNF with the charge transfer rate is higher than the baseline value by a magnitude.

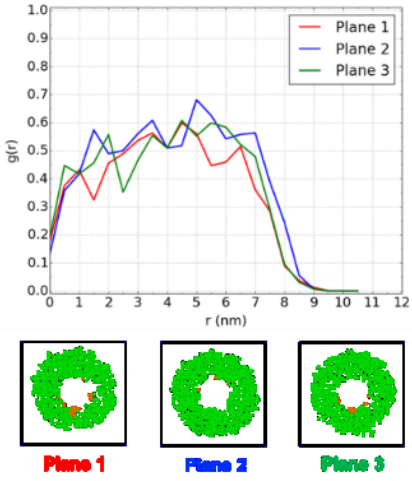

Figure 5.15: The RDF analysis of the Li_2O_2 formed on a catalyst-loaded CNF with the diffusion rate of $LiO_{2(ip)}$ is higher than the baseline value by a magnitude.

VI . Conclusions

In this chapter, we introduced our stochastic models based on the kMC method to study the discharge process of LOBs. The local environment of the cathode has been captured in the model, as the simulated system represents either a meso-pore of the porous electrode or a carbon fiber of electrodes.

The results from the pore models highlight the double-edged effects of the pore/channel size on the discharge performance. On one hand, smaller pores can increase the overall reaction rate by enhancing the collision between the reactants and electrode surface due to a higher surface-to-volume ratio; on the other hand, smaller pores can hinder the mass transport due to pore clogging. Thus, both impacts should be balanced in the design of electrode textures. Moreover, the pore model provides insights into the experimental observation that discharge capacity decreases with the increase of Li^+ concentration, which is attributed to the lowering of O_2 mobility caused by the steric hindrance of Li^+.

The investigations with the fiber model focus on the formation of Li_2O_2 on the CNF electrode. Originating from distinct charge transfer rates, different types of Li_2O_2 growth were observed in the simulation of catalyst-free and catalyst-loaded system, leading to the variation in the ordering of the formed Li_2O_2. As the charge potential is correlated to the ordering of Li_2O_2, the simulation results provided an alternative explanation for the potential lowering mechanism of the catalysts.

As far as we know, this model is the first 3D kMC model of LOBs reported in literature. After the proof-of-concept, the same approach was expanded at LRCS to other electrochemical systems, such as Li-S batteries and Redox-flow batteries.[197,198] Moreover, with the outputs from the kMC model, a virtual reality (VR) game has been developed for the teaching purpose. The structural evolution of the pore was visualized to demonstrate the O_2 transport limitation and electrode passivation during the discharge of a Li-O_2 cell; this was the subject of another article, with myself as co-author, and currently submitted as: Yin, Y.; Zhao, R.; Ciger, J.; Lelong, R.; Franco, A. A, *J. Chem. Educ*, 2017, submitted.

Chapter 6 : Experimental Setup and Characterization of Li-O_2 Batteries

In parallel to the modeling, model experiments have been performed under conditions close to the ones assumed in the models, for the purpose of model validation. Moreover, due to the lack of available setup at LRCS to cycle the Li-O_2 cell in pure O_2, a new setup has been developed during this thesis.

I Materials and Method

I.1 Preparation of the electrolyte

The electrolyte was prepared by dissolving lithium perchlorate ($LiClO_4$, battery grade, Aldrich) in anhydrous dimethyl sulfoxide (DMSO, 99.9 %, Sigma-Aldrich). The DMSO solvent was dried with activated molecular sieve (3 Å, Sigma-Aldrich) for 48 h to obtain a water content < 20 ppm as measured by using the Karl Fischer method. The $LiClO_4$ salt was dried under vacuum overnight at 120 °C, then transferred into argon filled glovebox without exposure to ambient air. The solvent and salt were mixed together with targeted molarity inside the glovebox.

I.2 Preparation of the negative electrode

Li metal discs with diameter of 9 mm and thicknesses of 0.7 mm were used as negative electrodes in the characterized. In prior to the cell assembling, the surface of the Li discs was scratched to remove the passivation layer.

It is reported that Li metal is not stable in DMSO upon cycling due to the failure of forming a stable solid electrolyte interphase (SEI) layer on the metal surface. As a result, Li metal continuously reacts with DMSO until being fully oxidized.[199] However, this effect can be neglected in our experiments where Li was in large excess. As we focused only on the first discharge-recharge cycle, the overall reaction time is not that long and at the end of the cycle, metallic Li can be still found in the cell. So, it is reasonable to consider that the impact of DMSO on Li does not affect significantly our experimental results.

I.3 Preparation of the positive electrode

Two types of positive electrodes were used in our experiments: porous carbon composite electrodes and gas diffusion layer (GDL) electrodes.

I.3.a Carbon composite electrodes

The carbon composite electrodes were prepared from slurries consisting of 90 wt% Carbon Super P (Csp, Timcal Ltd) with 10 wt% binder mixed in organic solvents. The binder was either polyvinylidene difluoride (PVdF, Kynar®, Arkema) or polytetrafluoroethylene (PTFE, 60 wt% dispersion in water, Sigma Aldric), for which the organic solvents were correspondingly N-Methyl-2-pyrrolidone (NMP, Sigma Aldrich) or isopropanol (>99.9%, Sigma Aldrich). Then, the slurries were loaded on stainless steel (SS) meshes (ϕ11 mm, AISI 316, 100 mesh, Alfa Aesar) by drop-coating with a glass pipette or spray-coating with an air-sprayer (Badge model 360). The as-prepared electrodes were firstly dried on a heating plate at 100 °C in ambient air, then further dried under vacuum in a Büchi oven at 120 °C overnight and transferred to an argon-filled glovebox without any air exposure. Before vacuum drying, PTFE-based electrodes were washed with ethanol/water (3:1, v:v) mixture to remove the surfactant from the PTFE suspension.

I.3.b GDL electrodes

The GDL disc electrodes were cut from a large GDL sheet (H23, Freudenberg) using a steel punch with a diameter of 11 mm. Due to its good electronical conductivity (in-plane resistance: 4.5 mΩ cm^2, from provider), GDL electrodes can be employed without any further treatment except vacuum drying at 120 °C overnight.

II. Battery testing and post mortem analysis

II.1 Swagelok cells assembling

As Swagelok®-type (SW) cells can be easily disassembled to recover the cycled electrodes, they were used in this thesis to perform the electrochemical characterizations.

The SW cells were assembled inside an argon-filled glove box containing less than 5 ppm O_2 and 1 ppm H_2O. **Figure 6.1** displays the architecture of the SW cell, where the Li metal/separator/positive electrode sandwich is placed between two stainless-steel cylinders. The bottom SS cylinder is solid, holding the Li metal disc. Then, two pieces of separators (Whatman® glass fiber, Ø14 mm) soaked with electrolyte and a positive electrode were successively stacked on the Li-metal disc. When the carbon composite electrode is used as positive electrode, a disc of SS mesh was used as current collector, which is not necessary for GDL electrodes. Above that

there is the top cylinder, which is designed to be hollowed to allow O_2 access to the positive electrode.

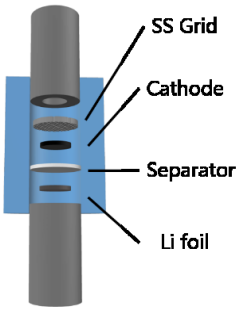

Figure 6.1: Schematic representation of SW cell.

II.2 O_2 filling

At the start of this thesis, there was no available LOB testing setup in LRCS except for a handcrafted glass tube, which cost more than 2000 euros. Then, a new hardware for SW cycling was developed with the help of Jean-Bernard Leriche, a technician at LRCS (**Figure 6.2**). These airtight glass containers were modified from LeParfait® glass jars, which are originally designed for food preservation and are widely available in the market. In total three holes were drilled on the cap of the jar to implant two one-way gas valves and a wire bundle. Epoxy resin were applied to seal the gap between the edge of the holes and the implants to prevent air leakage. The two valves were used as the gas inlet and outlet, respectively.

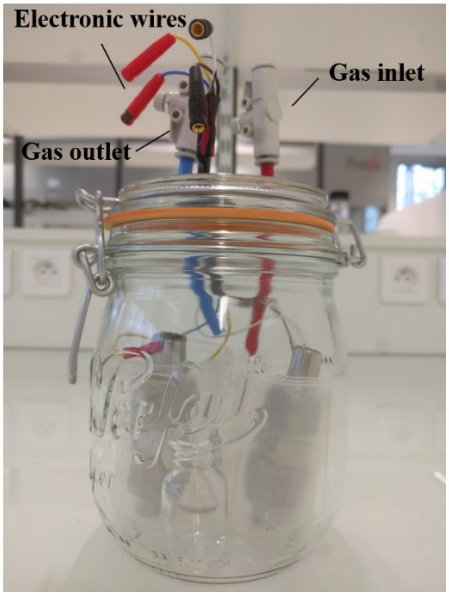

Figure 6.2: Photograph of the modified Le Parfait glass jar.

When being taken out of the glovebox, the glass jars were filled with argon, then they were purged with O_2 for 1 hour. As the glass jar cannot sustain pressure higher than 1.2 bar, the gas outlet was connected to ambient atmosphere through a silicon oil bubbler to prevent the backflow of air to the jar when O_2 purging stops.

The volume of the glass jars was 0.75 L and consuming all the O_2 in the jar to form Li_2O_2 provided a capacity of 1795 mAh. Considering that the discharge capacity obtained in the experiments were generally less than 2 mAh, corresponding to 0.2 mL of O_2 consumption, the pressure variations during the cycling were negligible. Besides, the large volume of the jar enabled simultaneous cycling of two SW cells so that the cells can experience the same environment during the cycling.

The galvanostatic cycling were performed with VMP3 multi-channel potentiostat (Biologic, France) at 25 °C. The cells were left as rest for 1h before cycling to ensure a good dissolution of O_2 in the electrolyte. The voltage cut-offs were set at 2.2 and 4.3 V for discharge and charge, respectively.

II.3 Scanning electron microscopy (SEM)

After cycling, SW cells were disassembled in an argon-filled glove box so as to recover the electrodes. The recovered electrodes were washed with a few drops of dry DMSO to remove residual salt from the electrolyte, then they were sealed in a plastic

bag to ensure the transfer to a scanning electron microscopy (SEM). To minimize the air exposure, the electrodes were quickly placed in the vacuum chamber of SEM. The analyses were carried out with a FEI Tecnai F20 microscope at a working voltage of 10 kV.

III. Experiments with carbon composites electrodes

At the beginning of my PhD, the experiments commonly reported in the literature were conducted with carbon composite electrodes. The discharge current density was then set with respect to the electrode mass, which was proportional to the true surface area of Csp. [39,49,86,200] In line with the literature, the carbon composite electrodes were tested firstly in our experiments.

III.1 Impact of the carbon casting method

The impact of the casting method on the discharge process has been investigated with two PTFE-based electrodes prepared from drop-casting and spray casting, respectively. Both electrodes had a weight of 0.8 mg and they were both discharged at a current density of 20 mA/$g_{electrode}$. However, their discharge behaviors were different as shown in **Figure 6.3 a**. With a relative flat potential plateau, the discharge capacity of the spray-casted electrode ended up with 1.13 mAh, which is much larger than the 0.68 mAh from drop-casted electrode showing a slopy discharge profile.

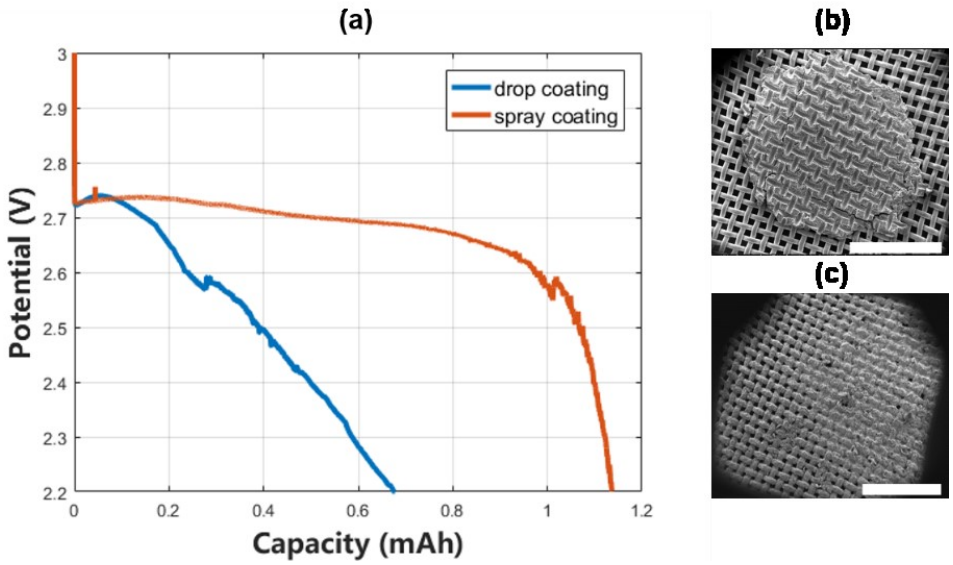

Figure 6.3: (a) Discharge profiles of PTFE-based electrodes prepared by drop coating and spray coating, with their SEM images showing in **(b)** and **(c)**, where the bar represents 2 mm. Both electrodes weight 0.8 mg and the discharge current density is 20 mA/$g_{electrode.}$

This difference can be attributed to distinct distributions of the carbon deposits. **Figure 6.3 b** and **c** displayed the SEM images of drop-casted and spray-casted electrodes. While in the former case, the carbon deposit is located in the center of the gird; in the latter case, the carbon deposit is distributed more dispersedly on the surface of the grid wires, leaving the space between the wires open. As a result, comparing to drop-coated electrode, spray-coated electrode has a better contact with the grid, leading to a more efficient current collection. Moreover, the open space between grid wires in spray-coated electrode enhances the O_2 accessibility to the carbon surface and alleviates the pore clogging in carbon as compared to the relatively compact drop-coated electrode. This thus leads to a higher capacity for spray-coated electrode.

The above comparison indicated that not only the mass but also the distribution of the carbon deposit strongly impacts the discharge performances. However, it is not easy to control the loading and distribution to obtain identical electrodes from a slurry-based process.

III.2 Impact of binder

In the carbon composite electrode, a polymer binder is used to hold the Csp particles together. PVdF is a commonly used binder in LIBs and it has also been applied

in LOBs.[39,107,201,202] Another binder which is commonly used in LOBs is PTFE.[49,173,203] Both of them have been tested in our experiments.

It is found that the discharge performance of carbon composite electrodes depends on the binder type. **Figure 6.4** shows the discharge profiles of PVdF-based and PTFE-based electrode, respectively. Both electrodes were prepared from drop-casting and have a similar weight (~1 mg). However, at the same discharge current density, the PVdF-based electrode has a discharge capacity slightly higher than 2.5 mAh, 3 times larger than the capacity of the PTFE-based electrode. At the same time, the discharge profiles were different. While the PTFE-based electrode showed a sharp drop all the way during the discharge, the discharge voltage of the PVdF-based electrode was fairly stable until the "sudden death".

The reason for such a difference is not clear. But it can be linked to the carbon detachment of PVdF-based electrode as observed in dissembled cells, which was mainly due to the dissolution of PVdF in DMSO. Though DMSO is listed as active solvent for PVdF in the product brochure from provider,[203] the solubility of PVdF in DMSO seems not to be well recognized in the Li-O_2 community as many experiment were reported to be performed with PVdF-based electrode in DMSO.[43,205,206] In our experiment, when PVdF dissolved into the DMSO, the carbon deposit then detached and went also in to solution. This detachment started from the outer layer of the deposit that was more likely to have pore clogging due to Li_2O_2 accumulation, thus it helped O_2 to access the inner part of the deposit, improving the discharge capacity.

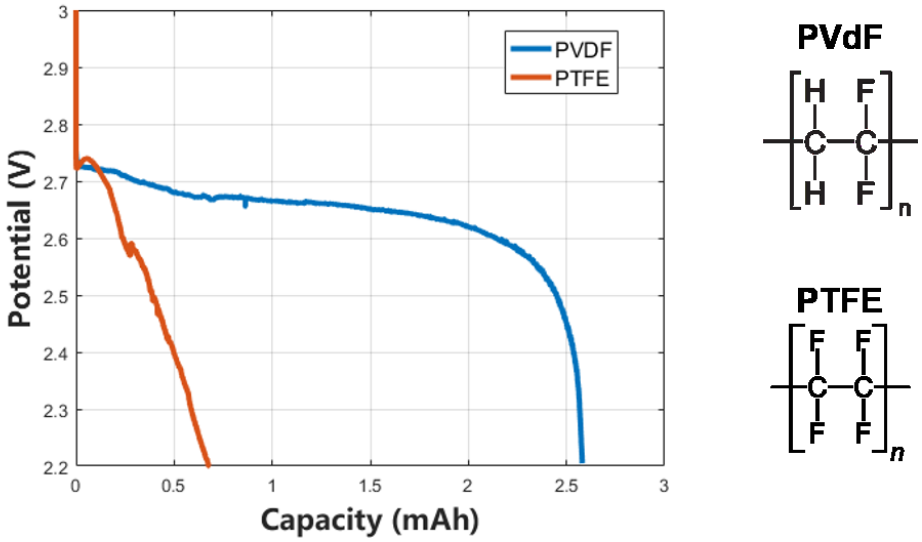

Figure 6.4: Discharge profiles of carbon composite electrode with PVdF and PTFE binder. Both electrodes contain 10 wt% of binder and were prepared by drop-casting. The discharge current density is 20 mA/$g_{electrode}$.

IV. Experiments with GDL electrodes

IV.1 Characterization of GDL

The thickness of the GDL is 207 µm and the mass loading is 95 g/m^2. Considering a density of carbon materials between 2.2~2.4 g/cm^3, the porosity of a GDL electrode is estimated to be 79.1~80.8 %, similar to 80 % as assumed in the model. The GDL disc electrodes have a diameter of 11 mm and their average weight is 9.3 mg. The SEM image showed that the GDL electrodes consist of interlaced carbon fibers whose radius (r) was around 5 µm (**Figure 6.5**).

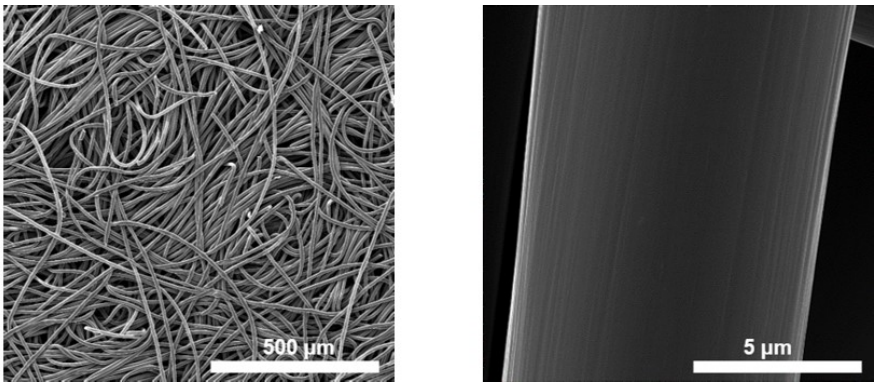

Figure 6.5: SEM images of pristine GDL electrode.

Assuming that the carbon fiber has smooth surface and its density (ρ) is around 2.3 g/cm^3, the specific surface area (SSA) can be determined by:

$$SSA = \frac{2\pi rl}{\pi r^2 l\rho} = 0.225\ m^2/g \qquad 6.1$$

The as-calculated SSA value agrees with the Brunauer–Emmett–Teller (BET) surface measurement (ASAP 2020, Micromeritics), which was around 0.2 m^2/g. Moreover, adsorption/desorption isotherm of GDL is of type II isotherm, indicating that GDL are macroporous materials, which is consistent with the assumption of ignoring pore clogging in the nucleation model (cf. **Chapter 4**).

Furthermore, Thermogravimetric Analysis/Mass Spectrometry (TGA-MS, STA449C Jupiter - QMS Aëolos 32, Netzsch) measurement of GDL has been performed under air from 25 to 1000 °C at a rate of 10 °C/min. TGA -MS results showed that over 99% of weight loss was between 600 to 900 °C, with CO_2 (m/z: 12, 44 and 45) as the predominate decomposition product (**Figure 6.6**), in agreement with the carbon oxidation. A small amount of CO_2 released at 340 °C which may originated from the decomposition of polymeric additives which are usually decomposed below 580 °C.[207] This weight loss (~ 0.3 %) indicates that the binder content in GDL is very low supporting the fact to be neglected in the models (cf. **Chapters 3, 4 and 5**).

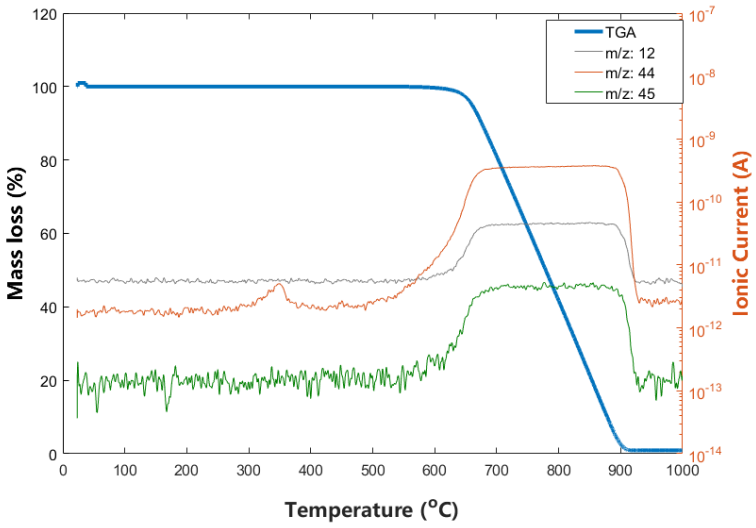

Figure 6.6: The TGA-MS results of GDL electrodes.

IV.2 An example of modeling/experiment coupling: impact of current density on the discharge process

To achieve a reliable comparison between modeling and experiment, the electrodes used in the experiment should be consistent with the assumptions in the model and be able to provide accurate parameters as inputs for the model. In this context, despite of a low SSA, GDL electrode is a good choice for the comparison between experiment and modeling, especially for the nucleation model reported in **Chapter 4** due to the following reasons:

(a) as self-standing materials, the variations of mass and texture between GDL electrodes are smaller than that between carbon composite electrodes;

(b) GDL consists of pure carbon fibers with almost no binder, thus the binder effects on the electrochemical response can be ignored in the GDL electrodes;

(c) due to the lack of mese-pores and micro-pores in GDL, the formed Li_2O_2 can only present on the surface of carbon fibers and can be easily observed by SEM;

(d) the macroporous characteristic of GDL reduces the possibility of pore clogging and supports the corresponding assumption in the nucleation model.

An issue concerning the modeling/experiment comparison is the variability of parameters values. While testing the impact of one parameter in a model is mainly by assigning different values to this parameter, it is tricky in an experiment to change a parameter without modifying simultaneously other parameters. For example, when we replace an electrolyte with another one, the observed change in discharge performance may result from the combination of the effects of the O_2 diffusion coefficient, LiO_2 solubility and L_2O_2/electrolyte surface energy. It may be possible to design a self-consistent model to predict concurrently the impacts of electrolyte on all the three aspects, but it reveals very complex to separate the impact of each individual parameter from the overall results of experiments. This makes the modeling/experiment quantitative comparison challenging. Fortunately, the operation conditions are

relatively more controllable. Thus, the discharge current has been chosen as the variable in this thesis to perform a comparison between the modeling and experimental results.

LOBs based on GDL disc electrodes were discharged in 1M $LiClO_4$/DMSO electrolyte at currents of 100, 50 and 20 μA, respectively. The current densities with respect to the apparent surface area of the GDL are accordingly 1, 0.5 and 0.2 mA/cm^2. As shown in **Figure 6.7 a**, the discharge capacity decreased with increasing of the discharge current density, which qualitatively agreed with the simulation results (**Figure 6.7 b**). Moreover, SEM shows that the Li_2O_2 particles in the fully discharge electrode have a radius of around 150 μm at 20 μA, which decreases to 75 μm when the current increases to 50 μA. Further increase of the current to 100 μA leads to the disappearing of the individual particles suggesting the formed Li_2O_2 might be in the form of thin-film. Assuming that this Li_2O_2 thin film is uniformly coated on the carbon fiber surface, the discharge capacity at 100 μA corresponds to a film thickness of around 4 nm, which is close to the critical tunneling distance reported by Viswanathan *et al.*[99] and used in our models (cf**. Chapters 4** and **5**). The trend in the Li_2O_2 size is again in qualitative agreement with the simulation results from the nucleation model. Moreover, the discharge profile at 20 μA obtained from experiment showed a similar potential dip as predicted by the model and this dip disappeared at higher current in both experimental and modeling results.

However, some quantitative differences between experimental and modeling results are observable. For instance, at the three testing currents, the discharge capacities obtained from experiments range from 4 to 70 mAh/g_{GDL}, while the simulated ones span from 7 to 39 mAh/g_{GDL}. The same trend was found in Li_2O_2 final particle radius. As shown in **Figure 6.8**, the Li_2O_2 radii obtained through simulations at 100, 50, and 20 μA, are 25, 50, and 100 nm, respectively, which is in good quantitative agreement with the experimental results.

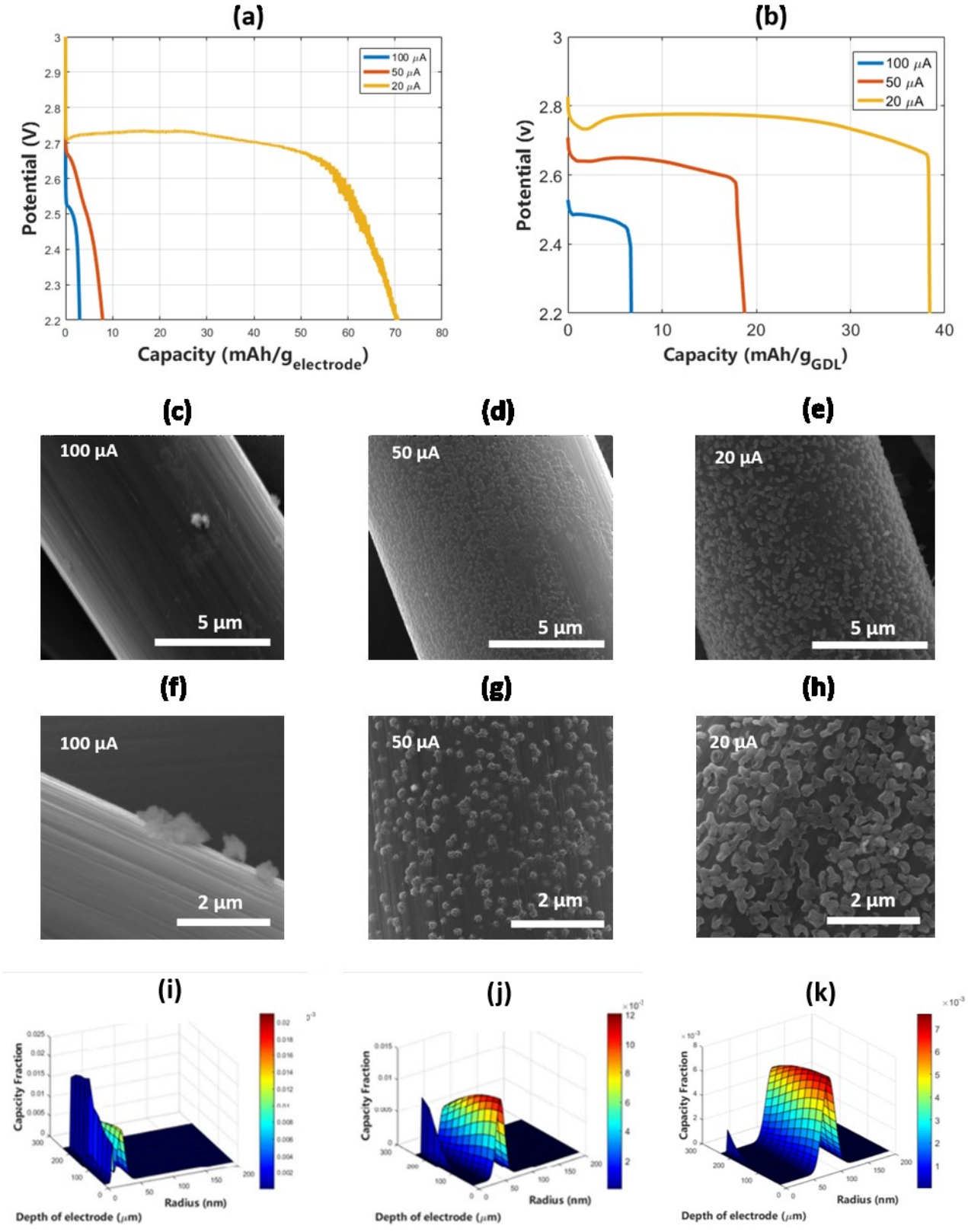

Figure 6.7: (a) Experimental and **(b)** simulated discharge profiles of GDL electrodes at current density of 20, 50, 100 μA, with the SEM images of the discharged electrodes shown in **(c)-(h)**.

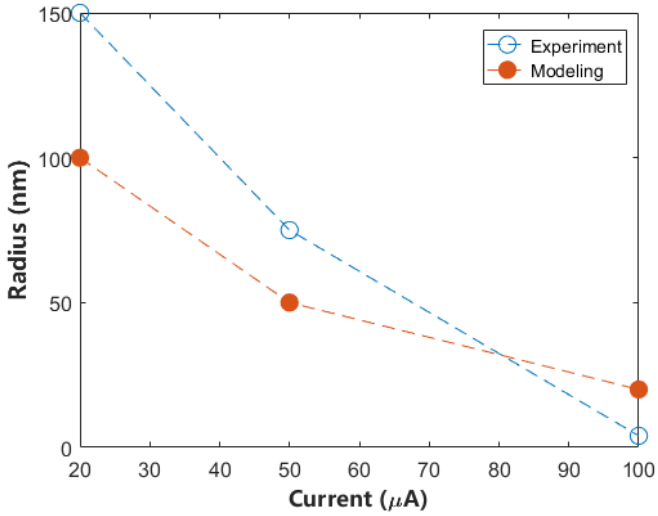

Figure 6.8: Evolution of Li_2O_2 particle final radius as a function of discharge currents from experiments (blue) and modeling (red).

The discrepancies between experimental and simulation results were inevitable not only due to the simplifications in the model, but also due to the possible uncertainties in the experimental measurement. For example, in the nucleation model, the concentration of $LiO_{2(ip)}$ has been generalized in each bin, however in reality, at the same depth of electrode, the local $LiO_{2(ip)}$ concentration close to the carbon fiber surface would be higher than the average concentration, particularly at high current density when more $LiO_{2(ip)}$ were formed close to the electrode surface but not have enough time to diffuse away to the bulk solution. As a result, the actual nucleation rate can be higher than the simulated rate, leading to a faster passivation of the electrode surface and a lower capacity as observed in experiments. Moreover, the chemical nucleation, which refers to the disproportionation of $LiO_{2(ip)}$, was overlooked in the model. This is a reasonable assumption at relative low currents, however, at high currents, with higher local $LiO_{2(ip)}$ concentrations, the collision frequency between two $LiO_{2(ip)}$ can increase, resulting in a higher probability for chemical nucleation. The impact of the chemical nucleation on the discharge performance can reveal complex. On one hand, the chemical nucleation may slow down the electrochemical nucleation by consuming $LiO_{2(ip)}$, leading to a delay of the electrode passivation; on the other hand, if the Li_2O_2 nucleus formed from chemical nucleation falls on the electrode surface and grows there, the chemical nucleation can then accelerate the electrode passivation. Besides, other simplifications, such as the hemispherical representation of the Li_2O_2 particles and

neglecting the electrochemical double layer effects, can also account for the quantitative deviation of the modeling results from experimental results.

In addition, the inaccuracies of the input parameters for the model can be responsible for the differences between modeling and experiments as well. Due to the lack of reliable sources to obtain accurate values for some parameters such as kinetic constants, surface energies and binding energies, they were estimated from relevant cases. For instance, the surface energy of Li_2O_2 in DMSO were adapted from the surface energy of Li_2O_2 in vacuum as reported in DFT calculations literature.

V. Conclusions

Compared to conventional carbon composite electrodes, GDL electrode was a better choice for the experimental characterization as its low binder content, macroporous texture and self-standing nature meets the modeling assumptions well. To examine the validity of the nucleation model reported in **Chapter 4**, the current density was chosen as the testing variable due to its good manageability.

The simulation results and the experimental results are in quantitative agreement. However deviations were inevitable not only due to the mechanism simplifications and parameter inaccuracies in the model, but possibly also due to the intrinsic uncertainties in the experimental measurements. Further work can be performed towards obtaining more reliable parameters for the model by combining other modeling techniques (*e.g.* DFT) or experimental measurements. Despite this, experimental results and simulation results were in good qualitative agreement: the shape of discharge profiles, the trend of discharge capacities, and trend of Li_2O_2 radius were found to be similar. This indicated that the model reported in **Chapter 4** is able to capture the essence of the discharge process. The analysis of the gap between modeling and experiments suggested the possible directions to further improve the model, such as including the chemical nucleation.

Moreover, though the GDL electrodes were ideal for model validation, they are not suitable for practical applications of LOBs due to their low specific surface area. The future work can be devoted to adapt the nucleation model to carbon composite electrodes where the evolution of pore size distribution should be considered to describe the pore clogging.

More generally, the experimental work reported in this Chapter established a basis for two other PhD thesis ongoing in the laboratory, and started one year later than my PhD: the cell setups developed during this thesis, reveal useful to them to perform systematic experimental studies.

Chapter 7 : General Conclusions

Due to their high theoretical capacity, LOBs have been considered as promising energy storage devices since their invention. However, the high complexity of these devices has impeded their practical application. Furthermore, the scattered experimental results and mechanistic theories reported in literature, add difficulties to develop a comprehensive understanding of their operation principles. The work accomplished in this thesis constitutes an effort to untangle the complexity of LOBs through the combination of modeling approaches with experiments, with the focus of obtaining a better understanding of the mechanisms interplays, rather than pursuing a perfect quantitative match between simulation and experimental results.

Within this thesis, the following topics were covered:

- Due to the lack of (re-)charge models in literature, a continuum cell model and a series of kinetic models have been developed to simulate the (re-)charge process of LOBs. By considering, as initial condition, a bi-modal PSD of Li2O2 formed during discharge, the simulation results were able to reproduce the experimentally-observed stepwise charge profile.

  The cell model attributed the stepwise profile to the Li_2O_2 size-dependent charge mechanisms. The deposition of large particles formed from the discharge solution mechanism has an activation energy barrier of 0.4 V, which is not necessary for small Li_2O_2 particles formed through the discharge surface mechanism. Thus, while small particles are decomposed at low voltage, the oxidation of large particles occurs only at high voltage.

  The kinetic models provided an alternative explanation for the stepwise charge profiles by considering Li_2O_2 as an electric resistor. As compared to the small particles, large Li_2O_2 particles cause a larger ohmic drop due to their high resistance and thus decompose at higher voltage. The Li_2O_2 resistance decreased during the decomposition due to their reduced size. However, the shrinking of active surface area counteracted the effects of the decreasing resistance. As a result, the electrode potential keep rising during the charge process.

  Furthermore, these charge models also suggested that the dependence of charging profiles on the discharge history can be explained by the evolution of the Li_2O_2 PSD at different discharge current densities.

- To calculate the PSD of Li2O2, a discharge cell model has been developed to simulate the nucleation and growth of Li2O2 by combining classical nucleation theory, elementary reaction kinetics and mass transport.

The simulation results provided insights to the potential dip and bending shape of the discharge profile as observed in the experiments. It is shown that this potential dip at the initial stage of the discharge is correlated to the nucleation process. Before the nucleation, the supersaturation of $LiO_{2(ip)}$ decreases the electrode potential. As the formation and growth of Li_2O_2 consume largely the $LiO_{2(ip)}$, the electrode potential then rises back and gradually reaches quasi-steady state. However, with the growth of Li_2O_2 particles, the surface area of the free electrode shrinks and the local current density increases, causing the decrease of electrode potential.

Moreover, the simulation results confirmed the preferential formation of Li_2O_2 close to the O_2 inlet and the bi-modal PSD of Li_2O_2. This PSD could have resulted from the nucleation process at the initial stage and the end stage of discharge process. The first nucleation was driven by the supersaturation of $LiO_{2(ip)}$, while the second nucleation was caused by the high electrode overpotential which is due to the increasing local current density resulting from the electrode passivation.

In addition, the model converges the impacts of current density, electrolyte property, and electrode chemical property to the nucleation process. As the nucleation process can be promoted by higher overpotential (resulting from higher current), higher surface energy of Li_2O_2/electrolyte interface, and stronger binding of Li_2O_2 to the electrode. Under these conditions, Li_2O_2 nuclei are quickly formed on the electrode surface, leading to a fast electrode passivation and a low discharge capacity. In contrast, less Li_2O_2 nuclei are formed when the overpotential is low (due to a low current density), or/and the surface energy of Li_2O_2/electrolyte interface is low, or/and the binding energy of Li_2O_2/electrode is relatively low. As a result, the formed nuclei are able to grow to large particles via not only electrochemical growth, but more importantly, through the chemical growth, resulting in a larger discharge capacity.

- Complementary to the deterministic models, stochastic models based on the kMC method have been developed, which focus on the meso-scale level and have been applied with different geometrical assumptions to the electrode structure.

The simulation results at the pore scale confirmed again the preferential formation of Li_2O_2 close to the O_2 inlet. The accumulation of Li_2O_2 can hinder the mass transport and even lead to pore/channel clogging. This highlighted the importance of optimizing the pore size and pore connectivity of the positive electrode. Moreover, the pore model reveals that lowering the salt concentration can promote discharge capacity due to the enhancement of O_2 mobility, which is in good agreement with experimental observations.

Also based on the kMC method, the fiber model focused on the formation of the Li_2O_2 on the catalyst-loaded and catalyst-free CNF (carbon nano-fiber). The simulation results suggested that the presence of catalysts on the CNF led to the inhomogeneous reaction kinetics on the fiber surface and the enhanced charge transfer rate, which resulted in a poor selectivity of reaction site. Consequently, the compactness and ordering of Li_2O_2 thin-film on the catalyst-loaded CNF were lower than the catalyst-free CNF. This is in agreement with the experimental observation of the decreasing Li_2O_2 crystallinity in presence of catalyst. As the amorphous Li_2O_2 is reported to be decomposed at lower voltage, this model suggested that instead of directly catalyzing the Li_2O_2 oxidation, the catalyst may rather lower the charge potential by tuning the Li_2O_2 crystallinity during discharge.

- In parallel to the modeling investigation, an experimental setup has been built to test the LOBs in conditions close to the assumed ones in the models. This setup was modified from commercial airtight jar and its large volume allowed cycling of two cells at the same time to ensure the identical environment for these two cells.

Moreover, as compared to carbon composite electrode, it is found that GDL electrode is a better model electrode due to its self-standing nature, macroporous texture, and low polymer content. By employing GDL discs as positive electrodes of LOBs, a series of experiments were performed to validate

the impact of the current on the discharge process as predicted by the discharge model. The experimental results are in good agreement with the model prediction with respect to the shape of the discharge profile, the variation trend of discharge capacity, and Li_2O_2 particle size at different currents.

Within this context, we found that the coupling of modeling and experiments can provide mechanistic insights into the complex interplays so as to obtain comprehensive understanding of the Li-O_2 system. In this coupling, modeling and experiments are mutually dependent. On one hand, models are extracted from experimental phenomena and fed with experimental parameters; on the other hand, modeling can be used as a tool to rationalize the experimental results and check the physical and chemical consistency of the theories proposed from experimental observations.

Moreover, the work in this thesis also indicated that instead of tightly binding together, modeling and experiment can be rather developed in parallel. While the communication between the theoretical and experimental approaches is important, it is difficult and unnecessary to have a perfect match and case-to-case validation due to unavoidable simplifications in models as well as the inherent limited accuracy of experimental measurements.

In front of all the challenges, it is still not clear if Li-O_2 technologies can be finally used for practical applications. However, the knowledge accumulated from an investigation coupling modeling and experiments is crucial to speed up the progress on understanding such complex systems.

It will be interesting to complete this work by performing model experiments on other effects such as the impact of electrode surface chemistry on the nucleation and growth of Li_2O_2, with the hope of strengthening the modeling/experiment coupling. Besides, a full-cycle model, which is able to simultaneously simulate the LOBs for multiple cycles, can be developed so as to further investigate the impact of cycling history on the cell performances.

This thesis work has provided useful inputs for two other ongoing PhDs on LOBs at LRCS. The “Le Parfait” setup has been used in their experiments for electrode

texture optimization and operation in ambient environment. The models developed during this thesis paved the way for them to develop more sophisticated models by including the parasitic reactions from electrolyte decomposition and air contaminants. Based on the 3D stochastic model, a VR game has been developed to introduce the concept and working principle of LOBs for the purpose of education.

More generally, the methodology proposed in this thesis can be also applied to other electrochemical systems including other metal-air batteries and Li-S batteries to develop comprehensive understanding. For instance, the nucleation model has been adapted to Li-S battery by a PhD student at LRCS to investigate the nucleation and growth of Li_2S. A similar model can also be useful for studying the Li plating to contribute to the development of Li-metal anodes for its application in LIBs, LOBs and Li-S batteries.

Bibliography

(1) Cowen, R. Voyager 1 Has Reached Interstellar Space. *Nat. News*. **2013**, doi : 10.1038/nature.2013.13735

(2) Larcher, D.; Tarascon, J.-M. Towards Greener and More Sustainable Batteries for Electrical Energy Storage. *Nat Chem.* **2015**, *7* (1), 19–29.

(3) Bithas, K.; Kalimeris, P. A Brief History of Energy Use in Human Societies. In *Revisiting the Energy-Development Link*; SpringerBriefs in Economics; Springer, Cham, 2016; pp 5–10.

(4) How Long before We Run out of Fossil Fuels? *Our World in Data*, 2017.

(5) Butt, N.; Beyer, H. L.; Bennett, J. R.; Biggs, D.; Maggini, R.; Mills, M.; Renwick, A. R.; Seabrook, L. M.; Possingham, H. P. Biodiversity Risks from Fossil Fuel Extraction. *Science.* **2013**, *342* (6157), 425–426.

(6) OECD, I. Energy and Air Pollution: World Energy Outlook Special Report 2016. **2016**.

(7) Climate change causes: A blanket around the Earth https://climate.nasa.gov/causes (accessed Nov 29, 2017).

(8) Publication: Renewables Information - 2017 edition - Overview https://www.iea.org/publications/freepublications/publication/renewables-information---2017-edition---overview.html (accessed Dec 15, 2017).

(9) The Danish Market : Danish Wind Industry Association http://www.windpower.org/en/knowledge/statistics/the_danish_market.html (accessed Dec 16, 2017).

(10) RENEWABLES 2017 GLOBAL STATUS REPORT http://www.ren21.net/gsr-2017/ (accessed Nov 30, 2017).

(11) Renewable Energy Data - Fraunhofer ISE http://www.ise.fraunhofer.de/en/renewable-energy-data.html (accessed Dec 3. 2017).

(12) http://ec.europa.eu/eurostat/statistics-explained/index.php?title=File:OIL-Final-Energy-Consumption-by-sector-EU28-1990-2014-MTOE.png&oldid=300945#filelinks (accessed Nov 30, 2017).

(13) Tarascon, J.-M.; Armand, M. Issues and Challenges Facing Rechargeable Lithium Batteries. *Nature* **2001**, *414* (6861), 359–367.

(14) Autonomie | ZOE | Véhicules Electriques | Véhicules | Renault FR https://www.renault.fr/vehicules/vehicules-electriques/zoe/autonomie.html (accessed Dec 15, 2017).

(15) Whittingham, M. S. Chemistry of Intercalation Compounds: Metal Guests in Chalcogenide Hosts. *Prog. Solid State Chem.* **1978**, *12* (1), 41–99.

(16) Ohzuku, T.; Ueda, A. Solid ‐ State Redox Reactions of $LiCoO_2$ ($R\bar{3}m$) for 4 Volt Secondary Lithium Cells. *J. Electrochem. Soc.* **1994**, *141* (11), 2972–2977.

(17) Reimers, J. N.; Dahn, J. R. Electrochemical and In Situ X-Ray Diffraction Studies of Lithium Intercalation in Li_xCoO_2. *J. Electrochem. Soc.* **1992**, *139* (8), 2091–2097.

(18) Cho, Y.; Cho, J. Significant Improvement of $LiNi_{0.8}Co_{0.15}Al_{0.05}O_2$ Cathodes at 60 ° C by SiO_2 Dry Coating for Li-Ion Batteries. *J. Electrochem. Soc.* **2010**, *157* (6), A625–A629.

(19) Hwang, B. J.; Tsai, Y. W.; Carlier, D.; Ceder, G. A Combined Computational/Experimental Study on $LiNi_{1/3}Co_{1/3}Mn_{1/3}O_2$. *Chem. Mater.* **2003**, *15* (19), 3676–3682.

(20) Shaju, K. M.; Bruce, P. G. A Stoichiometric Nano-$LiMn_2O_4$ Spinel Electrode Exhibiting High Power and Stable Cycling. *Chem. Mater.* **2008**, *20* (17), 5557–5562.

(21) Yamada, A.; Chung, S. C.; Hinokuma, K. Optimized $LiFePO_4$ for Lithium Battery Cathodes. *J. Electrochem. Soc.* **2001**, *148* (3), A224–A229.

(22) McRae, E.; Mareche, J.-F. Stage Dependence of the Electrical Resistivity of Graphite Intercalation Compounds. *J. Phys. C Solid State Phys.* **1985**, *18* (8), 1627.

(23) Levi, M. D.; Aurbach, D. Simultaneous Measurements and Modeling of the Electrochemical Impedance and the Cyclic Voltammetric Characteristics of Graphite Electrodes Doped with Lithium. *J. Phys. Chem. B* **1997**, *101* (23), 4630–4640.

(24) Scharner, S.; Weppner, W.; Schmid‐Beurmann, P. Evidence of Two‐Phase Formation upon Lithium Insertion into the $Li_{1.33}Ti_{1.67}O_4$ Spinel. *J. Electrochem. Soc.* **1999**, *146* (3), 857–861.

(25) Wagemaker, M.; Simon, D. R.; Kelder, E. M.; Schoonman, J.; Ringpfeil, C.; Haake, U.; Lützenkirchen-Hecht, D.; Frahm, R.; Mulder, F. M. A Kinetic Two-Phase and Equilibrium Solid Solution in Spinel $Li_{4+x}Ti_5O_{12}$. *Adv. Mater.* **2006**, *18* (23), 3169–3173.

(26) Brodd, R. J. *Batteries for Sustainability: Selected Entries from the Encyclopedia of Sustainability Science and Technology*; Springer Science & Business Media, 2012.

(27) Lu, J.; Li, L.; Park, J.-B.; Sun, Y.-K.; Wu, F.; Amine, K. Aprotic and Aqueous Li–O_2 Batteries. *Chem. Rev.* **2014**, *114* (11), 5611–5640.

(28) Choi, J. W.; Aurbach, D. Promise and Reality of Post-Lithium-Ion Batteries with High Energy Densities. *Nat. Rev. Mater.* **2016**, *1* (4), 16013.

(29) Abraham, K. M.; Jiang, Z. A Polymer Electrolyte‐Based Rechargeable Lithium/Oxygen Battery. *J. Electrochem. Soc.* **1996**, *143* (1), 1–5.

(30) Ogasawara, T.; Débart, A.; Holzapfel, M.; Novák, P.; Bruce, P. G. Rechargeable Li_2O_2 Electrode for Lithium Batteries. *J. Am. Chem. Soc.* **2006**, *128* (4), 1390–1393.

(31) Gallagher, K. G.; Goebel, S.; Greszler, T.; Mathias, M.; Oelerich, W.; Eroglu, D.; Srinivasan, V. Quantifying the Promise of Lithium–air Batteries for Electric Vehicles. *Energy Environ. Sci.* **2014**, *7* (5), 1555–1563.

(32) Ottakam Thotiyl, M. M.; Freunberger, S. A.; Peng, Z.; Bruce, P. G. The Carbon Electrode in Nonaqueous Li–O_2 Cells. *J. Am. Chem. Soc.* **2013**, *135* (1), 494–500.

(33) McCloskey, B. D.; Valery, A.; Luntz, A. C.; Gowda, S. R.; Wallraff, G. M.; Garcia, J. M.; Mori, T.; Krupp, L. E. Combining Accurate O_2 and Li_2O_2 Assays to Separate Discharge and Charge Stability Limitations in Nonaqueous Li–O2 Batteries. *J. Phys. Chem. Lett.* **2013**, *4* (17), 2989–2993.

(34) Lu, Y.-C.; Kwabi, D. G.; Yao, K. P. C.; Harding, J. R.; Zhou, J.; Zuin, L.; Shao-Horn, Y. The Discharge Rate Capability of Rechargeable Li–O_2 Batteries. *Energy Environ. Sci.* **2011**, *4* (8), 2999–3007.

(35) Adams, B. D.; Radtke, C.; Black, R.; Trudeau, M. L.; Zaghib, K.; Nazar, L. F. Current Density Dependence of Peroxide Formation in the Li–O_2 Battery and Its Effect on Charge. *Energy Environ. Sci.* **2013**, *6* (6), 1772–1778.

(36) Horstmann, B.; Gallant, B.; Mitchell, R.; Bessler, W. G.; Shao-Horn, Y.; Bazant, M. Z. Rate-Dependent Morphology of Li_2O_2 Growth in Li-O_2 Batteries. *J. Phys. Chem. Lett.* **2013**, *4* (24), 4217–4222.

(37) Griffith, L. D.; Sleightholme, A. E. S.; Mansfield, J. F.; Siegel, D. J.; Monroe, C. W. Correlating Li/O_2 Cell Capacity and Product Morphology with Discharge Current. *ACS Appl. Mater. Interfaces* **2015**, *7* (14), 7670–7678.

(38) Mitchell, R. R.; Gallant, B. M.; Shao-Horn, Y.; Thompson, C. V. Mechanisms of Morphological Evolution of Li2O2 Particles during Electrochemical Growth. *J. Phys. Chem. Lett.* **2013**, *4* (7), 1060–1064.

(39) Read, J.; Mutolo, K.; Ervin, M.; Behl, W.; Wolfenstine, J.; Driedger, A.; Foster, D. Oxygen Transport Properties of Organic Electrolytes and Performance of Lithium/Oxygen Battery. *J. Electrochem. Soc.* **2003**, *150* (10), A1351–A1356.

(40) Lu, Y.-C.; Gasteiger, H. A.; Parent, M. C.; Chiloyan, V.; Shao-Horn, Y. The Influence of Catalysts on Discharge and Charge Voltages of Rechargeable Li–Oxygen Batteries. *Electrochem. Solid-State Lett.* **2010**, *13* (6), A69.

(41) Laoire, C. Ó.; Mukerjee, S.; Plichta, E. J.; Hendrickson, M. A.; Abraham, K. M. Rechargeable Lithium/TEGDME-LiPF6/O_2 Battery. *J. Electrochem. Soc.* **2011**, *158* (3), A302–A308.

(42) Read, J. Ether-Based Electrolytes for the Lithium/Oxygen Organic Electrolyte Battery. *J. Electrochem. Soc.* **2006**, *153* (1), A96.

(43) Trahan, M. J.; Mukerjee, S.; Plichta, E. J.; Hendrickson, M. A.; Abraham, K. M. Studies of Li-Air Cells Utilizing Dimethyl Sulfoxide-Based Electrolyte. *J. Electrochem. Soc.* **2013**, *160* (2), A259–A267.

(44) Bondue, C. J.; Reinsberg, P.; Abd-El-Latif, A. A.; Baltruschat, H. Oxygen Reduction and Oxygen Evolution in DMSO Based Electrolytes: The Role of the Electrocatalyst. *Phys. Chem. Chem. Phys.* **2015**, *17* (38), 25593–25606.

(45) Yu, Q.; Ye, S. In Situ Study of Oxygen Reduction in Dimethyl Sulfoxide (DMSO) Solution: A Fundamental Study for Development of the Lithium–Oxygen Battery. *J. Phys. Chem. C* **2015**, *119* (22), 12236–12250.

(46) Walker, W.; Giordani, V.; Uddin, J.; Bryantsev, V. S.; Chase, G. V.; Addison, D. A Rechargeable Li–O2 Battery Using a Lithium Nitrate/N,N-Dimethylacetamide Electrolyte. *J. Am. Chem. Soc.* **2013**, *135* (6), 2076–2079.

(47) Allen, C. J.; Hwang, J.; Kautz, R.; Mukerjee, S.; Plichta, E. J.; Hendrickson, M. A.; Abraham, K. M. Oxygen Reduction Reactions in Ionic Liquids and the Formulation of a General ORR Mechanism for Li–Air Batteries. *J. Phys. Chem. C* **2012**, *116* (39), 20755–20764.

(48) Gebresilassie Eshetu, G.; Armand, M.; Scrosati, B.; Passerini, S. Energy Storage Materials Synthesized from Ionic Liquids. *Angew. Chem. Int. Ed.* **2014**, n/a-n/a.

(49) Johnson, L.; Li, C.; Liu, Z.; Chen, Y.; Freunberger, S. A.; Ashok, P. C.; Praveen, B. B.; Dholakia, K.; Tarascon, J.-M.; Bruce, P. G. The Role of LiO_2 Solubility in O_2 Reduction in Aprotic Solvents and Its Consequences for Li–O_2 Batteries. *Nat. Chem.* **2014**, *6* (12), 1091–1099.

(50) Peng, Z.; Freunberger, S. A.; Hardwick, L. J.; Chen, Y.; Giordani, V.; Bardé, F.; Novák, P.; Graham, D.; Tarascon, J.-M.; Bruce, P. G. Oxygen Reactions in a Non-Aqueous Li+ Electrolyte. *Angew. Chem. Int. Ed.* **2011**, *50* (28), 6351–6355.

(51) Yang, J.; Zhai, D.; Wang, H.-H.; Lau, K. C.; Schlueter, J. A.; Du, P.; Myers, D. J.; Sun, Y.-K.; Curtiss, L. A.; Amine, K. Evidence for Lithium Superoxide-like Species in the Discharge Product of a Li–O_2 Battery. *Phys. Chem. Chem. Phys.* **2013**, *15* (11), 3764–3771.

(52) Abraham, K. M. Electrolyte-Directed Reactions of the Oxygen Electrode in Lithium-Air Batteries. *J. Electrochem. Soc.* **2015**, *162* (2), A3021–A3031.

(53) Scheers, J.; Lidberg, D.; Sodeyama, K.; Futera, Z.; Tateyama, Y. Life of Superoxide in Aprotic Li–O_2 Battery Electrolytes: Simulated Solvent and Counter-Ion Effects. *Phys. Chem. Chem. Phys.* **2016**, *18* (15), 9961–9968.

(54) Das, U.; Lau, K. C.; Redfern, P. C.; Curtiss, L. A. Structure and Stability of Lithium Superoxide Clusters and Relevance to Li–O_2 Batteries. *J. Phys. Chem. Lett.* **2014**, *5* (5), 813–819.

(55) Gutmann, V. Empirical Parameters for Donor and Acceptor Properties of Solvents. *Electrochimica Acta* **1976**, *21* (9), 661–670.

(56) Mayer, U.; Gutmann, V.; Gerger, W. The Acceptor Number — A Quantitative Empirical Parameter for the Electrophilic Properties of Solvents. *Monatshefte Für Chem. Chem. Mon.* **1975**, *106* (6), 1235–1257.

(57) Sharon, D.; Hirsberg, D.; Salama, M.; Afri, M.; Frimer, A. A.; Noked, M.; Kwak, W.; Sun, Y.-K.; Aurbach, D. Mechanistic Role of Li+ Dissociation Level in Aprotic Li–O_2 Battery. *ACS Appl. Mater. Interfaces* **2016**, *8* (8), 5300–5307.

(58) Burke, C. M.; Pande, V.; Khetan, A.; Viswanathan, V.; McCloskey, B. D. Enhancing Electrochemical Intermediate Solvation through Electrolyte Anion Selection to Increase Nonaqueous Li–O_2 Battery Capacity. *Proc. Natl. Acad. Sci.* **2015**, *112* (30), 9293–9298.

(59) Elia, G. A.; Park, J.-B.; Sun, Y.-K.; Scrosati, B.; Hassoun, J. Role of the Lithium Salt in the Performance of Lithium–Oxygen Batteries: A Comparative Study. *ChemElectroChem* **2014**, *1* (1), 47–50.

(60) Gunasekara, I.; Mukerjee, S.; Plichta, E. J.; Hendrickson, M. A.; Abraham, K. M. A Study of the Influence of Lithium Salt Anions on Oxygen Reduction Reactions in Li-Air Batteries. *J. Electrochem. Soc.* **2015**, *162* (6), A1055–A1066.

(61) Liu, B.; Xu, W.; Yan, P.; Sun, X.; Bowden, M. E.; Read, J.; Qian, J.; Mei, D.; Wang, C.-M.; Zhang, J.-G. Enhanced Cycling Stability of Rechargeable Li–O_2 Batteries Using High-Concentration Electrolytes. *Adv. Funct. Mater.* **2016**, *26* (4), 605–613.

(62) Markus, I. M.; Jones, G.; García, J. M. Investigation of Electrolyte Concentration Effects on the Performance of Lithium–Oxygen Batteries. *J. Phys. Chem. C* **2016**, *120* (11), 5949–5957.

(63) Mohazabrad, F.; Wang, F.; Li, X. Experimental Studies of Salt Concentration in Electrolyte on the Performance of Li-O_2 Batteries at Various Current Densities. *J. Electrochem. Soc.* **2016**, *163* (13), A2623–A2627.

(64) Gittleson, F. S.; Jones, R. E.; Ward, D. K.; Foster, M. E. Oxygen Solubility and Transport in Li–air Battery Electrolytes: Establishing Criteria and Strategies for Electrolyte Design. *Energy Environ. Sci.* **2017**, *10* (5), 1167–1179.

(65) Débart, A.; Bao, J.; Armstrong, G.; Bruce, P. G. An O_2 Cathode for Rechargeable Lithium Batteries: The Effect of a Catalyst. *J. Power Sources* **2007**, *174* (2), 1177–1182.

(66) Read, J. Characterization of the Lithium/Oxygen Organic Electrolyte Battery. *J. Electrochem. Soc.* **2002**, *149* (9), A1190–A1195.

(67) Mizuno, F.; Takechi, K.; Higashi, S.; Shiga, T.; Shiotsuki, T.; Takazawa, N.; Sakurabayashi, Y.; Okazaki, S.; Nitta, I.; Kodama, T.; et al. Cathode Reaction Mechanism of Non-Aqueous Li–O_2 Batteries with Highly Oxygen Radical Stable Electrolyte Solvent. *J. Power Sources* **2013**, *228*, 47–56.

(68) Bryantsev, V. S.; Blanco, M. Computational Study of the Mechanisms of Superoxide-Induced Decomposition of Organic Carbonate-Based Electrolytes. *J. Phys. Chem. Lett.* **2011**, *2* (5), 379–383.

(69) Freunberger, S. A.; Chen, Y.; Peng, Z.; Griffin, J. M.; Hardwick, L. J.; Bardé, F.; Novák, P.; Bruce, P. G. Reactions in the Rechargeable Lithium–O_2 Battery with Alkyl Carbonate Electrolytes. *J. Am. Chem. Soc.* **2011**, *133* (20), 8040–8047.

(70) Bardé, F.; Chen, Y.; Johnson, L.; Schaltin, S.; Fransaer, J.; Bruce, P. G. Sulfone-Based Electrolytes for Nonaqueous Li–O_2 Batteries. *J. Phys. Chem. C* **2014**, *118* (33), 18892–18898.

(71) Chen, Y.; Freunberger, S. A.; Peng, Z.; Bardé, F.; Bruce, P. G. Li–O_2 Battery with a Dimethylformamide Electrolyte. *J. Am. Chem. Soc.* **2012**, *134* (18), 7952–7957.

(72) Younesi, R.; Norby, P.; Vegge, T. A New Look at the Stability of Dimethyl Sulfoxide and Acetonitrile in Li-O_2 Batteries. *ECS Electrochem. Lett.* **2014**, *3* (3), A15–A18.

(73) Schwenke, K. U.; Meini, S.; Wu, X.; Gasteiger, H. A.; Piana, M. Stability of Superoxide Radicals in Glyme Solvents for Non-Aqueous Li–O_2 Battery Electrolytes. *Phys. Chem. Chem. Phys.* **2013**, *15* (28), 11830–11839.

(74) Black, R.; Oh, S. H.; Lee, J.-H.; Yim, T.; Adams, B.; Nazar, L. F. Screening for Superoxide Reactivity in Li-O_2 Batteries: Effect on Li_2O_2/LiOH Crystallization. *J. Am. Chem. Soc.* **2012**, *134* (6), 2902–2905.

(75) Bryantsev, V. S.; Faglioni, F. Predicting Autoxidation Stability of Ether- and Amide-Based Electrolyte Solvents for Li–Air Batteries. *J. Phys. Chem. A* **2012**, *116* (26), 7128–7138.

(76) Nasybulin, E.; Xu, W.; Engelhard, M. H.; Nie, Z.; Burton, S. D.; Cosimbescu, L.; Gross, M. E.; Zhang, J.-G. Effects of Electrolyte Salts on the Performance of Li–O_2 Batteries. *J. Phys. Chem. C* **2013**, *117* (6), 2635–2645.

(77) Li, Y.; Li, X.; Geng, D.; Tang, Y.; Li, R.; Dodelet, J.-P.; Lefèvre, M.; Sun, X. Carbon Black Cathodes for Lithium Oxygen Batteries: Influence of Porosity and Heteroatom-Doping. *Carbon* **2013**, *64* (Supplement C), 170–177.

(78) Yang, C.; Wong, R. A.; Hong, M.; Yamanaka, K.; Ohta, T.; Byon, H. R. Unexpected Li_2O_2 Film Growth on Carbon Nanotube Electrodes with CeO_2 Nanoparticles in Li–O_2 Batteries. *Nano Lett.* **2016**, *16* (5), 2969–2974.

(79) Gallant, B. M.; Mitchell, R. R.; Kwabi, D. G.; Zhou, J.; Zuin, L.; Thompson, C. V.; Shao-Horn, Y. Chemical and Morphological Changes of Li–O_2 Battery Electrodes upon Cycling. *J. Phys. Chem. C* **2012**, *116* (39), 20800–20805.

(80) Mi, R.; Liu, H.; Wang, H.; Wong, K.-W.; Mei, J.; Chen, Y.; Lau, W.-M.; Yan, H. Effects of Nitrogen-Doped Carbon Nanotubes on the Discharge Performance of Li-Air Batteries. *Carbon* **2014**, *67*, 744–752.

(81) Li, Y.; Wang, J.; Li, X.; Geng, D.; Li, R.; Sun, X. Superior Energy Capacity of Graphene Nanosheets for a Nonaqueous Lithium-Oxygen Battery. *Chem. Commun.* **2011**, *47* (33), 9438–9440.

(82) Liu, T.; Leskes, M.; Yu, W.; Moore, A. J.; Zhou, L.; Bayley, P. M.; Kim, G.; Grey, C. P. Cycling Li-O_2 Batteries via LiOH Formation and Decomposition. *Science* **2015**, *350* (6260), 530–533.

(83) Lu, J.; Lee, Y. J.; Luo, X.; Lau, K. C.; Asadi, M.; Wang, H.-H.; Brombosz, S.; Wen, J.; Zhai, D.; Chen, Z.; et al. A Lithium-Oxygen Battery Based on Lithium Superoxide. *Nature* **2016**, *529* (7586), 377–382.

(84) Wong, R. A.; Dutta, A.; Yang, C.; Yamanaka, K.; Ohta, T.; Nakao, A.; Waki, K.; Byon, H. R. Structurally Tuning Li_2O_2 by Controlling the Surface Properties of Carbon Electrodes: Implications for Li-O_2 Batteries. *Chem. Mater.* **2016**.

(85) Belova, A. I.; Kwabi, D. G.; Yashina, L. V.; Shao-Horn, Y.; Itkis, D. M. Mechanism of Oxygen Reduction in Aprotic Li–Air Batteries: The Role of Carbon Electrode Surface Structure. *J. Phys. Chem. C* **2017**, *121* (3), 1569–1577.

(86) McCloskey, B. D.; Valery, A.; Luntz, A. C.; Gowda, S. R.; Wallraff, G. M.; Garcia, J. M.; Mori, T.; Krupp, L. E. Combining Accurate O_2 and Li_2O_2 Assays to Separate Discharge and Charge Stability Limitations in Nonaqueous Li–O2 Batteries. *J. Phys. Chem. Lett.* **2013**, *4* (17), 2989–2993.

(87) Peng, Z.; Freunberger, S. A.; Chen, Y.; Bruce, P. G. A Reversible and Higher-Rate Li-O2 Battery. *Science* **2012**, *337* (6094), 563–566.

(88) Ottakam Thotiyl, M. M.; Freunberger, S. A.; Peng, Z.; Chen, Y.; Liu, Z.; Bruce, P. G. A Stable Cathode for the Aprotic Li–O_2 Battery. *Nat. Mater.* **2013**, *12* (11), 1050–1056.

(89) Reinsberg, P.; Weiß, A.; Bawol, P. P.; Baltruschat, H. Electrochemical Reaction Order of the Oxygen Reduction Reaction in Li+-Containing DMSO. *J. Phys. Chem. C* **2017**.

(90) Meini, S.; Piana, M.; Beyer, H.; Schwämmlein, J.; Gasteiger, H. A. Effect of Carbon Surface Area on First Discharge Capacity of Li-O_2 Cathodes and Cycle-Life Behavior in Ether-Based Electrolytes. *J. Electrochem. Soc.* **2012**, *159* (12), A2135–A2142.

(91) Cheng, H.; Scott, K. Carbon-Supported Manganese Oxide Nanocatalysts for Rechargeable Lithium–air Batteries. *J. Power Sources* **2010**, *195* (5), 1370–1374.

(92) Hayashi, M.; Minowa, H.; Takahashi, M.; Shodai, T. Surface Properties and Electrochemical Performance of Carbon Materials for Air Electrodes of Lithium-Air Batteries. *Electrochemistry* **2010**, *78* (5), 325–328.

(93) Ma, S. B.; Lee, D. J.; Roev, V.; Im, D.; Doo, S.-G. Effect of Porosity on Electrochemical Properties of Carbon Materials as Cathode for Lithium-Oxygen Battery. *J. Power Sources* **2013**, *244* (Supplement C), 494–498.

(94) Ding, N.; Chien, S. W.; Hor, T. S. A.; Lum, R.; Zong, Y.; Liu, Z. Influence of Carbon Pore Size on the Discharge Capacity of Li–O_2 Batteries. *J. Mater. Chem. A* **2014**, *2* (31), 12433–12441.

(95) Landa-Medrano, I.; Pinedo, R.; de Larramendi, I. R.; Ortiz-Vitoriano, N.; Rojo, T. Monitoring the Location of Cathode-Reactions in Li-O_2 Batteries. *J. Electrochem. Soc.* **2015**, *162* (2), A3126–A3132.

(96) Sakai, K.; Iwamura, S.; Mukai, S. R. Influence of the Porous Structure of the Cathode on the Discharge Capacity of Lithium-Air Batteries. *J. Electrochem. Soc.* **2017**, *164* (13), A3075–A3080.

(97) Xue, K.-H.; McTurk, E.; Johnson, L.; Bruce, P. G.; Franco, A. A. A Comprehensive Model for Non-Aqueous Lithium Air Batteries Involving Different Reaction Mechanisms. *J. Electrochem. Soc.* **2015**, *162* (4), A614–A621.

(98) Hummelshøj, J. S.; LOBmqvist, J.; Datta, S.; Vegge, T.; Rossmeisl, J.; Thygesen, K. S.; Luntz, A. C.; Jacobsen, K. W.; Nørskov, J. K. Communications: Elementary Oxygen Electrode Reactions in the Aprotic Li-Air Battery. *J. Chem. Phys.* **2010**, *132* (7), 071101.

(99) Viswanathan, V.; Thygesen, K. S.; Hummelshøj, J. S.; Nørskov, J. K.; Girishkumar, G.; McCloskey, B. D.; Luntz, A. C. Electrical Conductivity in Li_2O_2 and Its Role in Determining Capacity Limitations in Non-Aqueous Li-O_2 Batteries. *J. Chem. Phys.* **2011**, *135* (21), 214704.

(100) Radin, M. D.; Rodriguez, J. F.; Tian, F.; Siegel, D. J. Lithium Peroxide Surfaces Are Metallic, While Lithium Oxide Surfaces Are Not. *J. Am. Chem. Soc.* **2012**, *134* (2), 1093–1103.

(101) Geng, W. T.; He, B. L.; Ohno, T. Grain Boundary Induced Conductivity in Li_2O_2. *J. Phys. Chem. C* **2013**, *117* (48), 25222–25228.

(102) Ong, S. P.; Mo, Y.; Ceder, G. Low Hole Polaron Migration Barrier in Lithium Peroxide. *Phys. Rev. B* **2012**, *85* (8), 081105.

(103) Tian, F.; Radin, M. D.; Siegel, D. J. Enhanced Charge Transport in Amorphous Li_2O_2. *Chem. Mater.* **2014**, *26* (9), 2952–2959.

(104) Zhang, Y.; Cui, Q.; Zhang, X.; McKee, W. C.; Xu, Y.; Ling, S.; Li, H.; Zhong, G.; Yang, Y.; Peng, Z. Amorphous Li_2O_2: Chemical Synthesis and Electrochemical Properties. *Angew. Chem. Int. Ed.* **2016**, n/a-n/a.

(105) McCloskey, B. D.; Speidel, A.; Scheffler, R.; Miller, D. C.; Viswanathan, V.; Hummelshøj, J. S.; Nørskov, J. K.; Luntz, A. C. Twin Problems of Interfacial Carbonate Formation in Nonaqueous Li–O_2 Batteries. *J. Phys. Chem. Lett.* **2012**, *3* (8), 997–1001.

(106) Kang, S.; Mo, Y.; Ong, S. P.; Ceder, G. A Facile Mechanism for Recharging Li_2O_2 in Li–O_2 Batteries. *Chem. Mater.* **2013**, *25* (16), 3328–3336.

(107) Zhai, D.; Wang, H.-H.; Yang, J.; Lau, K. C.; Li, K.; Amine, K.; Curtiss, L. A. Disproportionation in Li–O_2 Batteries Based on a Large Surface Area Carbon Cathode. *J. Am. Chem. Soc.* **2013**, *135* (41), 15364–15372.

(108) Lu, Y.-C.; Shao-Horn, Y. Probing the Reaction Kinetics of the Charge Reactions of Nonaqueous Li–O_2 Batteries. *J. Phys. Chem. Lett.* **2013**, *4* (1), 93–99.

(109) Lu, Y.-C.; Crumlin, E. J.; Carney, T. J.; Baggetto, L.; Veith, G. M.; Dudney, N. J.; Liu, Z.; Shao-Horn, Y. Influence of Hydrocarbon and CO_2 on the Reversibility of Li–O_2 Chemistry Using In Situ Ambient Pressure X-Ray Photoelectron Spectroscopy. *J. Phys. Chem. C* **2013**, *117* (49), 25948–25954.

(110) Zhai, D.; Wang, H.-H.; Lau, K. C.; Gao, J.; Redfern, P. C.; Kang, F.; Li, B.; Indacochea, E.; Das, U.; Sun, H.-H.; et al. Raman Evidence for Late Stage Disproportionation in a Li–O2 Battery. *J. Phys. Chem. Lett.* **2014**, *5* (15), 2705–2710.

(111) Ganapathy, S.; Heringa, J. R.; Anastasaki, M. S.; Adams, B. D.; van Hulzen, M.; Basak, S.; Li, Z.; Wright, J. P.; Nazar, L. F.; van Dijk, N. H.; et al. Operando Nanobeam Diffraction to Follow the Decomposition of Individual Li_2O_2 Grains in a Nonaqueous Li–O_2 Battery. *J. Phys. Chem. Lett.* **2016**, *7* (17), 3388–3394.

(112) Franco, A. A. *PEMFC Degradation Modeling and Analysis, Book Chapter in: Polymer Electrolyte Membrane and Direct Methanol Fuel Cell Technology (PEMFCs and DMFCs)-Volume 1: Fundamentals and Performance, Edited by C*; Hartnig and C. Roth (publisher: Woodhead, Cambridge, UK), 2011.

(113) Lu, Y.-C.; Xu, Z.; Gasteiger, H. A.; Chen, S.; Hamad-Schifferli, K.; Shao-Horn, Y. Platinum−Gold Nanoparticles: A Highly Active Bifunctional Electrocatalyst for Rechargeable Lithium−Air Batteries. *J. Am. Chem. Soc.* **2010**, *132* (35), 12170–12171.

(114) Kwak, W.-J.; Kang, T.-G.; Sun, Y.-K.; Lee, Y. J. Iron–cobalt Bimetal Decorated Carbon Nanotubes as Cost-Effective Cathode Catalysts for Li–O_2 Batteries. *J Mater Chem A* **2016**, *4* (18), 7020–7026.

(115) Trahey, L.; Karan, N. K.; Chan, M. K. Y.; Lu, J.; Ren, Y.; Greeley, J.; Balasubramanian, M.; Burrell, A. K.; Curtiss, L. A.; Thackeray, M. M. Synthesis, Characterization, and Structural Modeling of High-Capacity, Dual Functioning MnO_2 Electrode/Electrocatalysts for Li-O_2 Cells. *Adv. Energy Mater.* **2013**, *3* (1), 75–84.

(116) Qin, Y.; Lu, J.; Du, P.; Chen, Z.; Ren, Y.; Wu, T.; Miller, J. T.; Wen, J.; Miller, D. J.; Zhang, Z.; et al. In Situ Fabrication of Porous-Carbon-Supported α-MnO_2 Nanorods at Room Temperature: Application for Rechargeable Li–O_2 Batteries. *Energy Environ. Sci.* **2013**, *6* (2), 519–531.

(117) McCloskey, B. D.; Addison, D. A Viewpoint on Heterogeneous Electrocatalysis and Redox Mediation in Nonaqueous Li-O_2 Batteries. *ACS Catal.* **2017**, *7* (1), 772–778.

(118) Yang, Y.; Zhang, T.; Wang, X.; Chen, L.; Wu, N.; Liu, W.; Lu, H.; Xiao, L.; Fu, L.; Zhuang, L. Tuning the Morphology and Crystal Structure of Li_2O_2 : A Graphene Model Electrode Study for Li–O_2 Battery. *ACS Appl. Mater. Interfaces* **2016**.

(119) McCloskey, B. D.; Scheffler, R.; Speidel, A.; Bethune, D. S.; Shelby, R. M.; Luntz, A. C. On the Efficacy of Electrocatalysis in Nonaqueous Li–O_2 Batteries. *J. Am. Chem. Soc.* **2011**, *133* (45), 18038–18041.

(120) Chen, Y.; Freunberger, S. A.; Peng, Z.; Fontaine, O.; Bruce, P. G. Charging a Li–O_2 Battery Using a Redox Mediator. *Nat. Chem.* **2013**, *5* (6), 489–494.

(121) Gao, X.; Chen, Y.; Johnson, L.; Bruce, P. G. Promoting Solution Phase Discharge in Li-O_2 Batteries Containing Weakly Solvating Electrolyte Solutions. *Nat. Mater.* **2016**, *15* (8), 882–888.

(122) Kwak, W.-J.; Hirshberg, D.; Sharon, D.; Afri, M.; Frimer, A. A.; Jung, H.-G.; Aurbach, D.; Sun, Y.-K. Li–O_2 Cells with LiBr as an Electrolyte and a Redox Mediator. *Energy Environ. Sci.* **2016**, *9* (7), 2334–2345.

(123) Burke, C. M.; Black, R.; Kochetkov, I. R.; Giordani, V.; Addison, D.; Nazar, L. F.; McCloskey, B. D. Implications of 4 e^- Oxygen Reduction via Iodide Redox Mediation in Li–O_2 Batteries. *ACS Energy Lett.* **2016**, *1* (4), 747–756.

(124) Liang, Z.; Lu, Y.-C. Critical Role of Redox Mediator in Suppressing Charging Instabilities of Lithium–Oxygen Batteries. *J. Am. Chem. Soc.* **2016**, *138* (24), 7574–7583.

(125) Encyclopedia of Interfacial Chemistry - 1st Edition: https://www.elsevier.com/books/encyclopedia-of-interfacial-chemistry/unknown/978-0-12-809739-7 (accessed Jan 4, 2018).

(126) de Morais, R. F.; Sautet, P.; Loffreda, D.; Franco, A. A. A Multiscale Theoretical Methodology for the Calculation of Electrochemical Observables from Ab Initio Data: Application to the Oxygen Reduction Reaction in a Pt(1 1 1)-Based Polymer Electrolyte Membrane Fuel Cell. *Electrochimica Acta* **2011**, *56* (28), 10842–10856.

(127) Malek, K.; Franco, A. A. Microstructure-Based Modeling of Aging Mechanisms in Catalyst Layers of Polymer Electrolyte Fuel Cells. *J. Phys. Chem. B* **2011**, *115* (25), 8088–8101.

(128) Gagliardi, A.; Mastroianni, S.; Gentilini, D.; Giordano, F.; Reale, A.; Brown, T. M.; Carlo, A. D. Multiscale Modeling of Dye Solar Cells and Comparison With Experimental Data. *IEEE J. Sel. Top. Quantum Electron.* **2010**, *16* (6), 1611–1618.

(129) Salmi, T.; Bouzguenda, M.; Gastli, A.; Masmoudi, A. MATLAB/Simulink Based Modeling of Photovoltaic Cell. *Int. J. Renew. Energy Res. IJRER* **2012**, *2* (2), 213–218.

(130) Franco, A. A.; Doublet, M. L.; Bessler, W. G. *Physical Multiscale Modeling and Numerical Simulation of Electrochemical Devices for Energy Conversion and Storage: From Theory to Engineering to Practice*; Springer, 2015.

(131) Luntz, A. C.; Viswanathan, V.; Voss, J.; Varley, J. B.; Nørskov, J. K.; Scheffler, R.; Speidel, A. Tunneling and Polaron Charge Transport through Li_2O_2 in Li–O_2 Batteries. *J. Phys. Chem. Lett.* **2013**, *4* (20), 3494–3499.

(132) Varley, J. B.; Viswanathan, V.; Nørskov, J. K.; Luntz, A. C. Lithium and Oxygen Vacancies and Their Role in Li_2O_2 Charge Transport in Li–O_2 Batteries. *Energy Environ. Sci.* **2014**, *7* (2), 720–727.

(133) Dathar, G. K. P.; Shelton, W. A.; Xu, Y. Trends in the Catalytic Activity of Transition Metals for the Oxygen Reduction Reaction by Lithium. *J. Phys. Chem. Lett.* **2012**, *3* (7), 891–895.

(134) Franco, A. A. *Rechargeable Lithium Batteries: From Fundamentals to Applications*; Woodhead/Elsevier publishing, 2015.

(135) Islam, M. S. Recent Atomistic Modelling Studies of Energy Materials: Batteries Included. *Philos. Trans. R. Soc. Lond. Math. Phys. Eng. Sci.* **2010**, *368* (1923), 3255–3267.

(136) Deng, Y.; Eames, C.; Chotard, J.-N.; Lalère, F.; Seznec, V.; Emge, S.; Pecher, O.; Grey, C. P.; Masquelier, C.; Islam, M. S. Structural and Mechanistic Insights into Fast Lithium-Ion Conduction in Li_4SiO_4–Li_3PO_4 Solid Electrolytes. *J. Am. Chem. Soc.* **2015**, *137* (28), 9136–9145.

(137) Islam, M. S. Computer Modelling of Defects and Transport in Perovskite Oxides. *Solid State Ion.* **2002**, *154*, 75–85.

(138) Sergeev, A.; Chertovich, A.; Itkis, D.; Sen, A.; Gross, A.; Khokhlov, A. Electrode/Electrolyte Interface in the Li-O_2 Battery: Insight from Molecular Dynamics Study. *ArXiv Prepr. ArXiv170102086* **2017**.

(139) Senftle, T. P.; Hong, S.; Islam, M. M.; Kylasa, S. B.; Zheng, Y.; Shin, Y. K.; Junkermeier, C.; Engel-Herbert, R.; Janik, M. J.; Aktulga, H. M.; et al. The ReaxFF Reactive Force-Field: Development, Applications and Future Directions. *Npj Comput. Mater.* **2016**, *2*, 15011.

(140) Yoo, K.; Banerjee, S.; Dutta, P. Modeling of Volume Change Phenomena in a Li–air Battery. *J. Power Sources* **2014**, *258*, 340–350.

(141) Andersen, C. P.; Hu, H.; Qiu, G.; Kalra, V.; Sun, Y. Pore-Scale Transport Resolved Model Incorporating Cathode Microstructure and Peroxide Growth in Lithium-Air Batteries. *J. Electrochem. Soc.* **2015**, *162* (7), A1135–A1145.

(142) Xue, K.-H.; Nguyen, T.-K.; Franco, A. A. Impact of the Cathode Microstructure on the Discharge Performance of Lithium Air Batteries: A Multiscale Model. *J. Electrochem. Soc.* **2014**, *161* (8), E3028–E3035.

(143) Sandhu, S. S.; Fellner, J. P.; Brutchen, G. W. Diffusion-Limited Model for a Lithium/Air Battery with an Organic Electrolyte. *J. Power Sources* **2007**, *164* (1), 365–371.

(144) Ren, Y. X.; Zhao, T. S.; Tan, P.; Wei, Z. H.; Zhou, X. L. Modeling of an Aprotic Li-O2 Battery Incorporating Multiple-Step Reactions. *Appl. Energy* **2017**, *187*, 706–716.

(145) Grübl, D.; Bergner, B.; Schröder, D.; Janek, J.; Bessler, W. G. Multistep Reaction Mechanisms in Nonaqueous Lithium–Oxygen Batteries with Redox Mediator: A Model-Based Study. *J. Phys. Chem. C* **2016**, *120* (43), 24623–24636.

(146) Safari, M.; Adams, B. D.; Nazar, L. F. Kinetics of Oxygen Reduction in Aprotic Li-O2 Cells: A Model-Based Study. *J. Phys. Chem. Lett.* **2014**.

(147) Andrei, P.; Zheng, J. P.; Hendrickson, M.; Plichta, E. J. Some Possible Approaches for Improving the Energy Density of Li-Air Batteries. *J. Electrochem. Soc.* **2010**, *157* (12), A1287–A1295.

(148) Franco, A. A.; Xue, K.-H. Carbon-Based Electrodes for Lithium Air Batteries: Scientific and Technological Challenges from a Modeling Perspective. *ECS J. Solid State Sci. Technol.* **2013**, *2* (10), M3084–M3100.

(149) Bevara, V.; Andrei, P. Changing the Cathode Microstructure to Improve the Capacity of Li-Air Batteries: Theoretical Predictions. *J. Electrochem. Soc.* **2014**, *161* (14), A2068–A2079.

(150) Huang, J.; Faghri, A. Analysis of Electrolyte Level Change in a Lithium Air Battery. *J. Power Sources* **2016**, *307* (Supplement C), 45–55.

(151) Horstmann, B.; Danner, T.; G. Bessler, W. Precipitation in Aqueous Lithium–oxygen Batteries: A Model-Based Analysis. *Energy Environ. Sci.* **2013**, *6* (4), 1299–1314.

(152) Lau, S.; Archer, L. A. Nucleation and Growth of Lithium Peroxide in the Li–O_2 Battery. *Nano Lett.* **2015**, *15* (9), 5995–6002.

(153) Welland, M. J.; Lau, K. C.; Redfern, P. C.; Liang, L.; Zhai, D.; Wolf, D.; Curtiss, L. A. An Atomistically Informed Mesoscale Model for Growth and Coarsening during Discharge in Lithium-Oxygen Batteries. *J. Chem. Phys.* **2015**, *143* (22), 224113.

(154) Sahapatsombut, U.; Cheng, H.; Scott, K. Modelling the Micro–macro Homogeneous Cycling Behaviour of a Lithium–air Battery. *J. Power Sources* **2013**, *227*, 243–253.

(155) Franco, A. A. A Multiscale Physical Model of Electrochemical Energy Storage Devices. *ECS Trans.* **2013**, *45* (27), 11–19.

(156) Lu, Y.-C.; Gallant, B. M.; Kwabi, D. G.; Harding, J. R.; Mitchell, R. R.; Whittingham, M. S.; Shao-Horn, Y. Lithium–oxygen Batteries: Bridging Mechanistic Understanding and Battery Performance. *Energy Environ. Sci.* **2013**, *6* (3), 750–768.

(157) Ganapathy, S.; Adams, B. D.; Stenou, G.; Anastasaki, M. S.; Goubitz, K.; Miao, X.-F.; Nazar, L. F.; Wagemaker, M. Nature of Li_2O_2 Oxidation in a Li–O_2 Battery Revealed by Operando X-Ray Diffraction. *J. Am. Chem. Soc.* **2014**, *136* (46), 16335–16344.

(158) Bard, A. J.; Faulkner, L. R. *Electrochemical Methods: Fundamentals and Applications*; Wiley, 2000.

(159) Franco, A. A.; Tembely, M. Transient Multiscale Modeling of Aging Mechanisms in a PEFC Cathode. *J. Electrochem. Soc.* **2007**, *154* (7), B712–B723.

(160) Newman, J.; Tiedemann, W. Porous-Electrode Theory with Battery Applications. *AIChE J.* **1975**, *21* (1), 25–41.

(161) Laoire, C. O.; Mukerjee, S.; Abraham, K. M.; Plichta, E. J.; Hendrickson, M. A. Influence of Nonaqueous Solvents on the Electrochemistry of Oxygen in the Rechargeable Lithium−Air Battery. *J. Phys. Chem. C* **2010**, *114* (19), 9178–9186.

(162) Carl H. Hamann, A. H. and W. V. *Electrochemistry (2nd Edition)*; John Wiley & Sons, 2007.

(163) Scheers, J.; Lidberg, D.; Sodeyama, K.; Futera, Z.; Tateyama, Y. Life of Superoxide in Aprotic Li-O_2 Battery Electrolytes: Simulated Solvent and Counter-Ion Effects. *Phys Chem Chem Phys* **2016**.

(164) Luntz, A. C.; Viswanathan, V.; Voss, J.; Varley, J. B.; Nørskov, J. K.; Scheffler, R.; Speidel, A. Tunneling and Polaron Charge Transport through Li_2O_2 in Li–O_2 Batteries. *J. Phys. Chem. Lett.* **2013**, *4* (20), 3494–3499.

(165) Radin, M. D.; Tian, F.; Siegel, D. J. Electronic Structure of Li_2O_2 {0001} Surfaces. *J. Mater. Sci.* **2012**, *47* (21), 7564–7570.

(166) Myerson, A. S. Concluding Remarks. *Faraday Discuss.* **2015**, *179* (0), 543–547.

(167) Markov, I. V. *Crystal Growth for Beginners: Fundamentals of Nucleation, Crystal Growth and Epitaxy*, 2nd ed.; World Scientific: Singapore ; River Edge, N.J, 2003.

(168) Marqusee, J. A.; Ross, J. Kinetics of Phase Transitions: Theory of Ostwald Ripening. *J. Chem. Phys.* **1983**, *79* (1), 373–378.

(169) Voorhees, P. W. The Theory of Ostwald Ripening. *J. Stat. Phys. 38* (1–2), 231–252.

(170) Shi, L.; Xu, A.; Zhao, T. S. Formation of Li_3O_4 Nano Particles in the Discharge Products of Non-Aqueous Lithium–oxygen Batteries Leads to Lower Charge Overvoltage. *Phys. Chem. Chem. Phys.* **2015**, *17* (44), 29859–29866.

(171) Viswanathan, V.; Nørskov, J. K.; Speidel, A.; Scheffler, R.; Gowda, S.; Luntz, A. C. Li–O2 Kinetic Overpotentials: Tafel Plots from Experiment and First-Principles Theory. *J. Phys. Chem. Lett.* **2013**, *4* (4), 556–560.

(172) Luntz, A. C.; McCloskey, B. D. Nonaqueous Li–Air Batteries: A Status Report. *Chem. Rev.* **2014**, *114* (23), 11721–11750.

(173) Lepoivre, F.; Grimaud, A.; Larcher, D.; Tarascon, J.-M. Long-Time and Reliable Gas Monitoring in Li-O_2 Batteries via a Swagelok Derived Electrochemical Cell. *J. Electrochem. Soc.* **2016**, *163* (6), A923–A929.

(174) Girishkumar, G.; McCloskey, B.; Luntz, A. C.; Swanson, S.; Wilcke, W. Lithium−Air Battery: Promise and Challenges. *J. Phys. Chem. Lett.* **2010**, *1* (14), 2193–2203.

(175) Hu, Y.; Han, X.; Cheng, F.; Zhao, Q.; Hu, Z.; Chen, J. Size Effect of Lithium Peroxide on Charging Performance of Li–O_2 Batteries. *Nanoscale* **2014**, *6* (1), 177–180.

(176) Yin, Y.; Gaya, C.; Torayev, A.; Thangavel, V.; Franco, A. A. Impact of Li_2O_2 Particle Size on Li–O_2 Battery Charge Process: Insights from a Multiscale Modeling Perspective. *J. Phys. Chem. Lett.* **2016**, 3897–3902.

(177) Huang, J.; Zhang, B.; Bai, Z.; Guo, R.; Xu, Z.-L.; Sadighi, Z.; Qin, L.; Zhang, T.-Y.; Chen, G.; Huang, B.; et al. Anomalous Enhancement of Li-O_2 Battery Performance with Li_2O_2 Films Assisted by NiFeOx Nanofiber Catalysts: Insights into Morphology Control. *Adv. Funct. Mater.* **2016**, 8290–8299.

(178) Epstein, I. R.; Showalter, K. Nonlinear Chemical Dynamics: Oscillations, Patterns, and Chaos. *J. Phys. Chem.* **1996**, *100* (31), 13132–13147.

(179) Argentina, M.; Coullet, P. Chaotic Nucleation of Metastable Domains. *Phys. Rev. E* **1997**, *56* (3), R2359–R2362.

(180) Nielsen, A. E.; Söhnel, O. Interfacial Tensions Electrolyte Crystal-Aqueous Solution, from Nucleation Data. *J. Cryst. Growth* **1971**, *11* (3), 233–242.

(181) Xiao, J.; Mei, D.; Li, X.; Xu, W.; Wang, D.; Graff, G. L.; Bennett, W. D.; Nie, Z.; Saraf, L. V.; Aksay, I. A.; et al. Hierarchically Porous Graphene as a Lithium–Air Battery Electrode. *Nano Lett.* **2011**, *11* (11), 5071–5078.

(182) Lu, Y.-C.; Gasteiger, H. A.; Shao-Horn, Y. Catalytic Activity Trends of Oxygen Reduction Reaction for Nonaqueous Li-Air Batteries. *J. Am. Chem. Soc.* **2011**, *133* (47), 19048–19051.

(183) Geng, W. T.; Ohno, T. Li_2O_2 Wetting on the (110) Surface of RuO_2, TiO_2, and SnO_2: An Initiating Force for Polycrystalline Growth. *J. Phys. Chem. C* **2015**, *119* (2), 1024–1031.

(184) Krishnamurthy, D.; Hansen, H. A.; Viswanathan, V. Universality in Nonaqueous Alkali Oxygen Reduction on Metal Surfaces: Implications for Li–O_2 and Na–O_2 Batteries. *ACS Energy Lett.* **2016**, *1* (1), 162–168.

(185) Battaile, C. C. The Kinetic Monte Carlo Method: Foundation, Implementation, and Application. *Comput. Methods Appl. Mech. Eng.* **2008**, *197* (41), 3386–3398.

(186) Johansen, A. M.; Evers, L. Monte Carlo Methods. *Lect. Notes Univ. Bristol* **2007**, 1–128.

(187) Heath Turner, C.; Zhang, Z.; Gelb, L. D.; Dunlap, B. I. Kinetic Monte Carlo Simulation of Electrochemical Systems. In *Reviews in Computational Chemistry Volume 28*; Parrill, A. L., Lipkowitz, K. B., Eds.; John Wiley & Sons, Inc, 2015; pp 175–204.

(188) Jansen, A. P. J. *An Introduction to Kinetic Monte Carlo Simulations of Surface Reactions*; Springer, 2012.

(189) Ong, M. T.; Verners, O.; Draeger, E. W.; van Duin, A. C. T.; Lordi, V.; Pask, J. E. Lithium Ion Solvation and Diffusion in Bulk Organic Electrolytes from First-Principles and Classical Reactive Molecular Dynamics. *J. Phys. Chem. B* **2015**, *119* (4), 1535–1545.

(190) Cota, L. G.; de la Mora, P. On the Structure of Lithium Peroxide, Li_2O_2. *Acta Crystallogr. B* **2005**, *61* (2), 133–136.

(191) Hayamizu, K.; Aihara, Y.; Arai, S.; Garcia. Pulse-Gradient Spin-Echo ^{1}H, ^{7}Li, and ^{19}F NMR Diffusion and Ionic Conductivity Measurements of 14 Organic Electrolytes Containing $LiN(SO_2CF_3)_2$. *J. Phys. Chem. B* **1999**, *103* (3), 519–524.

(192) Kowalczk, I.; Read, J.; Salomon, M. Li-Air Batteries: A Classic Example of Limitations Owing to Solubilities. *Pure Appl. Chem.* **2007**, *79* (5).

(193) Smallwood, I. M. Dimethlsulphoxide. In *Handbook of Organic Solvent Properties*; Butterworth-Heinemann: Oxford, 1996; pp 253–255.

(194) Ma, S.; Wu, Y.; Wang, J.; Zhang, Y.; Zhang, Y.; Yan, X.; Wei, Y.; Liu, P.; Wang, J.; Jiang, K.; et al. Reversibility of Noble Metal-Catalyzed Aprotic Li-O_2 Batteries. *Nano Lett.* **2015**, *15* (12), 8084–8090.

(195) Jung, H.-G.; Jeong, Y. S.; Park, J.-B.; Sun, Y.-K.; Scrosati, B.; Lee, Y. J. Ruthenium-Based Electrocatalysts Supported on Reduced Graphene Oxide for Lithium-Air Batteries. *ACS Nano* **2013**, *7* (4), 3532–3539.

(196) Yilmaz, E.; Yogi, C.; Yamanaka, K.; Ohta, T.; Byon, H. R. Promoting Formation of Noncrystalline Li_2O_2 in the Li–O_2 Battery with RuO_2 Nanoparticles. *Nano Lett.* **2013**, *13* (10), 4679–4684.

(197) Shukla, G.; del Olmo Diaz, D.; Thangavel, V.; Franco, A. A. Self-Organization of Electroactive Suspensions in Discharging Slurry Batteries: A Mesoscale

Modeling Investigation. *ACS Appl. Mater. Interfaces* **2017**, *9* (21), 17882–17889.

(198) Roberts, M.; Younesi, R.; Richardson, W.; Liu, J.; Gustafsson, T.; Zhu, J.; Edström, K. Increased Cycling Efficiency of Lithium Anodes in Dimethyl Sulfoxide Electrolytes For Use in Li-O_2 Batteries. *ECS Electrochem. Lett.* **2014**, *3* (6), A62–A65.

(199) Shukla, G.; del Olmo Diaz, D.; Thangavel, V.; Franco, A. A. Self-organization of Electroactive Suspensions in Discharging Slurry Batteries: A Mesoscale Modeling Investigation. *ACS Appl. Mater. Interfaces* **2017**, *9* (21), 17882–17889.

(200) Adams, B. D.; Black, R.; Williams, Z.; Fernandes, R.; Cuisinier, M.; Berg, E. J.; Novak, P.; Murphy, G. K.; Nazar, L. F. Towards a Stable Organic Electrolyte for the Lithium Oxygen Battery. *Adv. Energy Mater.* **2015**, *5* (1), 1400867.

(201) Xu, D.; Wang, Z.; Xu, J.; Zhang, L.; Wang, L.; Zhang, X. A Stable Sulfone Based Electrolyte for High Performance Rechargeable Li–O_2 Batteries. *Chem. Commun.* **2012**, *48* (95), 11674–11676.

(202) Uludağ, A. A.; Tokur, M.; Algul, H.; Cetinkaya, T.; Uysal, M.; Akbulut, H. High Stable Li-Air Battery Cells by Using PEO and PVDF Additives in the TEGDME/LiPF6 Electrolytes. *Int. J. Hydrog. Energy* **2016**, *41* (16), 6954–6964.

(203) Zhang, S. S.; Read, J. A. A New Direction for the Performance Improvement of Rechargeable Lithium/Sulfur Batteries. *J. Power Sources* **2012**, *200*, 77–82.

(204) Kynar® PVDF Family http://www.extrememateriales-arkema.com/en/product-families/kynar-pvdf-family/ (accessed Jan 7, 2018).

(205) Marinaro, M.; Balasubramanian, P.; Gucciardi, E.; Theil, S.; Jörissen, L.; Wohlfahrt-Mehrens, M. Importance of Reaction Kinetics and Oxygen Crossover in Aprotic Li–O_2 Batteries Based on a Dimethyl Sulfoxide Electrolyte. *ChemSusChem* **2015**, *8* (18), 3139–3145.

(206) Storm, M. M.; Overgaard, M.; Younesi, R.; Reeler, N. E. A.; Vosch, T.; Nielsen, U. G.; Edström, K.; Norby, P. Reduced Graphene Oxide for Li–air Batteries: The Effect of Oxidation Time and Reduction Conditions for Graphene Oxide. *Carbon* **2015**, *85* (Supplement C), 233–244.

(207) *SFPE Handbook of Fire Protection Engineering*, 4 edition.; Dinenno, P. J., Drysdale, D., Ph D., Beyler, C. L., Ph D., Walton, W. D., Custer, R. L. P., Eds.; Natl Fire Protection Assn: Quincy, Mass.: Bethesda, Md, 2008.

Résumé des Travaux de Thèse

Introduction

Les brusques changements climatiques mondiaux ainsi que l'épuisement des combustibles fossiles nous incitent fortement à nous tourner vers des sources d'énergie renouvelables, à faible émission de carbone. Cependant, leur développement nécessite des dispositifs fiables pour concentrer et stocker l'énergie captée. Les batteries Li-oxygène (BLO) sont envisagées comme des candidats prometteurs pour les dispositifs de stockage d'énergie de prochaine génération car théoriquement ce sont des systèmes à très haute densité d'énergie. Malgré les efforts déployés au cours des dernières décennies, des percées fondamentales sont encore nécessaires pour permettre d'utiliser en pratique de tels systèmes. En effet, ces systèmes présentent une grande complexité du fait des mécanismes de réaction, des variations de texture des électrodes et des diverses réactions secondaires.

Les batteries Li-Air reposent sur la réaction électrochimique réversible entre le Li et l'oxygène gazeux. En réalité, il est donc plus précis de parler de batteries lithium -oxygène ou batteries Li-O_2 (BLO). Ces batteries peuvent fonctionner avec des électrolytes aqueux mais aussi non aqueux et produisent lors de la décharge LiOH et Li_2O_2, dont les potentiels thermodynamiques standards sont respectivement 3,45 et 2,96 V. Etant formé à un potentiel beaucoup plus élevé, LiOH est thermodynamiquement plus stable que Li_2O_2. Ainsi, en cas de présence d'eau dans des BLO non aqueux, LiOH se formera préférentiellement par rapport à Li_2O_2.

Une cellule BLO est constituée d'une électrode négative à base de lithium métal, d'un séparateur poreux et d'une électrode positive poreuse. Le séparateur et l'électrode poreuse sont tous deux imbibés d'électrolyte. Dans le cas des batteries Li-air aqueuses, une couche conductrice de Li mais toutefois électriquement isolante est déposée sur le lithium métal afin d'empêcher sa réaction avec l'eau.

Pendant le processus de décharge, les ions Li^+ sont formés à l'électrode négative .Dans les batteries aqueuses, les molécules d'O_2 dissoute dans l'électrolyte diffusent à la surface de l'électrode positive et y sont réduites et forment alors LiOH à partir des ions Li^+ et de l'eau. La solubilité de LiOH dans l'eau est d'environ 5,3 M, au-dessus de cette valeur, LiOH commence à précipiter dans la solution. Dans les batteries

non aqueuses, le solvant n'est pas impliqué dans la réaction. Les molécules d'O_2 dissoutes dans l'électrolyte sont réduites sur l'électrode positive en présence d'ions Li^+ pour former Li_2O_2 qui est insoluble dans le solvant organique. Ces réactions devraient se produire réversiblement lors du processus de charge, entrainant la décomposition des produits de décharge et le dépôt de lithium sur l'électrode négative. Cependant, le LiOH ne se décompose pas facilement car la liaison O-H est difficile à rompre. Cette limitation ainsi que la difficulté technique qui représente la protection de l'anode, tendent à limiter l'intérêt d'utiliser des batteries de type aqueux. Par conséquent, les efforts de recherche tout comme les travaux menés dans cette thèse se focalisent sur l'étude des batteries Li-oxygène non aqueuses.

La capacité de décharge est limitée à la fois par la passivation de l'électrode et par le colmatage des pores qui dépendent fortement de la morphologie du peroxyde de lithium (Li_2O_2) produit. La formation de petites particules de Li_2O_2 ou de couches minces conduit à une passivation rapide de l'électrode, tandis que la présence de larges particules de Li_2O_2 bloque les pores de l'électrode. La morphologie du Li_2O_2 est déterminée par les effets combinés des composants de l'électrolyte, des propriétés chimiques de l'électrode et de la densité de courant lors de la décharge. La texture de l'électrode, qui est principalement caractérisée par la surface spécifique, la taille des pores et le volume des pores, impacte également la capacité de décharge. Les électrodes de grande surface spécifique avec des pores de grande taille et présentant un volume poreux important sont favorables. En effet, une grande surface spécifique est ainsi développée et peut alors fournir un plus grand nombre de site actif pour les réactions électrochimiques. De plus, une grande taille de pores est moins susceptible d'être colmatée et un plus grand volume de pores peut contenir plus de Li_2O_2. Néanmoins, il est difficile de maximiser toutes ces propriétés de texture simultanément car elles sont fortement liées et dépendantes les unes des autres, ce qui rend donc difficile l'optimisation de l'électrode.

La charge des BLO souffre aussi de la forte surtension du système ainsi que du haut potentiel de l'électrode, tous deux corrélés à la nature isolante de Li_2O_2. Selon les électrolytes et matériaux d'électrode utilisés, de profils de charge très différents peuvent être obtenus, soulignant toute la complexité du processus de charge. Différents mécanismes de charge ont été proposés, mais aucun consensus n'a encore été trouvé.

Promue par les progrès des sciences informatiques, la modélisation mathématique apparaît comme un outil puissant pour étudier le comportement de systèmes complexes, comme cela a déjà été fait auparavant, pour réaliser les prévisions météorologiques ou encore les prédictions boursières. De nos jours, il est reconnu que la modélisation mathématique est utile pour évaluer et optimiser les systèmes électrochimiques tels que les piles à combustible à membrane échangeuse de protons et les batteries Li-ion. Dans ce contexte, combiner expérience et modélisation pourrait permettre de démêler l'impact des différentes composantes responsables de la complexité du système. Ainsi, la compréhension des batteries Li-oxygène sera approfondie dans l'espoir d'accélérer la maturation de cette technologie.

Bien que la modélisation informatique des BLO soit encore en phase de développement, de plus en plus de travaux ont été rapportés ces dernières années. Des méthodes de modélisation ont été appliquées au niveau microscopique et macroscopique. Les modèles microscopiques ont permis d'accéder à des informations au niveau moléculaire comme par exemple le transport de charge à travers le Li_2O_2, la stabilité de l'électrolyte et les impacts des catalyseurs. Les modèles macroscopiques, quant à eux, simulent les BLO au niveau de la cellule, en mettant l'accent soit sur la texture de l'électrode, soit sur la cinétique de la réaction. Malgré cela, afin de prédire les caractéristiques macroscopiques, comme le profil de décharge et de charge, en fonction des propriétés chimiques et texturales des composants de la cellule électrochimique, des modèles plus complets sont nécessaires. En outre, des modèles mésoscopiques sont également indispensables pour combler l'écart entre l'échelle microscopique et celle macroscopique dans l'espoir de fournir plus d'informations sur les problèmes non résolus du système Li-oxygène, tels que le rôle des catalyseurs et l'origine de l'augmentation du potentiel de charge.

Principaux résultats

Le travail accompli dans cette thèse a pour but de démêler la complexité des BLO en combinant modélisation et expérience. L'objectif est non pas de rechercher une adéquation quantitative parfaite entre la simulation et les résultats expérimentaux mais de mieux comprendre les liens entre les différents mécanismes.

Dans cette thèse, les sujets suivants ont été abordés:

- En raison du manque de modèles de (re-)charge dans la littérature, un modèle continu simulant une cellule de même qu'une série de modèles cinétiques ont été développés pour simuler le processus de (re-)charge des BLO. En considérant comme condition initiale une distribution de particules selon uniquement deux tailles différentes de Li_2O_2, préalablement formées pendant la décharge, les résultats de la simulation ont été capables de reproduire le profil de charge par paliers observé expérimentalement.

  Le modèle a attribué à chaque palier du profil le mécanisme de charge lié aux particules de Li_2O_2 de même taille. Pour les larges particules formées à partir du mécanisme de décharge en solution, leur décomposition nécessite initialement de dépasser la barrière de l'énergie d'activation de 0,4 V. Pour les petites particules obtenues par un mécanisme de surface lors de la décharge, un tel apport d'énergie n'est pas nécessaire. Ainsi, alors que les petites particules se décomposent à basse tension, l'oxydation des larges particules se produit uniquement à haute tension.

  Les modèles cinétiques ont fourni une explication alternative aux profils de charge par paliers en considérant le Li_2O_2 comme une résistance électrique. Comparées aux petites particules, les larges particules de Li_2O_2 provoquent une chute ohmique plus importante en raison de leur haute résistance et se décomposent donc à une tension plus élevée. La résistance du Li_2O_2 décroit pourtant lors de la décharge du fait de sa décomposition et donc de la réduction des tailles des particules. Cependant, le rétrécissement de la surface active a contrecarré les effets de la résistance décroissante. Par conséquent, le potentiel d'électrode continue à augmenter pendant le processus de charge.

  En outre, il apparait que selon l'historique de décharge, différents profils de charge sont observés. Ces modèles suggèrent que cette dépendance peut s'expliquer par la distribution des tailles de particules (DTP) de Li_2O_2 obtenues suite à différentes densités de courant de décharge.

- Pour calculer le DTP de Li_2O_2, un modèle simulant une cellule lors de la décharge a été développé pour simuler le phénomène de nucléation et croissance

de Li_2O_2, en combinant la théorie classique de nucléation, la cinétique de réactions élémentaires et le transport de masse.

Les résultats de la simulation ont permis de mieux appréhender la chute de potentiel et rapide remontée de potentiel (formant un décrochage en début de décharge) ainsi que la forme incurvé du plateau de décharge. Cette baisse de potentiel en début de décharge a été corrélée au processus de nucléation. Avant la nucléation, la sursaturation de paires ioniques $LiO2_{(pi)}$ entraîne la diminution du potentiel d'électrode. Comme la formation et la croissance de Li_2O_2 consomment en grande partie le $LiO2_{(pi)}$, le potentiel d'électrode remonte par la ensuite et atteint progressivement l'état quasi-stationnaire. Toutefois, avec la croissance des particules de Li_2O_2, la surface disponible de l'électrode rétrécit et la densité de courant locale augmente, provoquant ainsi la diminution du potentiel de l'électrode.

De plus, les résultats de la simulation ont confirmé la formation préférentielle de Li_2O_2 à proximité de l'entrée d'oxygène ainsi que la formation de particules de Li_2O_2 selon deux tailles différentes. Cette DTP peut être le résultat du processus de nucléation prenant place au stade initial puis au stade final du processus de décharge. La première nucléation est entraînée par la sursaturation de $LiO2_{(pi)}$, tandis que la seconde nucléation est due à la surtension plus élevée résultant de l'augmentation de la densité de courant locale du fait de la passivation de l'électrode.

De plus, le modèle lie la densité de courant, les propriétés de l'électrolyte et la propriété chimique de l'électrode au processus de nucléation. Le processus de nucléation peut être favorisé par une surtension importante (résultant d'un courant plus élevé), par une énergie de surface plus élevée entre le Li_2O_2 et l'électrolyte et par une liaison plus forte entre le Li_2O_2 et l'électrode. Dans ces conditions, les noyaux Li_2O_2 se forment alors rapidement sur la surface de l'électrode amenant à une passivation rapide de l'électrode et donc à une faible capacité de décharge. En revanche, moins de noyaux Li_2O_2 sont formés lorsque la surtension est faible (en raison d'une faible densité de courant), ainsi que lorsque l'énergie de surface entre le Li_2O_2 et l'électrolyte est faible, de même que lorsque l'énergie de surface entre le Li_2O_2 et l'électrode est relativement

faible. En conséquence, les noyaux formés sont plus à même de se développer en large particules via non seulement le mécanisme de croissance électrochimique, mais plus important encore, à travers le mécanisme de croissance chimique, résultant ainsi en une plus grande capacité de décharge.

- En complément des modèles déterministes, des modèles stochastiques basés sur la méthode kMC (kinetic Monte Carlo) ont été développés. Ils se concentrent sur l'échelle mésoscopique et ont été appliqués avec différentes hypothèses géométriques relatives à la structure de l'électrode.

  Les résultats de la simulation à partir du modèle de pores ont confirmé à nouveau la formation préférentielle de Li_2O_2 à proximité de l'arrivée d'oxygène. L'accumulation de Li_2O_2 peut alors gêner le transport de masse et même conduire au colmatage des pores et canaux. Ceci met en évidence l'importance d'optimiser la taille des pores et la connectivité des pores de l'électrode positive. De plus, le modèle des pores révèle que la diminution de la concentration de sel dans l'électrolyte peut favoriser la capacité de décharge en raison de l'amélioration de la mobilité de l'oxygène, cette tendance correspond à ce qui a été observé expérimentalement.

  Également basé sur la méthode de kMC, le modèle de fibre s'est concentré sur la formation de Li_2O_2 sur une Nano Fibres de Carbone (NFC) chargée et sans catalyseur. Les résultats de la simulation suggèrent que la présence de catalyseurs sur la NFC conduit à une cinétique de réaction inhomogène sur la surface de la fibre ainsi qu'à une vitesse de transfert de charge plus rapide, ce qui aboutit à une mauvaise sélectivité du site réactionnel. Par conséquent, la compacité et le degré d'ordre du film mince de Li_2O_2 sur la NFC enrichie en catalyseur sont plus bas que sur la NFC sans catalyseur. Ceci est en accord avec l'observation expérimentale suivante: la cristallinité de Li_2O_2 décroit avec la présence de catalyseur. Selon la littérature, le Li_2O_2 amorphe est décomposé à une tension inférieure que le Li_2O_2 cristallin, ce modèle propose que plutôt que catalyser directement l'oxydation de Li_2O_2, le catalyseur devrait abaisser le potentiel de charge en contrôlant la cristallinité de Li_2O_2 pendant la décharge.

- Parallèlement à l'étude de modélisation, des tests expérimentaux ont été mis en place pour tester les BLO dans des conditions proches de celles supposées dans les modèles. Le montage a été modifiée à partir d'un pot hermétique commercial et son grand volume a permis de faire cycler deux cellules à la fois ayant ainsi un environnement identique.

  De plus, par rapport à l'électrode composite en carbone, il apparait que l'électrode GDL (Gas Diffusion Layer) est une meilleure électrode de référence. L'électrode GDL est flexible, ne requière pas de collecteur, contient peu de polymère et surtout présente une texture macroporeuse. En utilisant des disques GDL comme électrode positive des BLO, une série d'expériences a été effectuée pour valider l'impact du courant sur le processus de décharge comme prédit par le modèle de décharge. Les résultats expérimentaux sont en adéquation avec la prédiction du modèle en ce qui concerne la forme du profil de décharge, la variation de la capacité de décharge et l'évolution de la taille des particules de Li_2O_2 à différents courants.

Conclusions et perspectives

Dans ce contexte, nous avons montré que la combinaison de la modélisation et des expériences permet de fournir une meilleure compréhension des mécanismes complexes prenant place lors de la charge et décharge et par conséquent permet de mieux comprendre le système Li-oxygène dans son ensemble. Dans l'approche utilisée, modélisation et expérience sont intrinsèquement liées. D'une part, les modèles sont basés sur des phénomènes observés expérimentalement et utilisent des paramètres expérimentaux. D'autre part, la modélisation peut être utilisée comme outil pour rationaliser les résultats observés lors des expériences et de vérifier la cohérence physique et chimique des théories proposées pour expliquer les observations expérimentales.

De plus, les travaux de cette thèse ont également indiqué qu'au lieu d'être étroitement liés, la modélisation et l'expérience devraient être plutôt développées en parallèle. Bien que la communication entre les approches théoriques et expérimentales soit importante, il est difficile et n'est pas nécessaire d'avoir une correspondance parfaite ainsi qu'une validation au cas par cas du fait des simplifications inévitables

réalisées dans un modèle et du fait de la précision limitée inhérente aux mesures expérimentales.

Devant tous ces défis, le futur des batteries Li-oxygène et leur utilisation d'un point de vue pratique sont encore incertains. Cependant, les connaissances accumulées grâce à la modélisation couplée aux expériences, sont cruciales pour accélérer les progrès dans la compréhension de ces systèmes complexes.

Il serait intéressant de compléter ce travail en effectuant des expériences-modèles se concentrant sur d'autres effets tels que les impacts de la chimie de surface des électrodes ou la nucléation et la croissance de Li_2O_2, dans l'espoir de renforcer le couplage modélisation/expérience. En outre, un modèle simulant des cycles complet de charge/décharge, capable de simuler automatiquement les BLO lors du cyclage, devrait être développé afin d'étudier plus en profondeur les impacts de l'historique de cyclage sur les performances des cellules.

Ce travail de thèse a fourni des contributions utiles pour deux autres travaux de doctorat en cours. Le montage "Le Parfait" a été utilisé dans leurs expériences d'optimisation de texture d'électrode et de fonctionnement en environnement ambiant. Les modèles développés au cours de cette thèse leur ont permis d'obtenir des modèles plus sophistiqués en incluant les réactions parasites de la décomposition des électrolytes et des contaminants de l'air. Basé sur le modèle stochastique 3D, un jeu de RV (Réalité Virtuelle) a été développé pour introduire le concept et le principe de fonctionnement des BLO à des fins d'éducation.

Plus généralement, la méthodologie proposée dans cette thèse peut également être appliquée aux autres systèmes électrochimiques incluant d'autres batteries métal-air et des batteries Li-S (Li-Soufre) pour obtenir une meilleure compréhension. Par exemple, le modèle de nucléation a été adapté à la batterie Li-S par un doctorat du LRCS pour étudier la nucléation et la croissance de Li_2S. Un modèle similaire peut également être utile pour étudier la déposition du lithium afin de contribuer au développement de l'anode Li-métal pour son application dans les batteries Li-ion, BLO et Li-S.

Appendix I: List of Acronym

AC	Active carbon
AS	Association strength
CNF	Carbon nano-fiber
CNT	Carbon nano-tube
DEMS	Differential electrochemical mass spectrometry
DFT	Density functional theory
DMA	Dimethylacetamide
DME	1,2-Dimethoxyethane,
DMSO	Dimethyl Sulfoxide
DN	Donor number
EDL	Electrochemical double layer
EV	Electrical vehicle
GDL	Gas diffusion layer
ICV	Internal combustion engine vehicles
kMC	Kinitic Monte Carlo
LAB	Lithium-air battery
LIB	Lithium-ion battery
LOB	Lithium-oxygen battery
MD	Molecular dynamics
MMC	Metropolis Monte Carlo
PHS	Pumped hydroelectric storage
PSD	Particle size distribution
PTFE	Polytetrafluoroethylene

PVdF	Polyvinylidene difluoride
RRDE	Rotating ring disk electrode
SEI	Solid electrolyte interface
SEM	Scanning electron microscopy
SW	Swaglok® type cell
TGA-MS	Thermogravimetric Analysis/Mass Spectrometry
TPES	Total Primary Energy Supply
TEGDME	Tetraethylene glycol dimethyl ether
VC	Vulcan carbon
VR	Virtual reality
VSSM	Variable step size method
XRD	X-ray diffraction

Appendix II: List of publications and communications

Publications:

Journal

(1) Yin, Y.; Zhao, R.; R.; Ciger, J.; Lelong, R.; Franco, A. A. An Interactive and Immersive Virtual Reality Game for Teaching Electrochemical Energy Conversion and Storage. *J. Chem. Educ,* submitted

.(2) Yin, Y.; Torayev, A.; Gaya, C.; Mammeri, Y.; Franco, A. A. Linking the Performances of Li–O_2 Batteries to Discharge Rate and Electrode and Electrolyte Properties through the Nucleation Mechanism of Li_2O_2. *J. Phys. Chem. C.* **2017**, *121* (36), 19577–19585.

(3) Yin, Y.; Zhao, R.; Deng, Y.; Franco, A. A. Compactness of the Lithium Peroxide Thin Film Formed in Li–O_2 Batteries and Its Link to the Charge Transport Mechanism: Insights from Stochastic Simulations. *J. Phys. Chem. Lett.* **2017**, *8* (3), 599–604.

(4) Yin, Y.; Gaya, C.; Torayev, A.; Thangavel, V.; Franco, A. A. Impact of Li_2O_2 Particle Size on Li–O_2 Battery Charge Process: Insights from a Multiscale Modeling Perspective. *J. Phys. Chem. Lett.* **2016**, 3897–3902.

(5) Blanquer, G.; Yin, Y.; Quiroga, M. A.; Franco, A. A. Modeling Investigation of the Local Electrochemistry in Lithium-O_2 Batteries: A Kinetic Monte Carlo Approach. *J. Electrochem. Soc.* **2016**, *163* (3), A329–A337.

Book chapter

Yin, Y; Franco, A. A. (2018) Montecarlo modelling of electrocatalytic reactions. In Klaus Wandelt (Ed.) *Encyclopedia of Interfacial Chemistry,* in press.

Communications:

Oral:

(1) Yin, Y.; Zhao, R.; Deng, Y.; Franco, A. A. "Meso-Scale Model of Li_2O_2 Formation in Li-O_2 Batteries: Compactness of Thin Film and Its Link to Charge Transport Mechanism" , oral presentation in **the 231th ECS Meeting** (New Orleans, USA, May 28-June 1, 2017).

(2) Yin, Y.; Gaya, C.; Torayev, A.; Thangavel, V.; Larcher, D. ; Franco, A. A. "Multi-Scale Modeling and Experimental Characterization of Charge Process of Li-O_2 Batteries: Impacts of Particle Size and Cycling History", oral presentation in **the 231th ECS Meeting** (New Orleans, USA, May 28-June 1, 2017).

* Awarded a Travel Grant by ECS, European Section

(3) Yin, Y.; Torayev, A.; Gaya, C.; Thangavel, V.; Franco, A. A. "Understanding the role of Li_2O_2 particle size on Li-O_2 battery charge process" **the 20th ISE Topical Meeting** (Buenos Aires, Argentina, March 19-22, 2017)

(4) Y. Yin, M. A. Quiroga, G. Blanquer, A.A. Franco, "Boosting Lithium Air Batteries from Multiscale Modeling", oral presentation in **the 66th ISE Annual Meeting** (Taipei, Taiwan, October 4-9, 2015).

Teaching:

Teaching assistant in Hands-on session of Continuum modeling and KMC modeling at **College on Multiscale Computational Modeling of Materials for Energy Storage Applications,** (International Centre for Theoretical Physics, Trieste, Italy, July 04-15, 2016).

RESUME

En raison de leur capacité théorique élevée, les batteries Li-air ont été considérées comme des dispositifs de stockage d'énergie prometteurs depuis leur invention. Cependant, la grande complexité de ces dispositifs a entravé leur application pratique. En plus, les résultats expérimentaux et les théories mécanistes rapportés dans la littérature sont épars et ajoutent des difficultés pour développer une compréhension globale de leurs principes de fonctionnement. Le travail accompli dans cette thèse repose sur la combinaison de deux approches : la modélisation et l'expérimentation, non pas dans le but d'avoir une adéquation parfaite entre simulation et expérience mais afin de mieux comprendre le lien entre les différents mécanismes mis en jeux.

Un modèle de déchargé, basé sur une approche continuum et rassemblant théorie de la nucléation, description des réactions cinétiques et du transport de masse, a été développé. Le modèle permet d'étudier simultanément l'impact de la densité de courant, des propriétés de l'électrolyte et des propriétés de surface de l'électrode sur le procédé de décharge des batteries Li-air permettant ainsi une meilleure compréhension. De plus, le modèle de charge développé lors de cette thèse, met en lumière la corrélation entre la distribution des tailles de particules de Li_2O_2 et le profil de recharge obtenu. Finalement, afin d'étudier ces batteries au niveau mésoscopique, un modèle de cinétique Monte-Carlo a été créé et permet de comprendre les processus de décharge dans des espaces confinés.

ABSTRACT

Due to their high theoretical capacity, Li-air batteries (LABs) have been considered as promising energy storage devices since their invention. However, the high complexity of these devices has impeded their practical application. Moreover, the scattered experimental results and mechanistic theories reported in literature, add difficulties to develop a comprehensive understanding of their operation principles. The work accomplished in this thesis constitutes an effort to entangle the complexity of LABs through the combination of modeling approaches with experiments, with the focus on getting better understanding about the mechanisms interplays, rather than pursuing a perfect quantitative match between simulation and experimental results.

Based on continuum approach, a discharge model has been developed combining the nucleation theory, reaction kinetics and mass transport. This model converged the impacts of current density, electrolyte property and electrode surface property on the discharge process of LABs to a comprehensive theory. Furthermore, a charge model has been developed to address the important role of Li_2O_2 particle size distribution in determining the shape of recharge profile. In addition, to investigate the LAB system at mesoscale, a kinetic Monte Carlo (KMC) model has been build and the simulation results provided insights into the discharge process in confined environment at local level.